APPLICABILITY OF SPECIFIC SPEED AND ZWEIFEL COEFFICIENT RECOMMENDATIONS TO LOW HEAD AXIAL HYDRAULIC TURBINES

By

Zachary Hoyle

A THESIS

Submitted to
Michigan State University
In partial fulfillment of the requirements
For the degree of

Mechanical Engineering – Master of Science

2017

ABSTRACT

APPLICABILITY OF SPECIFIC SPEED AND ZWEIFEL COEFFICIENT RECOMMENDATIONS TO LOW HEAD AXIAL HYDRAULIC TURBINES

By

Zachary Hoyle

This thesis work investigates the applicability of literature recommendations regarding specific speed and Zweifel coefficient for low head axial hydraulic turbines with constant blade thickness circular arc blade profiles, and no inlet guide vane. Highest efficiency was observed in Computational Fluid Dynamics (CFD) investigations for the designs running at speeds 12-33% that of the speed recommended by the Cordier line. Designs that followed the Zweifel coefficient recommendations of the literature in range of 0.8-1.1 demonstrated highest efficiency in CFD investigations. To test the applicability of the Cordier line recommendations for machines of this type, designs at differing specifications were tested at six different rotational speeds. Peak efficiency was measured at specific speeds between 1.4 and 1.9, compared to the Cordier-recommended value of 5.5 to 6.1. Next designs with differing values of Zweifel coefficient were simulated at the rotational speed at which highest efficiency was measured for each set of specifications. Zweifel coefficient was altered by changing the axial blade length. It was found that highest efficiency was measured at Zweifel coefficients between 0.8 and 1.1. The designs with higher axial blade lengths had lower Zweifel coefficient, and experienced greater friction losses. Decreasing blade length and increased Zweifel coefficients were correlated with more severe velocity gradients at the leading edge, increased flow deviation and areas of low pressure where cavitation could occur. Designs with the shortest blades (Zwefiel coefficient above 1.2) experienced greater velocity gradients and turbulence at the trailing edge and decreased efficiency.

ACKNOWLEDGEMENTS

I greatly appreciate the support of those who have helped me through the Mechanical Engineering Master's program at Michigan State University. First, I thank my family for the love and support they have always provided, my father Randy, my mother Jill, my brother Randall, and my sister Jacqui. I'd like to thank my committee, Dr. Xinran Xiao, Dr. Abraham Engeda, and Dr. Norbert Mueller for their assistance, patience, and help to complete this work. A special thank you to Dr. Norbert Mueller, who for the past 5 years has provided enormously valuable advice and opportunities which have helped me gain experience in engineering and turbomachinery. All of the experience which I now have on my resume is the result of opportunities which Dr. Mueller has provided. I would like to thank my friends and colleagues who have provided very valuable guidance which helped me complete this thesis, in particular Blake Gower and Thomas Qualman. Thank you to Tim Hinds and Andrew Mccolm for providing the financial support which has allowed me to complete the program.

TABLE OF CONTENTS

LIST OF TABLES

LIST OF FIGURES

KEY TO SYMBOLS

A_m = meridonial cross-sectional area (m^2)

α = Absolute flow angle $(degrees)$

b = Axial blade length (m)

β = Relative flow angle$(degrees)$

β_b = Blade angle $(degrees)$

β_m = Mean relative flow angle $(degrees)$

C = Absolute flow speed $(\frac{m}{s})$

$\overrightarrow{C}$ = Absolute flow speed (vector form) $(\frac{m}{s})$

c = Chord length (m)

C_m = Absolute flow speed in meridional direction $(\frac{m}{s})$

C_u = Absolute flow speed in tangential direction $(\frac{m}{s})$

C_Y = Tangential force coefficient

C_d =Drag coefficient

C_x =Axial force coefficient

C_l = Lift force coefficient

D = Outside diameter (m)

D_s = Specific Diameter

$\tilde{e}$ = Mass-specific shaft work output $(\frac{m^2}{s^2})$

e = Total mass-specific work done on the fluid from leading edge to trailing edge $(\frac{m^2}{s^2})$

f = friction factor

F_x = Axial force $(\frac{kg\ m}{s^2})$

F_d = Drag force $(\frac{kg\ m}{s^2})$

F_l = Lift force $(\frac{kg\ m}{s^2})$

F_f = friction work lost per unit mass $(\frac{m^2}{s^2})$

g = gravitational acceleration constant $(\frac{m}{s^2})$

h_b = Blade height (m)

h = Enthalpy $(\frac{m^2}{s^2})$

h_o = Stagnation enthalpy$(\frac{m^2}{s^2})$

H = total head (m)

i' = Inlet incidence $(degrees)$

k = Turbulence kinetic energy $(\frac{m^2}{s^2})$

K = Friction loss coefficient from 90 degree turn

L_t = length of penstock pipe (m)

$\dot{m}$ =Mass flow rate $(\frac{kg}{s})$

$\Delta\dot{m}$ = Mass flow rate through a single blade passage $(\frac{kg}{s})$

N = Rotational speed $(\frac{rot}{s})$

N_s = Specific Speed (rot)

N_{rpm} = rotational speed (rot/min)

N_b = number of blades

P = Static pressure $\left(\frac{kg}{ms^2}\right)$

P_t = Total Pressure $\left(\frac{kg}{ms^2}\right)$

P_{atm} = Atmospheric Pressure $\left(\frac{kg}{ms^2}\right)$

$\dot{Q}$ = Heat input $(\frac{m^2 kg}{s^3})$

R_e= Reynolds Number

r_h = Inside (hub) radius (m)

r_s = Outside (shroud) radius (m)

r_θ = Distance from centerline in tangential direction (m)

r_m = Mean radius (m)

r_b = Radius of the penstock pipe (m)

ρ = Density $\left(\frac{kg}{m^3}\right)$

s = Blade spacing (m)

t = Blade thickness (m)

T = Local temperature $(Celcius)$

u = Local flow velocity $(\frac{m}{s})$

U = Rotor tip speed$(\frac{m}{s})$

$\overrightarrow{U}$ =Absolute rotor velocity (vector form) $(\frac{m}{s})$

U_θ = Absolute speed of rotor at position along span $(\frac{m}{s})$

$\dot{V}$ = Volume flow rate $(\frac{m^3}{s})$

ω = Angular velocity $(\frac{rad}{s})$

W = Relative flow speed $(\frac{m}{s})$

$\overrightarrow{W}$ = Relative flow speed (vector form) ($\frac{m}{s}$)

$\dot{W}$ = Shaft power output ($\frac{m^2 kg}{s^3}$)

W_{mean} = Mean relative velocity ($\frac{m}{s}$)

W_m = Relative flow speed in meridional direction($\frac{m}{s}$)

W_u = Relative flow speed in tangential direction ($\frac{m}{s}$)

Y = Tangential blade force ($\frac{kg\ m}{s^2}$)

Y_{id} = Idealized blade force ($\frac{kg\ m}{s^2}$)

Z = Zweifel Coefficient

z = Position above datum (m)

ξ = Loss coefficient

δ' = Outlet deviation ($degrees$)

ε_r = surface roughness(m)

ϕ = Flow Coefficient

ψ = Blade loading coefficient

ψ' = Head coefficient

ϕ' = Capacity Coefficient

μ = Kinematic viscosity

μ_t = Kinematic turbulence viscosity

δ_{jk} = Kroneker delta

Ω_s = Specific Speed (rad)

γ = Hub-tip ratio

$\eta =$ Isentropic turbine efficiency

$\eta_t =$ Total turbine efficiency

$\tau_{jk}{}'$ = Reynolds stresses$\left(\frac{kg}{ms^2}\right)$

$\tau_a =$ Time rate of change of momentum about a

$\tau =$ Shear stress$\left(\frac{kg}{ms^2}\right)$

Subscripts

max = At 100% efficiency, idealized

1 = Turbine leading edge

$2 =$ Turbine trailing edge

a = Position a: water surface/inlet of penstock pipe

b = Position b: outlet of penstock pipe/inlet of turbine entry annulus

1= Position 1: Turbine leading edge

2 = Position 2: Turbine trailing edge

c = Position c: Outlet of turbine exit annulus, water level

x = axial direction

h = hub

s = shroud

i = ideal property (assuming 100% efficiency)

k = index notation

j = index notation

$\theta =$ Tangential direction

CHAPTER 1. INTRODUCTION AND BACKGROUND

1.1. Introduction to Hydroelectric Power

Hydroelectricity is known as a renewable, sustainable, clean energy source with large potential for new development in the United States [1]. Hydroelectric power plants convert the kinetic and potential energy of water into electric power. To accomplish this, hydroelectric power plants use a turbine which converts the energy of the water into mechanical work, which is then transferred to a generator converting that mechanical work into electric power. Hydraulic (hydro) turbines usually have a stator which directs the water flow, as well as a runner or rotor. The stator directs the flow in a desired direction, using vanes or a nozzle. The rotor has blades which change the angular momentum of the flow, exerting a torque on the rotor inducing rotation [2].

The two main parameters which govern the amount of power which can be generated by a hydraulic turbine are the total available head H and the volume flow rate $\dot{V}$. Head is defined as the height difference between two water surfaces. Most hydropower plants use a dam to generate the head necessary for hydroelectric power generation. These dams hold back water, creating a reservoir with a high water level on one side of the dam. The potential energy of the water behind the dam is used to extract energy. Hydroelectric dams often use an intake pipe, called a penstock, to feed water into the turbine. After the water flows through the turbine, it flows through an outlet tube called a draft tube which has an expanding cross-section. The draft tube is designed to decelerate the water. The use of a draft tube also allows for the turbine to be placed above the lower water level and extract the full potential energy of the water. Therefore the draft tube ensures that the head of the water below the tail race level [3].

An example of this is shown below in Figure 1.1, a diagram of a dam with a hydroelectric system.

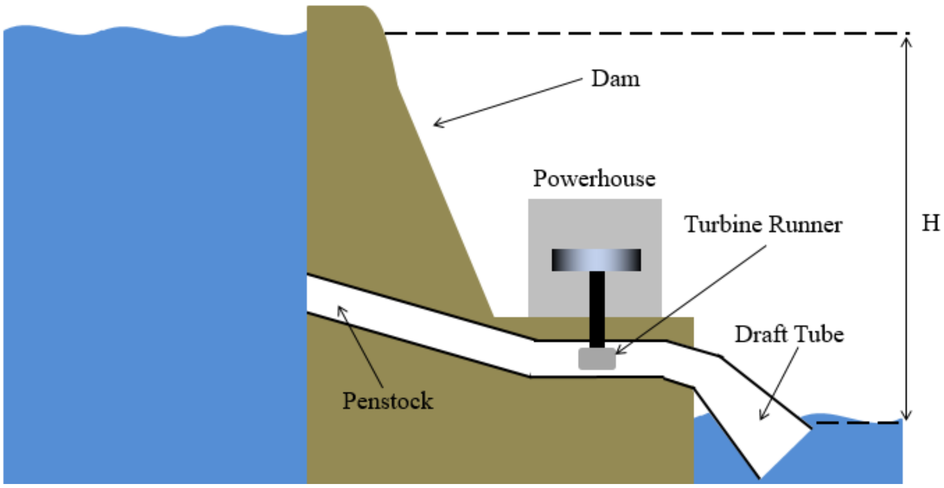

Figure 1.1. Hydroelectric Dam Schematic

The amount of electric power generated by a hydroelectric system $\left(\dot{W}\right)$ depends on the total efficiency of the system (η_t), the total head H, the gravitational acceleration constant g, and the volume flow rate $\dot{V}$, and is calculated using equation 1-1 [4]:

$$\dot{W} = g\dot{V}H\eta_t \tag{1-1}$$

The total efficiency of the system depends on the isentropic efficiency of the turbine rotor, the amount of friction losses in the penstock and draft tube, as well as the efficiency of the generator, among other factors.

1.2. Hydroelectric Power Challenges

Hydroelectric sites can be categorized by the potential for power output. They are divided into Large, Medium, Small, Mini, and Micro categories. This thesis focuses primarily on Mini hydro (between 100 and 1000 kW) and Micro hydro (up to 100 kW) turbine designs and development. Up to this point, constraints and problems related to the development of mini/micro hydropower include [5]:

1. High capital cost of hydropower generation equipment

2. High cost of civil works typically associated with mini/micro hydropower
3. High operations/maintenance cost

The US Department of Energy has suggested pre-packaged, pre-assembled modular low cost hydroelectric units are needed to solve this problem [1]. It has been suggested that a reduction in the capital cost of mini/micro hydroelectric units could lead to additional growth of hydropower generation in the United States [1]. This thesis focuses on the first problem, specifically the high capital cost of the turbine equipment.

1.3. Hydroelectric Dam Retrofits

In order to achieve the goal of expanding hydropower use, it is advantageous to look for potential sites with the lowest potential cost of installation and civil works. "Hydroelectric dam retrofits" are considered to be a cost-effective hydropower development strategy. Hydroelectric dam retrofits involve installing hydropower generation equipment into existing dams that have the necessary water volume flow and head for potential power generation [6]. The power generated could either be used to supplement the grid or offset electricity costs for municipal dam owners.

In a report prepared for the US Department of Energy, The Oak Ridge National Laboratory stated that the primary advantage of hydroelectric dam retrofits compared to new hydropower development is that "many of the costs and environmental impacts of dam construction have already been incurred at NPDs (Non-Powered-Dams) and may not be significantly increased by the incorporation of new energy production facilities. Thus, the development of some NPD's for energy purposes is assumed to be achievable with lower installed cost, lower levelized cost-of-energy, fewer barriers to development, less technological and business risk, and in a shorter time frame than development requiring new dam construction"

[6]. The Oak Ridge National Laboratory has estimated that a potential additional 12.6 gigawatts of power could be generated from hydroelectric dam retrofits in the United States. It is considered an abundant potential source of renewable energy in the US. There are over 80,000 non-powered dams in the United States, and it is estimated 54,000 of these have the water flow and head necessary for considerable power output if a hydroelectric system was installed [6].

Civil works contribute around 40% of the total cost of conventional small hydro projects [7]. The civil work projects that need to be done for a hydroelectric dam retrofit include the intake, penstock, and power house construction. Civil works cost also include any temporary infrastructure needed during installation and construction. Typically when installing new hydropower equipment into an existing dam, the dam must be de-watered and a new temporary dam must be constructed. The cost of the civil works projects associated with a hydroelectric dam retrofit are highly dependent on the design of the hydroelectric system selected.

It is advantageous to design the hydroelectric dam retrofit system such that extensive modification of the existing dam structure is not required. Many non-powered dams in the United States have spillways from which water flows. Most spillways have gates which control the rate at which water flows through the dam. Figure 1.2 below shows the Bellaire Dam in Antrim County, Michigan, and Figure 1.3 shows a spillway gate at the dam.


Figure 1.2. Bellaire Dam, Antrim County, Michigan


Figure 1.3. Spillway at the Bellaire Dam, Antrim County, Michigan

The analytical model in this work was set up to obtain CFD boundary conditions which were applicable for a proposed application of a hydraulic turbine for use as a retrofit turbine unit to fit on the front of dam spillways. The setup analyzed in this work is illustrated in Figure 1.4 below.

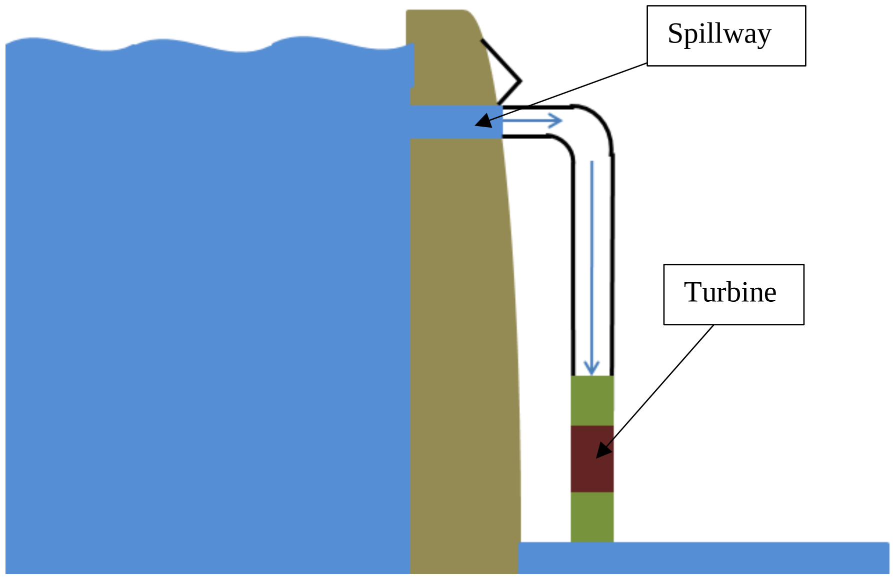

Figure 1.4. Hydroelectric dam retrofit schematic

1.4. Selection of Type of Water Turbine

When selecting a turbine system to be used for a potential site for hydroelectric plant installation, a number of different factors are considered. The first being the volume flow rate, head, and power obtainable given the geographic constraints of the hydropower site. The degree of complexity involved to build/install the hydroelectric system, as well as maintenance requirements of the turbine technology being evaluated are also considered. The portability and shipping cost of the system are factors as well as the degree of modularity of the turbine being considered for selection and potential environmental impacts. Modular turbine systems are of value as it allows for the turbine to be broken up into smaller components for easy maintenance and replacement in the field [2]. Before going forward on a hydropower project, the capital and operating costs of the system are weighed against the value of the energy the plant will generate. Engineers often pick the type of turbine to be used for a particular application by observing the designed flow rate and head, and picking the type of turbine based off of recommendations of literature.

1.5. Woven Wheel Hydro Turbine

A technology invented by Dr. Norbert Mueller at Michigan State University known as the Woven Wheel offers promise to reduce the capital cost and complexity of hydraulic turbines. The Woven Wheel is a manufacturing process which involves manufacturing turbomachinery blades by winding the wheel out of continuous composite fiber strands. The wheels are designed such that the fibers are wound in tension. For the Woven Wheel manufacturing technique, the A technology invented by Dr. Norbert Mueller at Michigan State University known as the Woven Wheel offers promise to reduce the capital cost and complexity of hydraulic turbines. The Woven Wheel is a manufacturing process which involves manufacturing turbomachinery blades by winding the wheel out of continuous composite fiber strands. The wheels are designed such that the fibers are wound in tension. For the Woven Wheel manufacturing technique, the continuous fiber is wound around a low-cost mandrel which can be 3-D printed. The technology allows for motor and generator components to be integrated directly into the hub or shroud, decreasing the cost of producing modular turbines or compressors which use the Woven Wheel as the rotor [8]. The winding of these wheels can be done by hand or using a commercially available computer controlled winding machine. The Woven Wheel design includes an outer shroud [9]. This winding process allows for a large number of different winding patterns to be employed. Figure 1.5(a) below shows a computer rendering of one such winding pattern. Figure 1.5(b) shows the wound turbomachine wheel inside of the mandrel, and Figure 1.5(c) shows the wheel after removal from the mandrel.

Figure 1.5. (a) 3-D model of Woven Wheel winding scheme (b) Woven Wheel in mandrel (c) Woven wheel removed from mandrel

This technology developed at Michigan State University allows for lower cost manufacturing of axial water turbines with integrated generator components. Inclusion of an integrated generator along the shroud of the rotor can decrease the part count and required maintenance as well. A prototype Woven Wheel water turbine was successfully tested for a tidal turbine application in a tow tank at the Marine Hydrodynamic Lab, at the University of Michigan, shown below in Figure 1.6.

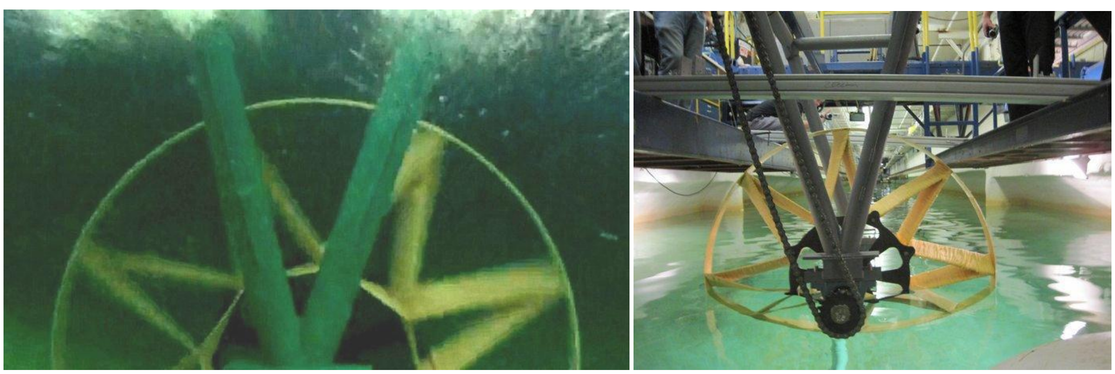

Figure 1.6. Woven Wheel tidal turbine being tested inside the tow tank

Integrated motor components have been demonstrated in the Woven Wheel's application as a compressor; however, the integration of the generator components in the Woven Wheel's application as a water turbine has yet to be prototyped. The turbine rotor tested, manufactured using the Woven Wheel manufacturing method was wound from Kevlar-49. Kevlar fiber has a specific strength three times higher than titanium alloys [10]. The advantages of using this Woven Wheel technology as a water turbine are discussed further below.

1.5.1. Lightweight, Modular Design

The Woven Wheel modular turbine or compressor units can be assembled in a row to form a modular multistage unit. Kevlar is a high strength, low cost, low weight fiber material which can be considered a good choice of composite material for winding a Woven Wheel for use as a water turbine. Figure 1.7 below shows a rendering of one such modular design. A recent Woven Wheel prototype weighed approximately 50% of a wheel of the similar geometry machined from 6061 T6 aluminum.

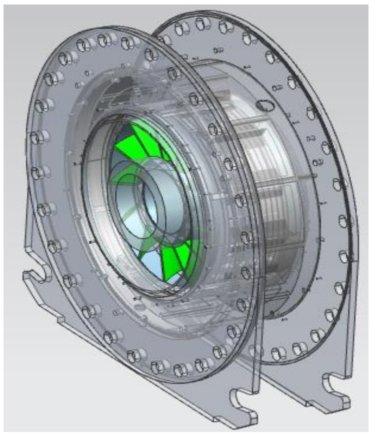

Figure 1.7. Modular Woven Wheel compressor unit design

1.5.2. Low-cost Additive Manufacturing

The Woven Wheel can be manufactured by winding a continuous carbon fiber bundle around a 3-D printed mandrel to form the shape of the blades. The wheel with mandrel is then infused with epoxy and cured, after which the wheel is removed from the mandrel. Preliminary prototyping of manufacturing Woven Wheels using this method has taken place at Michigan State University. The cost of manufacturing traditional turbine blades with an integrated shroud with traditional turbine manufacturing methods is high as it would require more raw material, and machining processes. The weight of the turbine would inevitably increase as well. Figure 1.8 below shows a 3-D printed mandrel and the winding process. Although the process requires further maturation, prototypes have demonstrated it costs less to purchase the materials and produce compared to traditional rotors machined out of metal.

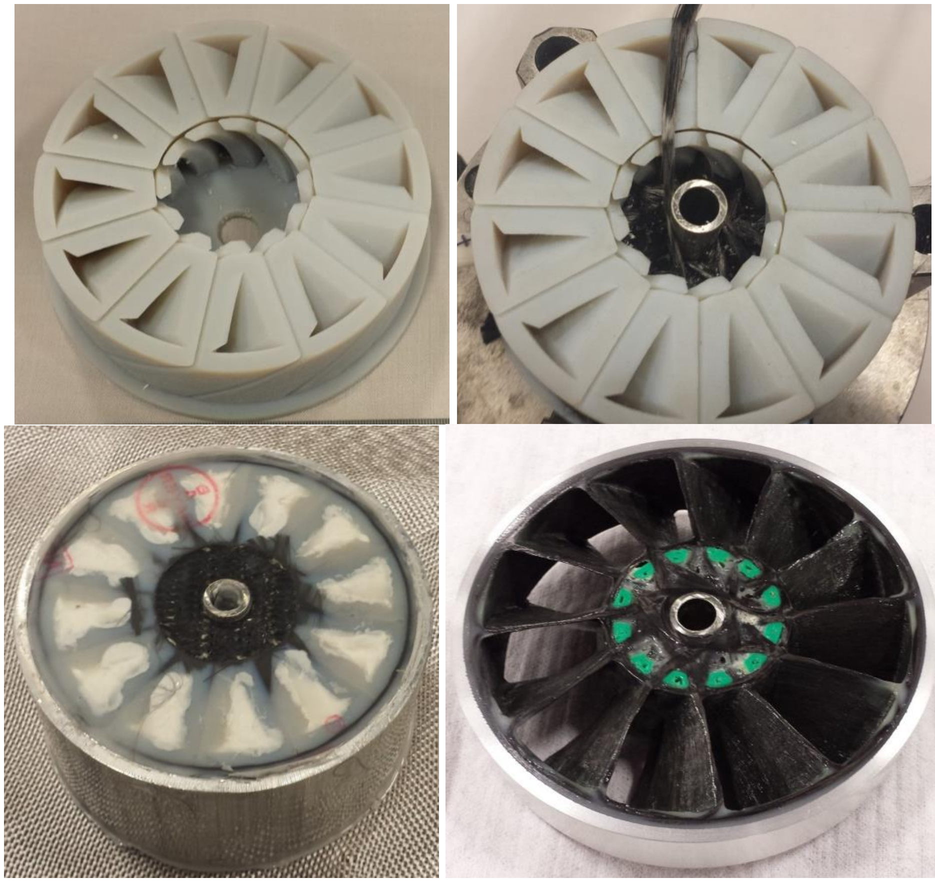

Figure 1.8. (a) 3-D printed mandrel. (b) carbon fiber winding. (c) mandrel post-winding after being dipped into epoxy/resin and cured. (d) Woven Wheel after removal from mandrel.

1.5.3. Rapid Customization and Manufacturing

Although this manufacturing process is still being refined and perfected, this additive manufacturing process allows for the time between design and production to be minimal. New designs derived from analytical models can be tested in CFD, a mandrel can be manufactured and wound in a matter of hours. This allows for faster, lower cost production and rapid customization. This added versatility lends itself well to the application of the technology for use as a water turbine. Individual hydroelectric applications are unique and are often custom projects, and the ability to adjust the Woven Wheel manufacturing technique to fit any required size is advantageous.

Currently only blade profiles with constant thickness can be manufactured using the Woven Wheel method. The turbine designs investigated in this thesis all have constant blade thickness from hub to shroud, and leading to trailing edge.

1.5.4. Outer Shroud Eliminates Tip Leakage and Reduces Fish Mortality

Fishes can suffer injuries and death passing through hydraulic turbines. This is considered a significant environmental concern when considering any new hydroelectric development [11]. Fish injuries and death while passing through hydraulic turbines is a result of rapid pressure changes along flow path, cavitation, narrow gaps between rotating parts and stationary structures, and fish collision with structures including turbine runner blades and guide vanes.

Traditional axial-flow turbines (such as Kaplan turbines) are not shrouded, there is a gap between the turbine runner and outer housing which is the most common source of the mortality of fish passing through hydraulic turbines [12]. Turbine manufactures like Voith have attempted to solve this problem by implementing design changes which reduce the factors listed above. Voith has developed a “Minimum Gap Runner” technology which features specially contoured and machined runner blades to minimize the gaps between the turbine runner blades and the hub, as well as the stationary outer housing. The minimization of the gap between turbine runner blades and the housing also reduces tip leakage, improving performance [13]. Computational Fluid Dynamics (CFD) is often used to ensure that cavitation, shear stresses, and rapid pressure changes are kept to a minimum.

Gaps between the turbine rotor blades and outer housing can lead to fish death. Companies like Voith have developed technologies for axial hydraulic turbines which reduce the size of this gap, however almost all axial hydraulic turbines do not have this feature [13]. Using the Woven Wheel as a hydraulic turbine reduces the risk of fish death as a result of the gap between rotor blades and the outer housing as the shroud is integrated into the design of the blades. This also reduces losses associated with tip leakage.

1.6. Definition of Turbine Type Investigated

This work explores the viability of using an axial turbine with simplified geometry for low head hydroelectric applications. Constraints were placed on the design to keep manufacturing costs as low as possible, and to allow the Woven Wheel method to be employed for manufacturing the turbine rotor. The turbines analyzed in this work have the following features:

- Axial flow
- Circular arc blade profile
- Constant thickness blade profile
- Constant OD/ID
- Shrouded rotor
- No inlet or outlet guide vane
- No-pre swirl, $C_{u1} = 0$

The performance of the hydro turbine designs tested in CFD could be improved by employing blade profiles, adjusting the OD/ID along the flow path axially, but these were not included in the designs, this was done to keep manufacturing production cost low and to make the designs applicable to the Woven Wheel manufacturing method. In this work turbines of this type referred to as CTPAT, or Constant Thickness Profile Axial Turbine.

The work in this thesis applies for turbine designs with shrouded rotors manufactured from metal as well as Woven Wheels. The CTPAT scheme is applicable with the modular Woven Wheel turbine concept which has been proposed. The use of constant thickness blade profiles makes the CTPAT scheme different from those turbines most commonly employed in the field. The analytical model described in section 2.3 was set up to obtain CFD boundary conditions which were applicable for a proposed application of a CTPAT turbine for use as a retrofit turbine unit to fit on the front of dam spillways.

1.7. Conservation of Energy

The first law of thermodynamics is applied through a control volume to obtain an equation for the steady flow energy balance for a turbine. A control volume representing a turbine is illustrated in Figure 1.9 below. For the analyses in this work, “1” represents the properties at the leading edge of the turbine, and “2” represents the properties at the trailing edge of the turbine. Equation 1-2 below shows the energy balance, where $\dot{Q}$ is the heat transfer from the surroundings to the control volume measured in Joules per second, h is mass-specific enthalpy, C is absolute flow speed, z represents the elevation above the datum, and $\dot{W}$ represents the power that is transferred from the fluid to the blades of the turbomachine via the shaft (shaft power).

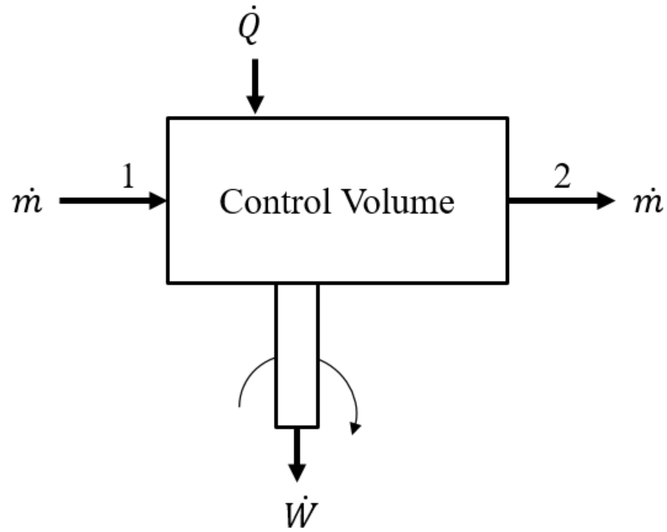

Figure 1.9. Turbomachine control volume

$$\dot{Q} - \dot{W} = \dot{m}\left[(h_2 - h_1) + \frac{1}{2}(C_2^2 - C_1^2) + g(z_2 - z_1)\right] \tag{1-2}$$

The heat transfer from the surroundings to the control volume $\dot{Q}$ is negligible for water turbines, and is assumed to be equal to zero. To derive an expression for the isentropic efficiency of the turbine, equation 1-2 is rewritten in differential form below in equation 1-3 [4]:

$$d\dot{W} = \dot{m}\left[dh + \frac{1}{2}d(c^2) + gdz)\right] \tag{1-3}$$

$\dot{W}_{max}$ is the total energy extraction from the fluid per second, and is the maximum possible power output of the turbine. For an isentropic process, $dh = \frac{dp}{\rho}$ [4]. $\dot{W}_{max}$ can then be expressed using equation 1-4:

$$\dot{W}_{max} = \dot{m}\left[\frac{(P_2 - P_1)}{\rho} + \frac{1}{2}(C_2^2 - C_1^2) + g(z_2 - z_1)\right] \tag{1-4}$$

For incompressible flow, the total energy extraction from the fluid per second $\dot{W}_{max}$ can be rewritten in terms of the total available head H, which takes into account gravitational potential energy, kinetic energy, and enthalpy difference, seen in equation 1-3, applied to the energy equation in equation 1-5 below [4]:

$$gH = \frac{P}{\rho} + \frac{1}{2}C^2 + gz \tag{1-5}$$

The expression for the total energy extraction from the fluid per second, $\dot{W_{max}}$, equation () can then be rewritten in terms of H, shown below in equation 1-6:

$$\dot{W_{max}} = \dot{m}g(H_1 - H_2) \tag{1-6}$$

The isentropic turbine efficiency η is defined as the ratio of the shaft power output $\dot{W}$ to the total energy extraction from the fluid per second $\dot{W_{max}}$, and defined below in equation 1-7 [4]. Isentropic turbine efficiency is referred to as "efficiency" in this work.

$$\eta = \frac{\dot{W}}{\dot{W_{max}}} = \frac{\dot{W}}{\dot{m}g(H_1 - H_2)} \tag{1-7}$$

The mass-specific form of the shaft power output $\dot{W}$ is denoted by $\tilde{e}$, measured in meters squared per seconds squared, $\tilde{e}$ is defined in equation 1-8 below:

$$\tilde{e} = \frac{\dot{W}}{\dot{m}} \tag{1-8}$$

Using equation 1-8, the expression for efficiency in equation 1-7 can then be rewritten in terms of the mass-specific shaft work $\tilde{e}$, shown below in equation 1-9:

$$\eta = \frac{\tilde{e}}{g(H_1 - H_2)} \tag{1-9}$$

A variable is defined, e, the mass-specific form of $\dot{W_{max}}$. e denotes the mass-specific work extracted from the fluid from the leading to trailing edge, which includes losses in the turbine, and is defined below in equation 1-10:

$$e = \frac{\dot{W_{max}}}{\dot{m}} = \frac{\tilde{e}}{\eta} = g(H_1 - H_2) \tag{1-10}$$

Work extraction from a hydraulic turbine can be expressed in terms of the total (stagnation) pressure, P_t. P_t can be expressed in terms of static pressure, dynamic pressure, and the gravitational head, shown in equation 1-11 below [4]:

$$P_t = \frac{P}{\rho} + \frac{1}{2}C^2 + gz \tag{1-11}$$

The mass-specific energy extracted from the fluid from leading to trailing edge, e, is expressed in terms of the total pressure P_t at leading and trailing edges in equation 1-12 below for incompressible flow for a hydraulic turbine:

$$P_{t2} = P_{t1} - e\rho \tag{1-12}$$

A portion of the total pressure drop across a turbine stage ($P_{t1} - P_{t2}$) is converted into useful shaft work ($\tilde{e}\rho$). The portion of the pressure drop that is not converted into shaft work are considered losses. The losses can be expressed using a reordered version of equation 1-12, in terms of the total loss coefficient ξ and the absolute velocity at the trailing edge, C_2, shown below in equation 1-13.

$$P_{t1} - P_{t2} = \tilde{e}\rho + \frac{1}{2}\rho\xi C_2^2 \tag{1-13}$$

Total loss coefficient ξ can be expressed in terms of its components, a sum of the sources of loss in a turbine stage, where $\xi_{profile}$ represents losses in the blade row, ξ_{exit} represents losses between the trailing edge and the outlet, ξ_{entry} represents losses between the turbine inlet and leading edge, expressed below in equation 1-14:

$$\xi = \xi_{entry} + \xi_{profile} + \xi_{exit} \tag{1-14}$$

The shaft power output of the turbine $\dot{W}$ can be calculated using the mass-specific shaft work $\tilde{e}$ and the mass flow rate $\dot{m}$, shown below in equation 1-15:

$$\dot{W} = \tilde{e}\dot{m} \tag{1-15}$$

1.8. Definitions of Geometry and Design Parameters

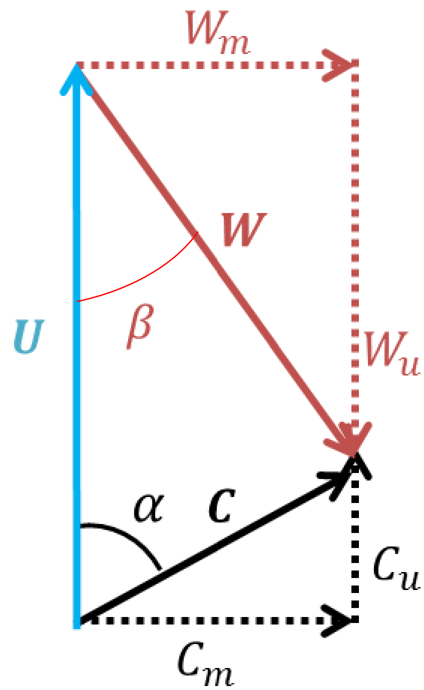

Figure 1.10. Example velocity triangle

The variables used to generate a turbine rotor design for CFD analysis are defined in this section. Absolute velocity of the turbine rotor is $\vec{U}$. The absolute velocity of the fluid is $\vec{C}$, and the velocity of the fluid relative to the rotor is $\vec{W}$, defined below in equation 1-16.

$$\vec{W} = \vec{C} - \vec{U} \tag{1-16}$$

The vectors $\vec{C}$ and $\vec{W}$ are often expressed in terms of their meridonial and tangential (wheel rotation direction) components. C_m is the absolute velocity of the fluid in the meridonial direction, and W_m is the flow speed in the meridional direction relative to the wheel. C_u is the absolute velocity of the fluid in the direction of the rotation of the wheel, and W_u is the flow speed in the rotation direction of the wheel relative to the wheel. Velocity triangles help to visualize how the velocities relate to each other. Figure 1.10 above shows an example velocity triangle. The magnitude of the absolute flow velocity, $C,$ is calculated using the meridonial and tangential velocity components shown below in equation 1-17:

$$C^2 = C_u^2 + C_m^2 \tag{1-17}$$

Similarly the magnitude of the relative flow velocity W can be calculated using the meridional and tangential relative velocity components, seen in equation 1-18:

$$W^2 = W_u^2 + W_m^2 \tag{1-18}$$

Absolute flow angle α is defined as the angle between the $\vec{C}$ vector and the $\vec{U}$ vector, and can be calculated using the components of the $\vec{C}$ vector, expressed below in equation 1-19:

$$\alpha = \cos^{-1}\frac{C_u}{C} = \; = \sin^{-1}(\frac{C_m}{C}) \tag{1-19}$$

Similarly the relative flow angle, β, is defined as the angle between the $\vec{W}$ vector and the $\vec{U}$ vector, and can be calculated using the components of the $\vec{W}$ vector, expressed below in equation 1-20:

$$\beta = \sin^{-1}\frac{W_m}{W} = \cos^{-1}(\frac{W_u}{W}) \tag{1-20}$$

Figure 1.11 below shows an example CTPAT axial turbine geometry, where h_b is the blade height, r_h is the inner (hub) radius, and r_s is the outside (shroud) radius of the turbine rotor, and ω is the angular velocity of the rotor. Position 1 represents the leading edge, position 2 represents the trailing edge.

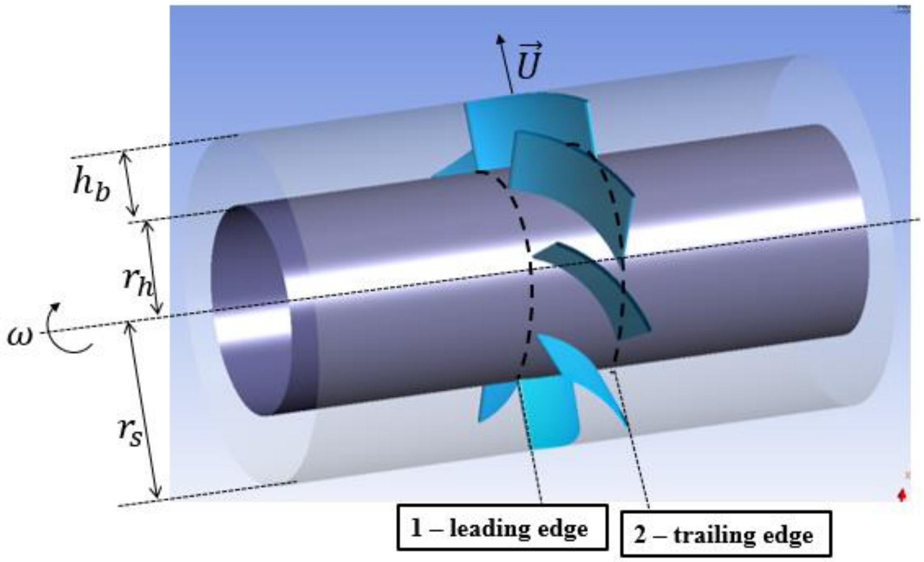

Figure 1.11. Axial turbine geometry parameters

For the analysis in this work, the outside (shroud) radius of the rotor, r_s, and the rotational speed of the rotor in RPM are all input. The hub-tip ratio γ is input as well. The inner (hub) radius r_h can be calculated using the shroud radius and the hub-tip ratio, shown in equation 1-21 below:

$$r_h = r_s \gamma \tag{1-21}$$

Angular velocity ω can be calculated using the rotational speed given in rotations per minute N_{rpm}, which was input for this analysis, using equation 1-22,then the tip speed of the wheel (U) can then be calculated using equation 1-23.

$$\omega = 2\pi \frac{N_{rpm}}{60} \tag{1-22}$$

$$U = r_s \omega \tag{1-23}$$

The tangential speed of the rotor for a position along the span is denoted by U_θ, where "θ" represents a position along the span, calculated using equation 1-24 below, where r_θ is the radial distance from the centerline to the position along the span being considered. This is different than the tip speed U in that tip speed uses outside radius. For example, the tangential speed of the rotor at the inner radius/hub is $U_h = r_h \omega$, calculated using the inner radius, r_h.

$$U_\theta = r_\theta \omega \tag{1-24}$$

The inner radius and outside radius of each turbine in this analysis were kept constant form leading to trailing edges. Thus the tip speed of the wheel is constant from the leading to trailing edges, so $U = U_1 = U_2$. For this analysis the thickness of the blades (t) and the number of blades (N_b) were also input. The thickness of the blades is constant from leading to trailing edge, and is also constant across the blade span. Blade height h_b is calculated for the IGV and rotor geometries using equation 1-25:

$$h_b = r_s - r_h \tag{1-25}$$

Meridional cross-sectional area A_m is then calculated for the axial rotor using equation 1-26:

$$A_m = \pi(r_s^2 - r_h^2) - t h_b N_b \tag{1-26}$$

Mass flow rate $\dot{m}$ can be calculated using the meridional cross-sectional area A_m, density ρ, and absolute meridonial flow speed C_m, shown below in equation 1-27:

$$\dot{m} = C_m A_m \rho \tag{1-27}$$

Equation 1-28 below is referred to as the equation of continuity, and states that mass flow rate, $\dot{m}$, stays constant from inlet to outlet of the turbomachine control volume. $\dot{m}$ stays constant from leading to trailing edge, and from inlet to outlet as there is no accumulation of water within the control volume. Equation 1-29 is a reordered version of equation 1-28, using the definition of mass flow rate in equation 1-27:

$$\dot{m}_1 = \dot{m}_2 \tag{1-28}$$

$$C_{m1} A_{m1} \rho_1 = C_{m2} A_{m2} \rho_2 \tag{1-29}$$

The mass flow rate of water flow ($\dot{m}$) as well as the density of the water (ρ) are input. Using these input properties and known geometry, meridional absolute flow speeds along the flow path can be calculated using equation 1-30 below, after rearranging the definition of mass flow rate expressed in equation 1-27:

$$C_m = \frac{\dot{m}}{A_m\,\rho} \tag{1-30}$$

Flow speed in the direction of the wheel relative to the wheel W_u is then calculated using the definition of the $\vec{W}$ vector equation 1-16 ,in the tangential direction, seen below in equation 1-31:

$$W_u = U - C_u \tag{1-31}$$

Similarly by applying equation 1-16 in the meridional direction W_m is calculated using equation 1-32 below:

$$W_m = C_m \tag{1-32}$$

Figure 1.12 below illustrates an example CTPAT axial turbine blade cascade with velocity triangles at leading and trailing edges. Geometric parameters are defined, where b is the axial blade length, s is the spacing between blades, c is the chord length, and t is the blade thickness. Circular arc blade profiles are used for the analytical model and the CFD simulations. For this analysis geometric parameters t, N_b, r_o, r_i, b are each provided as an input. For the analyses in this work, “1” represents the properties at the leading edge, and “2” represents the properties at the trailing edge of the turbine.

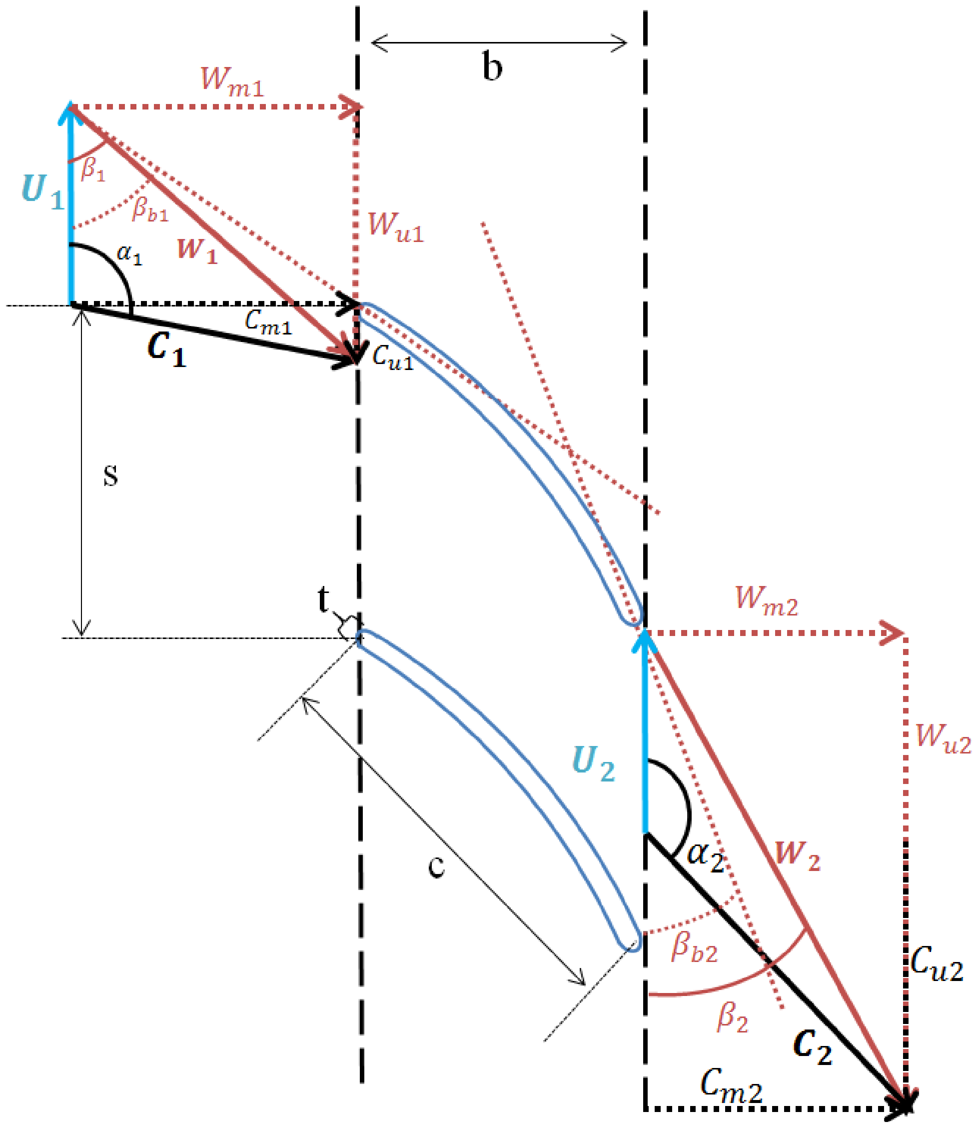

Figure 1.12. Turbine blade cascade with velocity triangles

Blade spacing s can be calculated using equation 1-34 below, which uses known geometric inputs and mean radius r_m, which is calculated using equation 1-33 below:

$$r_m = \sqrt{\frac{(r_h^2 + r_s^2)}{2}} \tag{1-32}$$

$$s = \frac{2\pi r_m}{N_b} \tag{1-33}$$

Flow does not follow the blade path perfectly, the difference between the ideal trailing edge relative flow angle if flow followed the blades perfectly and the actual trailing edge relative flow angle is referred to as the outlet deviation, δ', defined in equation 1-34 below, where β_{b2} is the angle between the blade at the trailing edge and the $\vec{U}$ vector, and β_2 is the relative flow angle at the trailing edge:

$$\delta' = \beta_2 - \beta_{b2} \tag{1-34}$$

Similarly the incidence is the difference between the leading edge flow angle and the blade leading edge angle, shown below in equation 1-35:

$$i' = \beta_1 - \beta_{b1} \tag{1-35}$$

The mass-specific shaft work $\tilde{e}$ can be related to the rotor speed and absolute tangential velocity using the Euler turbomachinery work equation, derived using conservation of angular momentum. Conservation of momentum equates the sum of external forces acting on a fluid to the rate of change of momentum. Applied to turbomachinery, the force applied by a fluid onto the blades is caused by the acceleration of the fluids passing through the blades [4]. Equation 1-36 below applies conservation of momentum in the x-direction for a control volume where fluid enters with uniform velocity C_{x1} in the x direction and leaves with uniform velocity C_{x2} in the x direction, m represents the mass of a fluid element, and F_x represents forces acted on the control volume in the x-direction [4]:

$$\sum F_x = \frac{d}{dt}(mC_x) = \dot{m}(C_{x2} - C_{x1}) \tag{1-36}$$

Conservation of momentum can be applied to relate change in tangential flow speed to the change in angular momentum and shaft power. The sum of all moments of all forces acting on a system about an axis is equal to the time rate of change of angular momentum about that axis [4]. This is seen below in equation 1-37, where τ_a is the time rate of change of angular momentum about axis A, r is the distance between the center of mass to the rotation axis A and C_θ is the component of velocity perpendicular to both the axis A and the radius vector:

$$\tau_a = m\frac{d}{dt}(rC_\theta) \tag{1-37}$$

Equation 1-37 can then be applied for an arbitrary turbomachine, with radius at leading edge r_1, radius at trailing edge r_2, with tangential velocity at the leading and trailing edges C_{u1} and C_{u2} respectively for one dimensional steady flow, shown below in equation 1-38 [4]:

$$\tau_a = \dot{m}(r_2 C_{u2} - r_1 C_{u1}) \tag{1-38}$$

Applying the definition of tip speed U by plugging in $r = \frac{U}{\omega}$ to equation 1-38, equation 1-39 is formed:

$$\tau_a \omega = \dot{m}(U_2 C_{u2} - U_1 C_{u1}) \tag{1-39}$$

The product $\tau_a \omega$ is equal the shaft power output of the turbine $\dot{W}$. Using equation 1-8, equation 1-39 is rearranged in terms of the mass-specific shaft work $\tilde{e}$, shown below in equation 1-40:

$$\tilde{e} = U_2 C_{u2} - U_1 C_{u1} \tag{1-40}$$

The above is a form of the Euler turbomachinery work equation, which is valid for steady, adiabatic flow [4]. For the analysis in this work, tip radius stays constant from leading to trailing edge such that $U_1 = U_2$. Equation 1-40 can then be simplified to form equation 1-41:

$$\tilde{e} = U(C_{u2} - C_{u1}) \tag{1-41}$$

By rearranging equation 1-41 and applying equation 1-10, $\tilde{e}$ can then be expressed in terms of the total head H difference from leading to trailing edge, shown below in equation 1-42:

$$U(C_{u2} - C_{u1}) = \eta g(H_1 - H_2) \tag{1-42}$$

1.9. Turbine Cascade Forces

An example pressure distribution across a turbine stage is shown below in Figure 1.13, where P_p is the pressure curve on the pressure side of the blade, P_s is the pressure curve on the suction side.

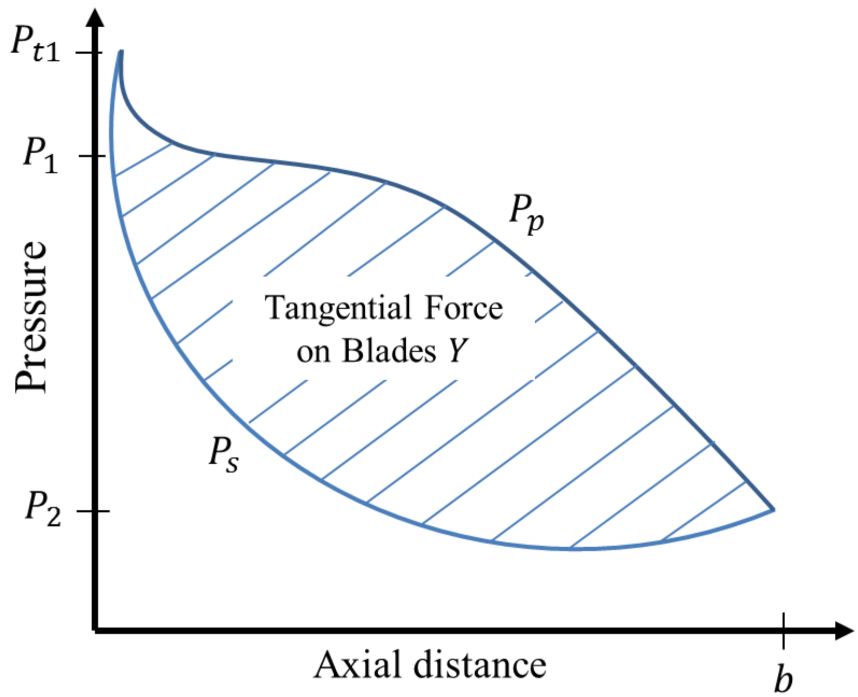

Figure 1.13. Pressure distribution across a turbine stage

The area between the P_p and P_s curves in Figure 1.13 is equal to the tangential force Y acting on the flow imparted by a single blade, calculated by integrating the pressure difference from the leading edge to the trailing edge, expressed below in equation 1-43.

$$Y = b \int_0^1 (P_p - P_s)\ d\left(\frac{x}{b}\right) \tag{1-43}$$

To derive an alternate form of equation 1-43, conservation of angular momentum is applied in the tangential direction, the tangential force can be expressed using equation 1-45 assuming constant axial velocity. First $\Delta\dot{m}$ is calculated, which represents the mass flow rate through a single blade passage, using equation 1-44 [4]:

$$\Delta\dot{m} = C_m s h_b \rho \tag{1-44}$$

$$Y = \Delta\dot{m}(W_{u2} - W_{u1}) \tag{1-45}$$

Force in the axial direction F_x can be derived using conservation of momentum, written below in equation 1-46, assuming axial velocity stays constant from leading to trailing edge:

$$F_x = (P_1 - P_2) s h_b \tag{1-46}$$

These forces can be used to calculate lift and drag forces F_l and F_d on the blades. Figure 1.14 below shows an example turbine blade cascade with blade forces.

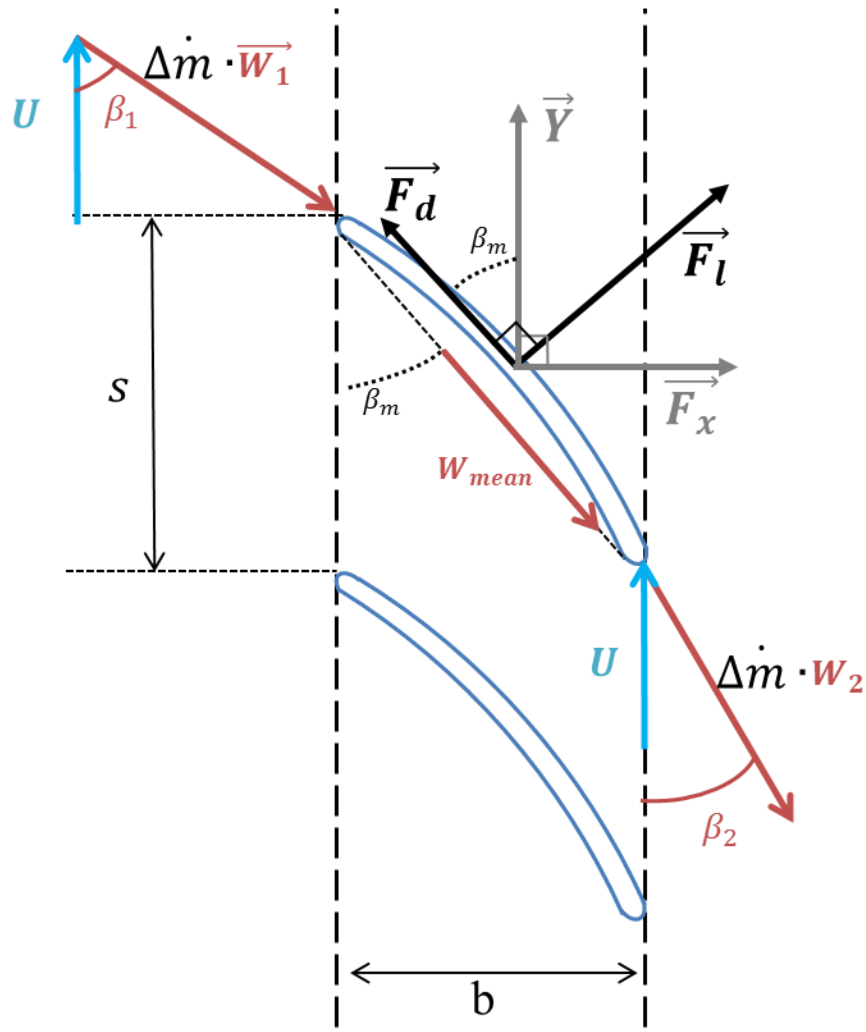

Figure 1.14. Example turbine blade cascade with blade forces

First mean flow angle β_m is calculated using equation 1-47, necessary for the calculation of lift and drag forces.

$$\tan\beta_m = \frac{1}{2}(\tan\beta_1 + \tan\beta_2) \tag{1-47}$$

Mean relative velocity W_{mean} can then be calculated using the mean relative flow angle β_m and the relative meridional velocity W_m, shown below in equation 1-48:

$$W_{mean} = W_m / \sin\beta_m \tag{1-48}$$

Lift and drag forces F_l and F_d can be calculated using equation 1-49 and equation 1-50 respectively, below:

$$F_l = F_x \cos\beta_m + Y\sin\beta_m \tag{1-49}$$

$$F_d = \text{Y}\cos\beta_m - F_x \sin\beta_m \tag{1-50}$$

Tangential force coefficient C_Y, axial force coefficient C_x, lift coefficient C_l, and drag coefficient are expressed in equations 1-51, 1-52, 1-53, and 1-54 respectively. They are useful non-dimensional coefficients which are a measure of the blade forces defined in equations 1-45, 1-46, 1-49, and 1-50 respectively, compared to the mean dynamic pressure , $\frac{\rho}{2}W_{mean}^2$, multiplied by the area on which it acts, sh_b.

$$C_Y = \frac{Y}{\frac{\rho}{2}W_{mean}^2 sh_b} \tag{1-51}$$

$$C_x = \frac{F_x}{\frac{\rho}{2}W_{mean}^2 sh_b} \tag{1-52}$$

$$C_l = \frac{F_l}{\frac{\rho}{2}W_{mean}^2 sh_b} \tag{1-53}$$

$$C_d = \frac{F_d}{\frac{\rho}{2}W_{mean}^2 sh_b} \tag{1-54}$$

1.10. Dimensionless Coefficients

1.10.1. Flow and Capacity Coefficients

The flow coefficient, ϕ, is a non-dimensional coefficient that depends on flow rate and rotational speed. The flow coefficient is used to compare different types of turbines. It relates the axial flow velocity to the speed of the blade, and is defined below in equation 1-55 [15]:

$$\phi = \frac{C_m}{U} \tag{1-55}$$

The capacity coefficient, ϕ', similar to the flow coefficient, is a non-dimensional parameter which is effected by the rotational speed, rotor diameter, and flow rate. The capacity coefficient is defined below in equation 1-56:

$$\phi' = \frac{\dot{V}}{ND^3} \tag{1-56}$$

1.10.2. Blade Loading and Head Coefficients

The blade loading coefficient ψ provides a measure of the work extraction for a turbine stage. The blade loading coefficient relates the mass-specific shaft work $\tilde{e}$ to the blade tip speed U. is defined below in equation 1-57: [4].

$$\psi = \frac{\tilde{e}}{U^2} \tag{1-57}$$

The equation is rearranged for an adiabatic axial water turbine with constant shroud radius, plugging in equation 1-10 into equation 1-57 to obtain equation 1-58 below: [4]

$$\psi = \frac{\tilde{e}}{U^2} = \frac{\eta g H}{\pi^2 N^2 r_s^2} \tag{1-58}$$

The head coefficient ψ' is similar to the blade loading coefficient in that it relates the work extraction to the rotational speed. However, blade loading coefficient ψ includes isentropic efficiency in the expression, while head coefficient ψ' uses total work extraction from the fluid,

e, in the expression. The head coefficient ψ' is defined below for an axial water turbine with constant shroud radius using equation 1-59:

$$\psi' = \frac{e}{(ND)^2} = \frac{gH}{(ND)^2} \tag{1-59}$$

Turbines which extract more work at a low tip speed have higher blade loading and head coefficients.

1.10.3. Specific Speed

Specific speed is a non-dimensional quantity that is used to describe and categorize turbomachinery. Specific speed, also called shape parameter, is discussed by Horlock [15] as a useful tool to help select the type of machine that will give highest efficiency for a given application. The specific speed was derived by raising the head and capacity coefficients to a power, eliminating diameter from the expression [16]. The specific speed takes into account rotational speed, flow rate, and total mass-specific work extracted from the fluid, where N is in units of rotations/second. For a water turbine with incompressible flow, the mass-specific work done on the fluid from leading to trailing edge, e, can be expressed in terms of total available head H. Specific speed N_s is defined below in equation 1-60 [15]:

$$N_s = \frac{\phi'^{\frac{1}{2}}}{\psi'^{\frac{3}{4}}} = \frac{\left(\frac{\dot{V}}{ND^3}\right)^{\frac{1}{2}}}{\left(\frac{e}{(ND)^2}\right)^{\frac{3}{4}}} = \frac{N\dot{V}^{\frac{1}{2}}}{e^{\frac{3}{4}}} = \frac{N\dot{V}^{\frac{1}{2}}}{gH^{\frac{3}{4}}} \tag{1-60}$$

It should be mentioned the head in this case is the total designed head of the turbine system, including losses. This form of specific speed is in units of rotations [4] . Another form of specific speed, Ω_s, uses the angular speed of the turbine measured in radians per second instead of rotations per second [4], defined below for incompressable flow in equation 1-61:

$$\Omega_s = \frac{\omega \dot{V}^{\frac{1}{2}}}{(gH)^{\frac{3}{4}}} \tag{1-61}$$

Horlock stated there is an optimal value of the specific speed for a given type of machine, independent of size, at which efficiency is highest [15]. Figure 1.15 illustrates this concept, showing there is a specific speed at which peak efficiency is reached.

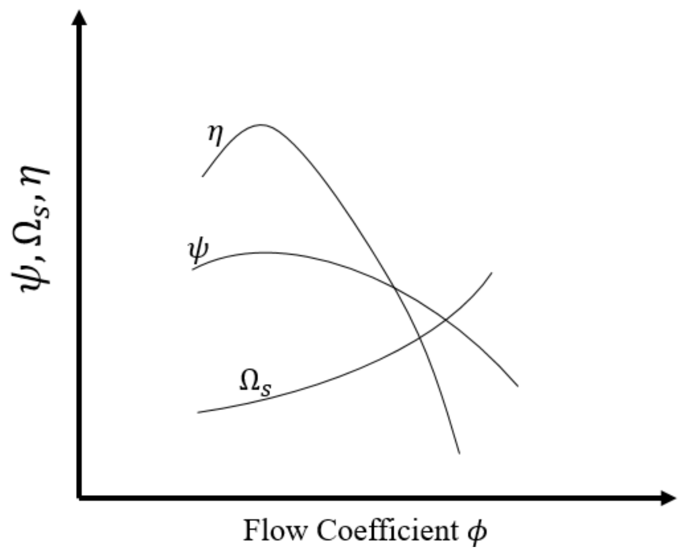

Figure 1.15. Example efficiency curve for turbine for specific speed N_s [15]

1.10.4. Specific Diameter

Specific diameter, D_s, is also used to describe and categorize turbines. The specific diameter was defined by using the head and capacity coefficients, similar to the specific speed. The head and capacity coefficients can be raised to a power to eliminate rotational speed from the equation [4]. This is shown below in equation 1-62 [4]:

$$D_s = \frac{\psi'^{\frac{1}{4}}}{\phi'^{\frac{1}{2}}} = \frac{D(gH)^{\frac{1}{4}}}{\dot{V}^{\frac{1}{2}}} \tag{1-62}$$

1.11. Cordier Diagram and Line

Dixon stated that once specific speed is determined; the ideal machine type can be selected using the Cordier diagram [4]. The Cordier diagram is also often used to select a specific speed or specific diameter for a given type of machine where efficiency is predicted to be highest. Otto Cordier carried out an experimental analysis of high efficiency turbomachines during the 1950s, and placed their data on a plot showing specific speed Ω_s against specific diameter D_s, and defined a trend line on a diagram showing where the highest efficiency turbomachines lie [17]. This curve is referred to as the "Cordier line".

Each type of machine has a range of specific speeds in which they perform with highest efficiency [15]. Machines with high head and low flow are on the right side of the Cordier diagram, while low head, high flow machines are on the left. The Cordier diagram with Cordier line is shown below in Figure 1.16. Circles are added to indicate where different types of machines typically lie on the diagram. Lines from Wright are placed above and below the Cordier line which indicate the accuracy/margin [18]. Wright divided the Cordier diagram into six regions [18]. The first region A, with specific speed between 6 and 10 and specific diameter between .95 and 1.25, propeller-type machines are typically used. Region B has specific speed between 3 and 6, specific diameter between 1.25 and 1.65. Wright mentioned this region has primarily axial turbomachines, like axial fans, axial pumps, and shrouded propellers. Region C contains machines with speed between 1.8 and 3, and specific diameter between 1.65 and 2.2. Ducted axial machines or multistage axial machines typically operate in this region. Region D includes machines with specific speeds between 1.0 and 1.8, and specific diameter between 2.2 and 2.8. Mixed flow pumps, blowers, mixed flow hydraulic turbines operate in this region. Region E includes machines with specific speed between .7 and 1, and specific diameter between 2.8 and 4. Centrifugal fans, pumps, heavy duty blowers, compressors operate in this range. Region F has specific speeds below .7 and specific diameters above 4. High pressure blowers, centrifugal compressors, high head pumps operate in this region.

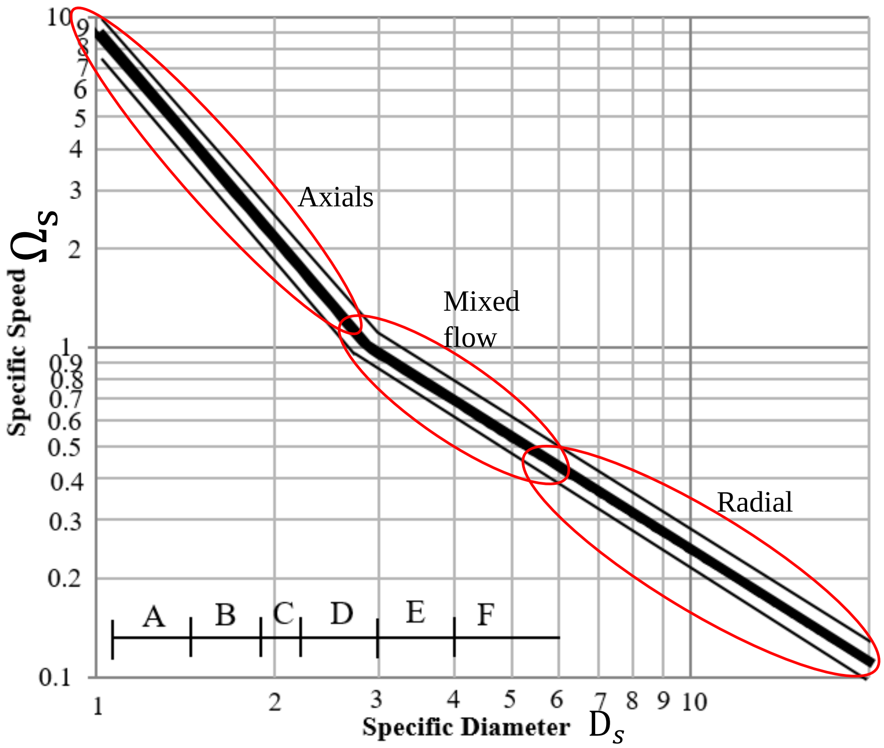

Figure 1.16. $D_s - \Omega_s$ *diagram with Cordier line and typical machine type*

Balje compiled test data and specifications from 92 water turbines built between 1940 and 1974 and placed them on the $D_s - \Omega_s$ chart, superimposed over the Cordier line,. The water turbines included in that test data have specific speeds between 2 and 6. The water turbines are close to the line originally defined by Cordier [15].

The below Figure 1.17 shows the Cordier line alongside eight modern axial hydro turbines manufactured by Voith Hydro, the specifications of which were obtained on the company website [20].

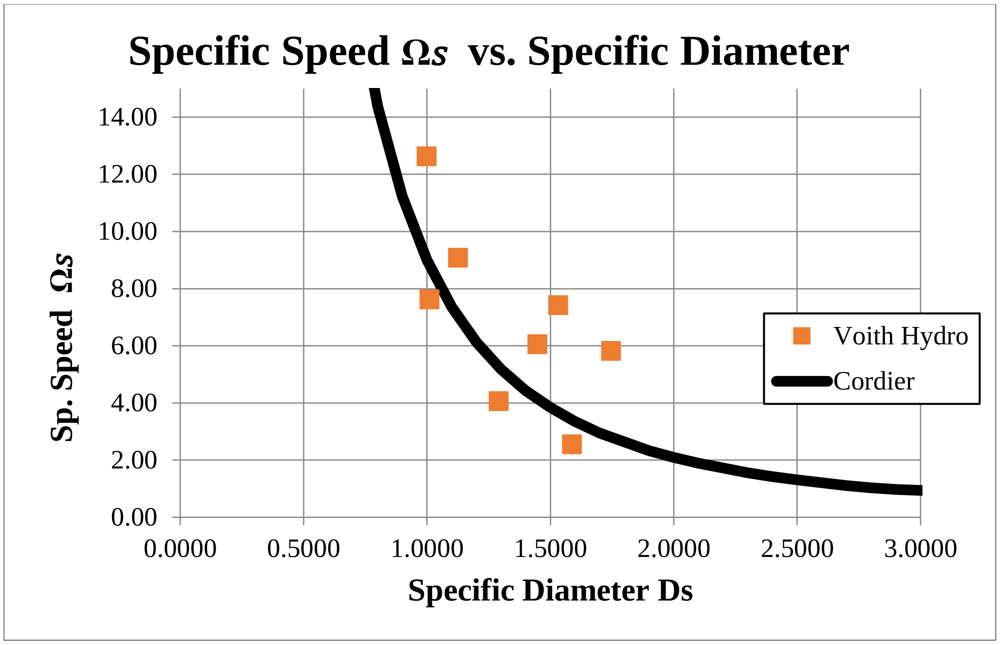

Figure 1.17. $D_s\!-\!\Omega_s$ diagram with Voith Hydro turbines with Cordier line

1.11.1. Effect of Flow, Loading Coefficients on Cordier Diagram Position

A turbine design's position on the $\mathrm{D_s}\!-\!\Omega_\mathrm{s}$ diagram relative to the Cordier line can be fully defined by two dimensionless coefficients, Flow coefficient ϕ and blade loading coefficient ψ. The below figures show the Cordier diagram with lines of constant ϕ (Figure 1.18) and ψ (Figure 1.19) superimposed.

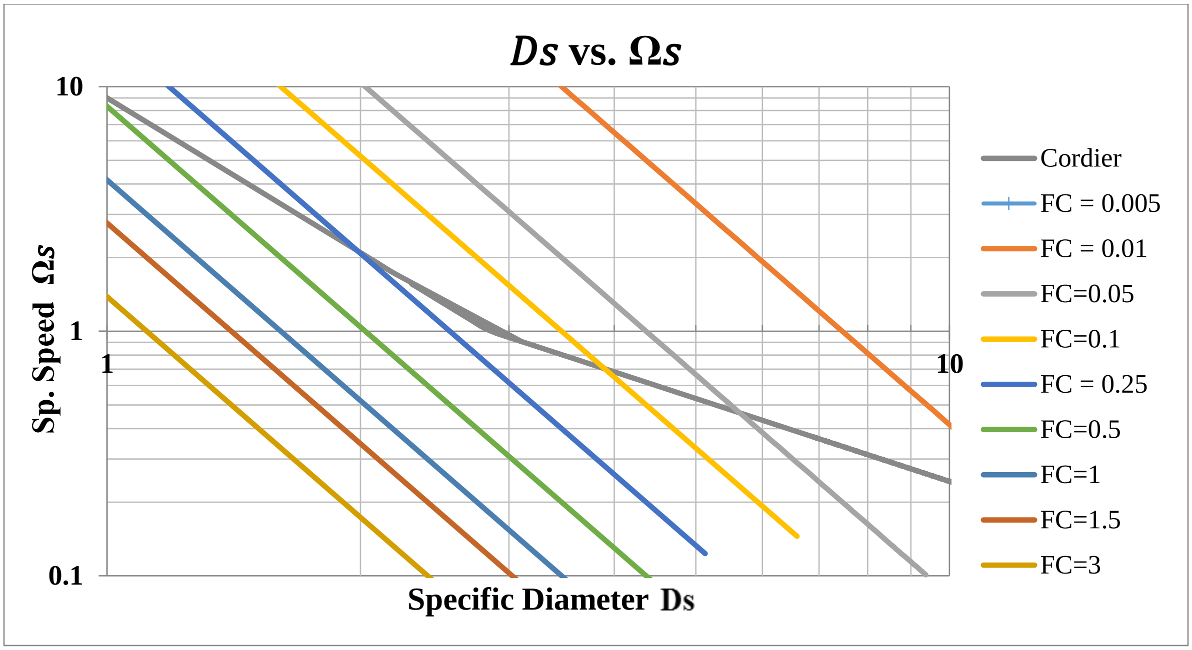

Figure 1.18. $D_s - \Omega_s$ diagram with Cordier line, lines of constant flow coefficient ϕ

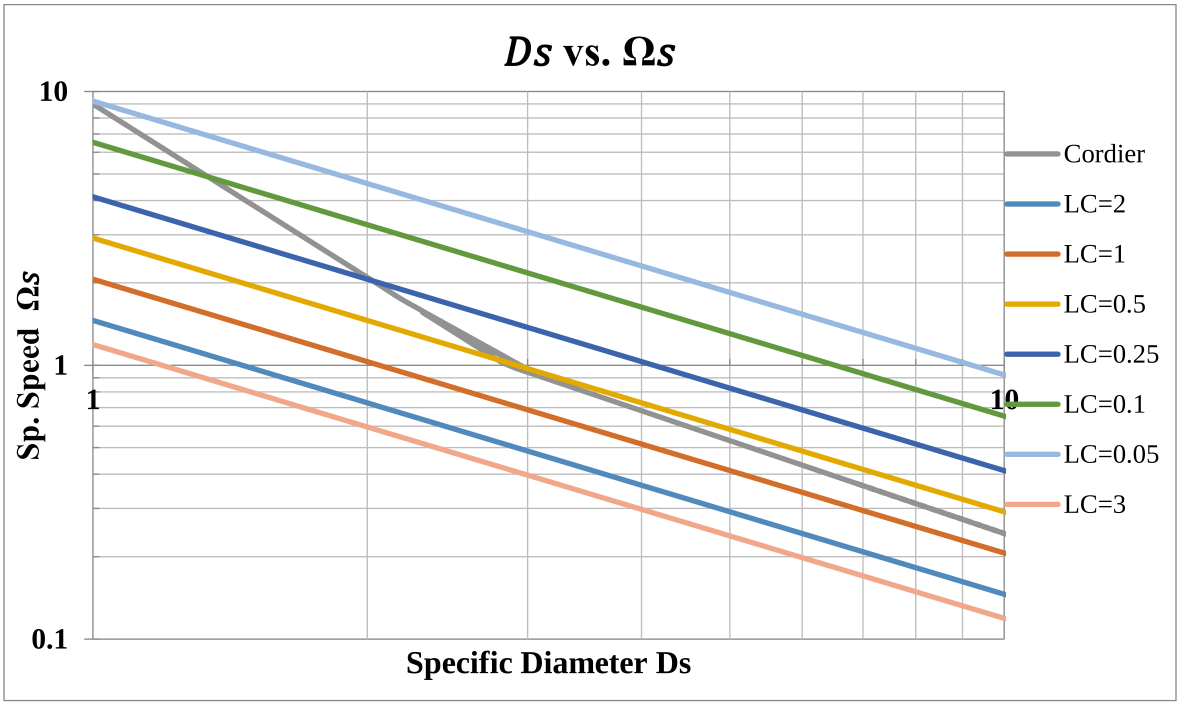

Figure 1.19 $D_s - \Omega_s$ diagram with Cordier line, lines of constant blade loading coefficient ψ

Turbine designs with high blade loading and flow coefficients have both low specific speed and specific diameter, are located on the lower left side of the $D_s - \Omega_s$ diagram, below and to the left of the Cordier line. Designs with low loading and flow coefficients are located above and to the right of the Cordier line.

1.11.2. Using Cordier Diagram as a Design Tool

Wright recommended using the Cordier line as a design tool to help decide what type of machine to use for a particular application, or to pick optimal values of either specific diameter or specific speed given one of the two. In Fluid Machinery, Performance and analysis, Wright stated: "When it is necessary to meet certain requirements in volume flow rate and pressure rise, one can follow the overall trend prediction of the Cordier diagram to help decide what type of machine will perform the job. For an initial selection of speed and known fluid density, one can estimate the specific speed. Enter the diagram at Ω_s, and determine a workable value for the machine size by choosing a value near or on the "Cordier line". This initial procedure will indicate both the size and type of machine one should be considering and the highest value of efficiency one can reasonably expect to achieve". [18] Wright stated that by using designs on the Cordier line highest efficiency can be achieved: "The efficiency band represents the best total efficiency that can reasonably be expected" [18]. Balje stated that efficient turbomachines are located close to the Cordier line [19]. Balje applied a curve fit to the data to derive an equation to pick optimal specific speed given specific diameter, which place the design on the Cordier line, the equations are shown below in equations 1-63 and 1-64 below [19]:

$$\Omega_s \cong 9.0 D_s^{-2.103} \text{ for } D_s < 2.8 \tag{1-63}$$

$$\Omega_s \cong 3.25 D_s^{-1.126} \text{ for } D_s \geq 2.8 \tag{1-64}$$

Adhikari et. al. described using the Cordier line as a starting point to help pick axial water turbine diameter given specific speed [21]. Given a flow rate, head, and desired diameter, the Cordier line can be used to pick an optimal specific speed, which then defines the RPM of the turbine. For example, for a turbine with a rotor diameter of .4 m, head of 2 meters, and flow rate of .46 $\frac{m^3}{s}$, the specific diameter is 1.22. Then the Cordier line recommendation is used to select the specific speed of 5.9. This gives a rotational speed of 737 RPM. Doing this in reverse gives a recommended diameter given rotational speed, head, and volume flow rate. For example, a 170 RPM turbine with head of 2 meters, a volume flow rate of .46 $\frac{m^3}{s}$, specific speed is 1.37. Using the Cordier diagram to pick optimal specific diameter of 2.2. Using equation 1-62 and solving for diameter gives an outside diameter of .7 meters.

1.11.3. Operating below the Cordier Line

The Cordier line can be used to pick a recommended specific diameter or specific speed given one of the two, however using the Cordier line for CTPAT turbines for this purpose results in recommendations of specific speed that may be larger than necessary for the application. Although there are correlations available within literature for predicting efficiency of specific types of hydraulic turbines at points off of the Cordier line, there will be no literature available for turbines with a new design, so it can be advantageous to test the effect of specific speed on efficiency when considering a new type of machine, like CTPAT.

Although literature suggests that the Cordier line provides a reasonable estimation of the specific speed at which a given machine will perform at peak efficiency. Korpela noted that turbines with low specific speed are better suited for radial turbines, and as specific speed increases axial turbines perform with higher efficiency [16]. Dixon mentioned that the Cordier line is a mean curve based upon data from a large number of machines Cordier compiled, and “it is possible to diverge from the line and still obtain high performance pumps, fans and compressors” [4]. However Cordier and Balje’s recommendations suggest that turbomachines should perform with higher efficiency when they lie on the Cordier line. Therefore it makes sense to test whether this applies for CTPAT turbines.

This work investigates the viability of the CTPAT turbine scheme for low head hydro, at specific speeds above and below that recommended by the Cordier line. This work investigates whether designs of this type within the range of specifications tested below the Cordier line (lower than recommended specific speed) perform any worse than designs on the Cordier line.

1.12. Literature Recommendations on Blade Loading and Flow Coefficients

Water turbines are often categorized by their blade loading coefficient ψ and flow coefficient ϕ. The Smith efficiency chart, shown below in Figure 1.20, was compiled using a large set of gas turbine test data to correlate head coefficient ψ' and flow coefficient ϕ to efficiency for a turbines with constant axial velocity [22]. Each turbine was tested at different operating points to find its point of highest efficiency, and the flow coefficient and loading coefficient were plotted at that point. Although the original diagram was published in 1965, the Smith diagram is still used today for preliminary turbine design, as more modern turbine designs follow the same efficiency vs. flow and head coefficient trends [23].

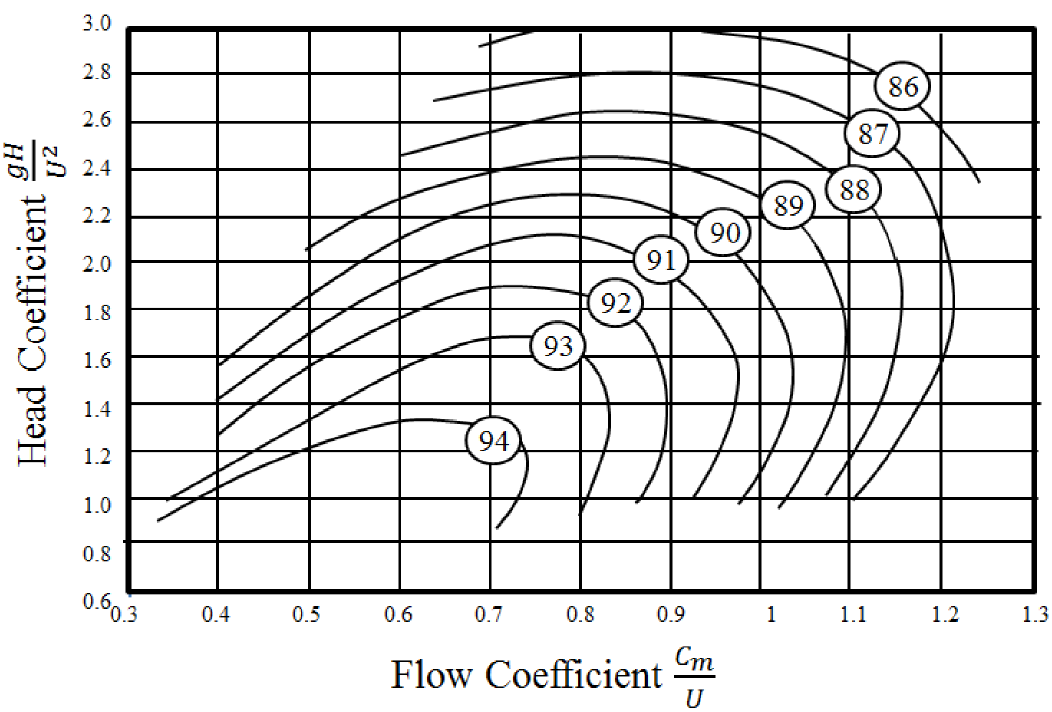

Figure 1.20. Smith loading vs. Flow coefficient diagram [22]

Smith's work suggests that as flow coefficient ϕ and head coefficient ψ' are increased, efficiency tends to decrease. The same relationship applies for capacity coefficient ϕ' and the blade loading coefficient ψ. Turbines with higher flow coefficients have higher flow velocities relative to blade speed, this tends to increase losses as there is a smaller acceleration through the blade path, that acceleration is usually beneficial as it minimizes boundary layer growth or secondary flows [24]. When head coefficient is increased, the change in flow tangential velocity becomes larger, which tends to increase loss. [4]

The Smith diagram is often used to choose optimum values of flow coefficient and blade loading coefficient given one of the two coefficients. Subsequent tests by Kacker and Okapuu confirmed the chart is useful for preliminary turbine design [25]. The diagram recommends values of flow coefficient and head coefficient that can offer higher performance, less flow separation and losses. However this does not mean that values of flow coefficient and head coefficient have to lie within recommended ranges in order to be considered acceptable designs [24]. The specifications of the axial turbines simulated lie both inside and outside of the recommendations of the Smith diagram and the Cordier line.

Smith's diagram was derived using gas turbine data and compressible flow, however the same trend applies for water turbines and incompressible flow, increasing flow coefficient and loading coefficient is correlated with decreased efficiency [15]. Figure 1.21 shows the range of typical flow coefficient ϕ and and blade loading coefficients ψ for different types of hydraulic turbines from Horlock. Flow coefficients for Kaplan and Francis turbines rarely reach above .6, and blade loading coefficients rarely reach above 2 [15].

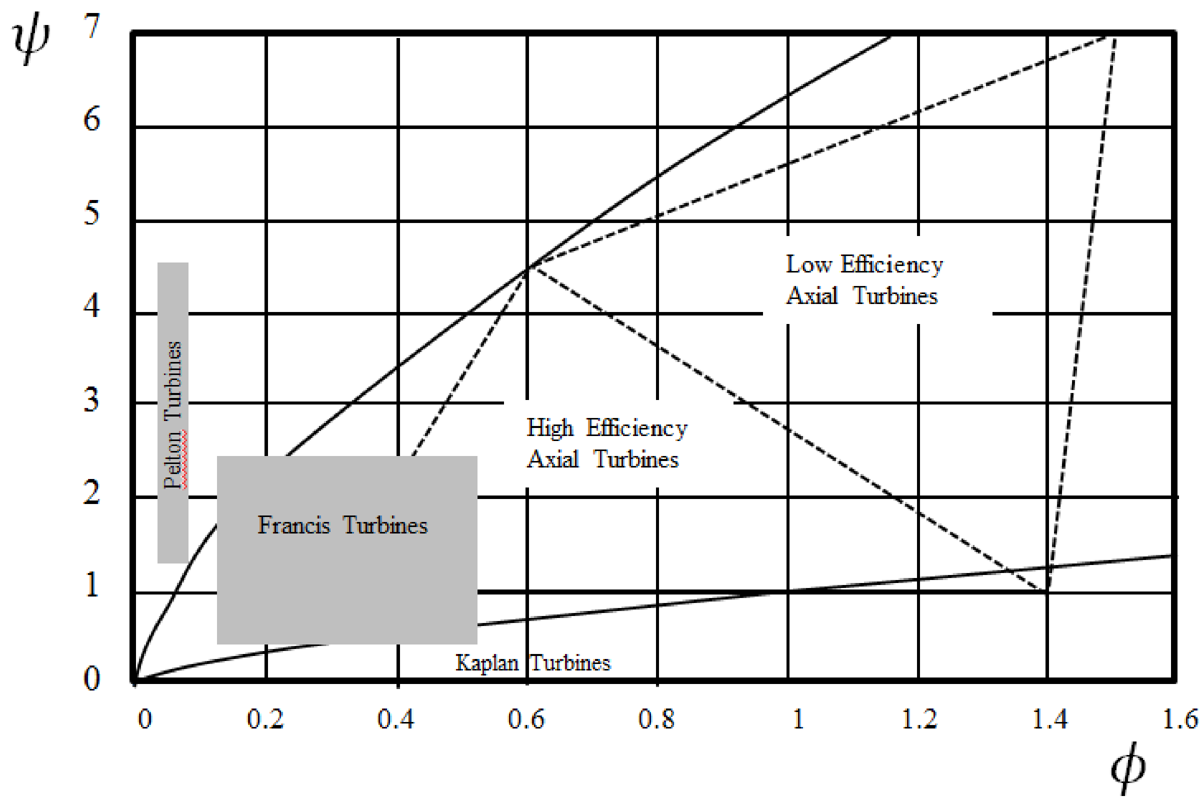

Figure 1.21. Blade loading and flow coefficients for different types of hydraulic turbines [15]

1.13. Cost Advantages of Designs With High Flow and High Loading Coefficients

Losses tend to increase with increasing blade loading and flow coefficients, however turbines with higher blade loading and flow coefficients can be produced for lower cost. Turbines with high flow coefficient generally have a smaller cross-sectional area compared to those with low flow coefficients, so turbines with lower ϕ tend to have increased turbine machining costs and weight [23]. Turbines with higher loading coefficient require fewer stages to achieve the same work extraction, and can extract more head for the same number of stages. Reducing the number of stages required for a turbine decreases part count, reducing weight, capital cost and operating cost. Industrial gas turbines are usually designed to maximize efficiency, so they generally have low flow and loading coefficients. Aerospace engines are usually designed for higher blade loading and high flow coefficient as the engine weight is of highest importance [23]. For aero engines, optimum value of ψ is between 1.5 to 2.5, and φ

ranges from 0.8 to 1.2. This contrasts with industrial gas turbines which typically have ψ between 1.0 to 1.5, and φ from 0.4 to 0.8 [23].

Smith, in his paper defining his diagram, stated that in practice the designer should use the highest possible feasible values of blade loading and flow coefficient, and has to “strike a compromise between the conflicting requirements of efficiency versus weight and cost” [22]. A critical part of turbine selection is to weigh turbine efficiency with capital cost, and designs which are less costly to produce, but have lower efficiencies can be considered acceptable for many applications. This is especially true for low-head hydro applications, the revenue generated from power is often not enough to justify large capital expenses for the most efficient turbines.

1.14. Zweifel Lift Coefficient

The Zweifel coefficient, also referred to as the Zweifel lift coefficient or Zweifel tangential force coefficient, Z, is often used to find the optimal blade spacing where losses are predicted to be lowest. The blade solidity, $\frac{s}{b}$, is the ratio of the blade spacing s to the axial blade length b. The solidity and has a large effect on the friction and losses resulting from deceleration on the suction side (diffusion) in the blade row. The Zweifel coefficient recommendations in literature can be used to pick a value of $\frac{s}{b}$ at which it is predicted that minimum friction losses and losses resulting from diffusion will occur [4]. If the spacing between blades is too small, the flow follows the blade with low deviation, but losses from friction are higher. If the spacing between blades is too high however, friction losses are low but the load distributed per blade increases, and losses resulting from diffusion increase [4]. Diffusion is undesirable in a turbine blade row, this is because the adverse pressure gradient, especially for large fluid deflections, makes boundary layer separation more probable [4].

The losses in the turbine from leading to trailing edge can be expressed in terms of the profile loss coefficient, $\xi_{profile}$. Profile losses are a function of losses as the result of friction and diffusion, such that $\xi_{profile} \cong \xi_{friction} + \xi_{diffusion}$. Schoberi stated that for every turbine design there is a value of $\frac{s}{b}$ where overall profile loss coefficient $\xi_{profile}$ is minimum [14]. Figure 1.22 below shows profile loss coefficient at differing blade spacing/chord length ratios, as the result of diffusion and friction.

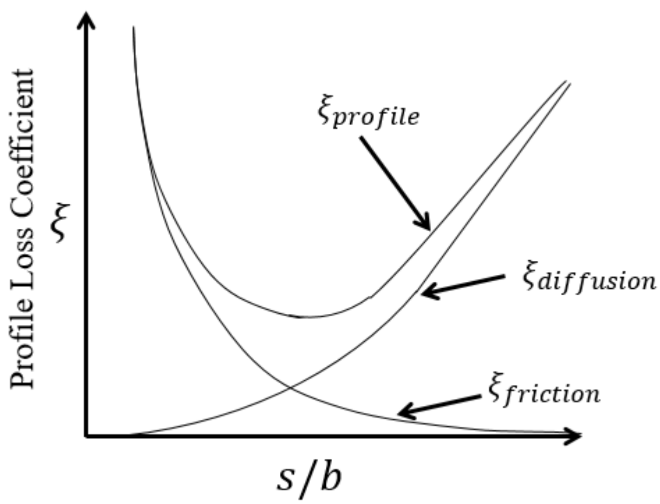

Figure 1.22. Profile loss coefficient vs. s/b ratio resulting from separation and friction [14]

Zweifel stated that "the ratio of an 'actual' to an 'ideal' tangential blade loading has an approximately constant value for minimum losses" [26]. Y denotes the actual tangential force per blade, previously defined in equation 1-43, and Y_{id} is the ideal tangential force per blade. The Zweifel coefficient Z is defined using the below equation 1-65:

$$Z = \frac{Y}{Y_{id}} \tag{1-65}$$

The tangential force imparted per blade, Y, is equal to the area between the pressure and suction curves in Figure 1.13, and can be calculated using equation 1-43. Y can also be expressed using conservation of momentum, assuming axial velocity stays constant from the leading to trailing edge. Equation 1-66 below shows Y expressed using conservation of momentum, in terms of mass flow rate per blade $\Delta\dot{m}$ and the change in relative tangential velocities from trailing edge to leading edge, shown below in equation 1-66 [27]:

$$Y = \Delta\dot{m}(W_{u2} - W_{u1}) \tag{1-66}$$

The ideal tangential force per blade Y_{id} is determined using an idealized pressure distribution from leading to trailing edge across a blade, multiplied by the area on which it acts. Zweifel defined this idealized pressure distribution using the assumption that the total pressure at the leading edge P_{t1} acts over the entire pressure side of the blade, meaning that velocity is assumed to be zero [14]. For this idealized pressure difference used for derivation of the Zweifel coefficient, it is assumed that the pressure is equal to P_2 on the entire suction side of the blade, and it is assumed the pressure is constant across the surface with no diffusion. The pressure distribution across the blade is thus assumed to be a rectangular shape [14]. Y_{id} is calculated by multiplying this pressure difference by the surface area on which this force acts, the product of the axial blade length and the blade height, bh_b, applied below in equation 1-67.

$$Y_{id} = (P_{t1} - P_2)bh_b \tag{1-67}$$

Figure 1.23 below shows an example pressure distribution across a blade with idealized pressure distribution for calculation of Zweifel coefficient. The Zweifel coefficient is a measure of how close the area of the real pressure distribution on the blades is to the area of this idealized pressure distribution.

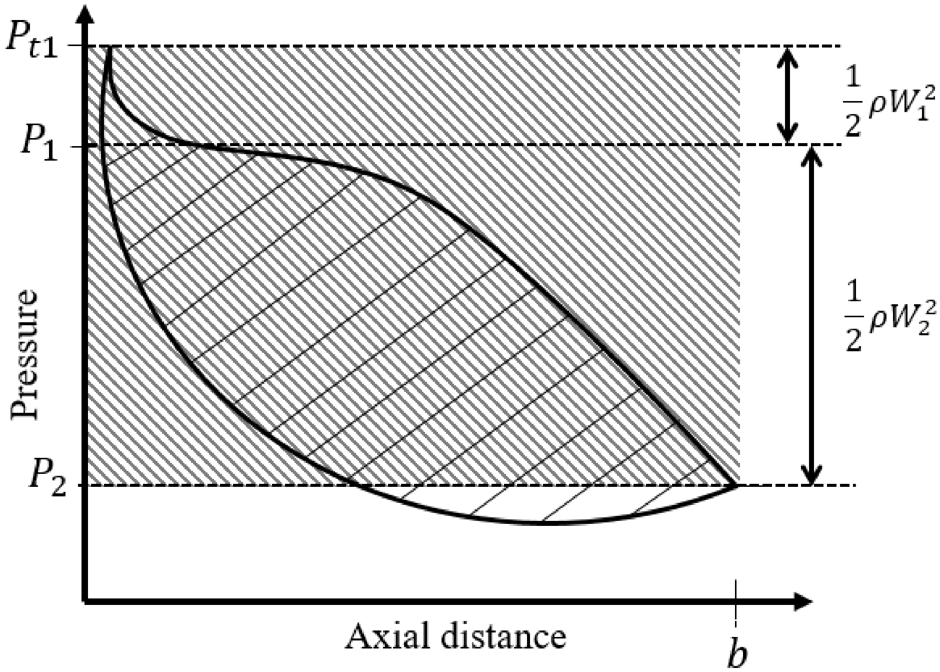

Figure 1.23. Idealized pressure distribution with actual pressure distribution for Zweifel coefficient calculation

For incompressible flow the idealized pressure difference $P_{t1} - P_2$ is equal to the dynamic pressure at the trailing edge, $\frac{\rho W_2^2}{2}$ [14]. Plugging into equation 1-67, the expression for idealized tangential force is seen below in equation 1-68:

$$Y_{id} = \frac{bh_b\rho W_2^2}{2} \tag{1-68}$$

It is assumed that meridional velocity W_m stays constant from leading edge to trailing edge, thus $W_{m1} = W_{m2}$. By plugging in the definition of the mass flow rate through one blade path, $\Delta\dot{m}$, equation 1-44, into the definition the actual tangential blade force Y (equation 1-66), Y can then be calculated, below in equation 1-69.

$$Y = \rho h_b s W_m (W_{u2} - W_{u1}) \tag{1-69}$$

Equations 1-68 and 1-69 can be plugged into the definition of Z (equation 1-65). Using the definition of relative flow velocity $\vec{W}$ (equation 1-16), the definition of Z can be rearranged to be expressed in terms of relative flow angles, seen below in equation 1-70 [27]:

$$Z = \frac{Y}{Y_{id}} = \frac{\Delta\dot{m}(W_{u2} - W_{u1})}{(P_{t1} - P_2)bh_b} = \frac{W_{m2}s(W_{u2} - W_{u1})}{\frac{1}{2}W_2^2 b} \tag{1-70}$$

The Zweifel coefficient is proportional to the ratio of the blade spacing to the axial blade length, $\frac{s}{b}$. Zweifel coefficient is similar to the tangential force coefficient C_y, originally defined in equation 1-51, simplified in equation 1-71 below. Unlike Z, C_y is not dependent upon $\frac{s}{b}$, and C_y uses mean relative velocity to normalize the tangential force. A set of designs with the same relative flow velocity components can have different values of Z depending on blade spacing and axial blade length, however the value of C_y will stay constant across each design.

$$C_y = \frac{Y}{\frac{1}{2}\rho W_{mean}^2 s h_b} = \frac{W_{m2}(W_{u2} - W_{u1})}{\frac{1}{2}W_{mean}^2} \tag{1-71}$$

The Zweifel coefficient recommendations from literature can be used to find the recommended value of $\frac{s}{b}$. After calculating the ideal $\frac{s}{b}$, the ideal b can then be calculated using a known value of s. Equation 1-70 is rearranged to solve for $\frac{s}{b}$ in equation 1-72 below:

$$\frac{s}{b} = .\frac{ZW_2^2}{2W_{m2}(W_{u2} - W_{u1})} \tag{1-72}$$

The Zweifel coefficient depends on the number of blades, axial blade length, blade spacing, and the blade angles, which are all interconnected. Blades which are closer together have lower Z, and results in higher weight, increased cost, reduced blade loading per blade, and increased friction losses due to increased surface area. Blades which are farther apart have higher Z, lower cost, lower weight, more tangential force distributed per blade, but lower friction losses, due to the decreased blade surface area [22].

Farther apart blades, therefore higher loading per blade can increase losses resulting from diffusion and adverse pressure gradients, while offering the benefit of lower friction. As

Zweifel coefficient is raised further the risk of flow separation increases [28] [4] [23]. Literature suggests that for the designs with higher Zweifel coefficient, losses via friction from the blade surfaces, hub and shroud are reduced, however the losses resulting from diffusion and trailing edge losses are higher [24] [28].

1.14.1. Recommended Values of Zweifel Coefficient

Zweifel suggested that for turbine cascades with incompressible flow at low Mach numbers, minimum profile losses occur and maximum efficiency can be reached when $Z = .8$ [26]. However since Zweifel's original paper, additional work has been done to determine optimal values of Z, after Zweifels initial work Pfiel demonstrated the optimal value of the coefficient varies from $Z = .75$ to 1.15 depending on flow deflection [30]. The experimental data used to determine the optimal value of Zweifel coefficient is based on dated turbine blade profiles, with moderate loading [4].

E.Dick noted the recommended value of the Zweifel coefficient does not change depending on the Mach number, and works for both incompressible and compressible fluids. He mentions that the optimal value of Zweifel coefficient is between 1.0 and 1.2, with separation beginning with values between 1.4 and 1.6 [27]. Although there is no agreement on a Zweifel coefficient that results in the highest efficiency, the literature suggests that for a given turbine design, the peak efficiency will be measured at a Zweifel coefficient somewhere between .75 and 1.2.

1.14.2. Industry Trend - Higher Zweifel Coefficients

A major trend in the turbine industry is the design of blades with ever increasing Zweifel coefficients, usually achieved by decreasing the number of blades. The desire to use turbine designs with higher Zweifel coefficients is primarily motivated by the desire to decrease total cost of ownership of turbine equipment. Blade profile design with high Zweifel coefficients is an area of active research, motivated primarily by the need to reduce part count and engine weight in commercial gas turbines, especially jet engines. [31] Reducing part count reduces capital cost, and service cost, reducing total cost of ownership. Decreasing the number of blades increases the tangential force Y imparted per blade, this increases Zweifel coefficient. The definition of the blade spacing, equation 1-33, and equation 1-72 show that reducing the number of blades increases blade spacing s, in turn increasing Zweifel coefficient. Reducing the number of blades reduces the number of parts and lowers material costs, which in turn reduces manufacturing and maintenance costs [31]. This is considered important, especially in the aviation industry where engine weight is critical.

Zweifel coefficient can also be increased by reducing the axial length of the blades, b. Reducing the axial blade length has a similar effect on the tangential loading to reducing the number of blades, this is because Zweifel coefficient is a measure of the tangential loading experienced per blade, weighed against the axial length. Reducing axial blade length is advantageous from a cost perspective as well, as blades with lower axial length require less material, cost less to manufacture, and weigh less.

Tests involving the highest Zweifel coefficient blade profiles demonstrated (in a cascade) were conducted by Praisner et. al, who tested airfoils with Zweifel coefficients between 1.6 and 1.82 [32]. However there has been less success in demonstrating airfoils with very high Zweifel coefficients in actual commercial gas turbines [28]. Schmitz et. al. developed a turbine stage called the Notre Dame Highly Loaded Turbine 01 (ND-HiLT01), with a rotor Zweifel coefficient of 1.35, with a blade loading coefficient of 2.8, and measured a stage efficiency of 90.6% [31]. The ND-HiLT01 was developed to demonstrate a reduction in stage count for a gas turbine engine and the part count of an individual airfoil row.

1.14.3. Zweifel Analysis

Reducing the number of blades and reducing the axial blade length both increase Zweifel coefficient for a design. The below Figure 1.24 shows how changing axial blade length b affects Zweifel coefficient, for a turbine with same power and flow rate as the first simulation case in this work. The designs in the Blade Length Study in this work had their Zweifel coefficients adjusted in this way by changing b.

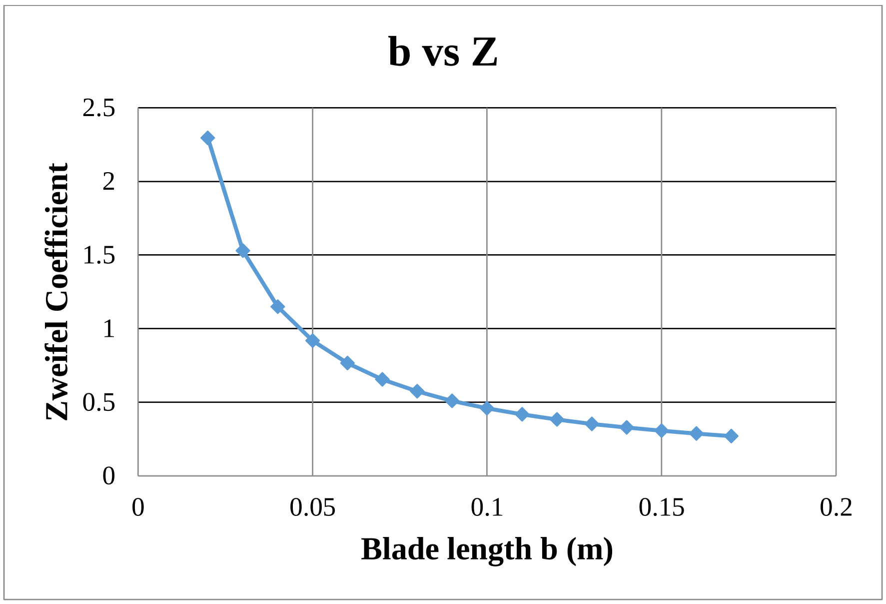

Figure 1.24. Blade length vs. Zweifel coefficient

Zweifel coefficient can also be changed by changing the number of blades of the design, which effects the blade spacing s. Reducing the number of blades increases the tangential force Y which is distributed per blade, thus increasing Z. The below Figure 1.25 shows this effect for a turbine design.

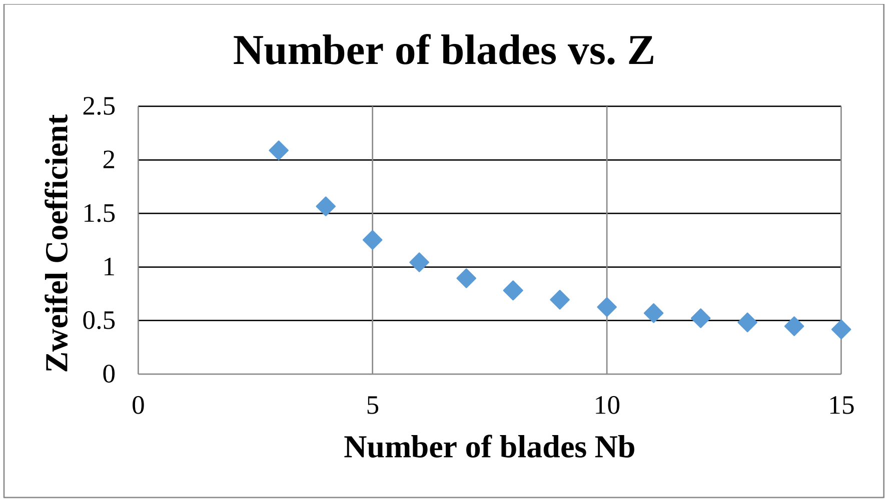

Figure 1.25. Number of blades vs. Zweifel coefficient

Zweifel coefficient can be changed while keeping relative flow angles, mass flow rate, and power constant by changing the number of blades or the blade length. Zweifel coefficient can be changed by changing the tip speed U, however the relative flow angles will change. The tip speed U has a significant effect on Zweifel coefficient, designs with larger tip speeds have lower Zweifel coefficients. The below Figure 1.26 shows how changing U effects Z for different turbine designs with the same power output, with three different blade lengths.

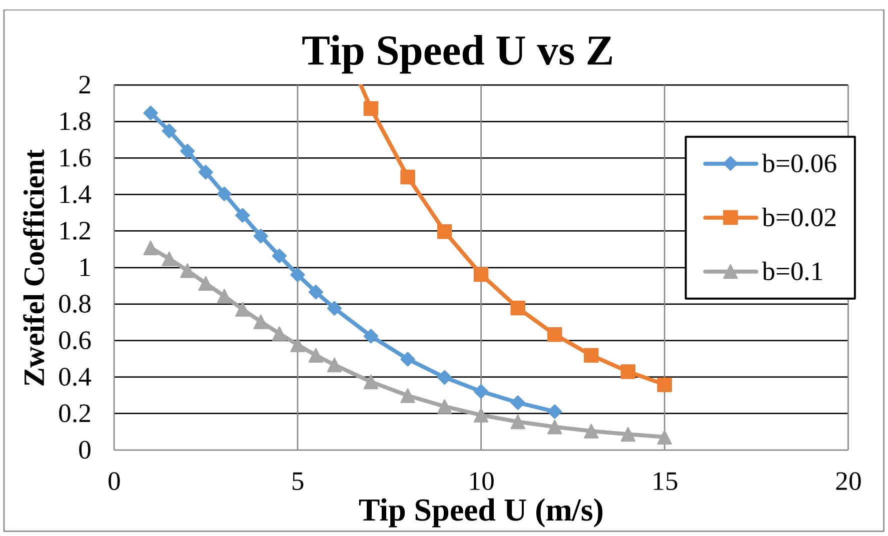

Figure 1.26. Tip speed vs. Zweifel coefficient at differing blade lengths

The above figure illustrates that designs with high tip speeds have low values of Zweifel coefficient. As tip speed is increased for a given design, to keep Zweifel coefficient near typical levels between ..75 and 1.2, blade length has to be decreased. This was demonstrated in the simulations done in the Speed Study, in particular the designs with the tip speed recommended by the Cordier diagram.

1.15. Cavitation

Cavitation occurs when the static pressure of the flow drops below the vapor pressure. Vapor bubbles are created by this effect, and these bubbles can collapse suddenly if the pressure rises later in the fluid stream. These collapsing bubbles can severely damage water turbines blades if the bubble collapse occurs on the turbine blade. The collapsing bubbles produce shock waves and microjets which produce high pressures and temperatures in a short period of time. Over time this effect causes fatigue in the blade material causing erosion [33]. Erosion resulting from cavitation occurs in pumps, water turbines, propellers, and valves. Cavitation is often generated on the suction surface of hydraulic turbine blades.

1.15.1. Cavitation for Composites

Composites are considered an attractive material choice for turbine blades, as the high specific strength and stiffness of these materials are superior to that of metal blades [34]. The cost of composite materials is also becoming cheaper, leading turbomachinery manufacturers to move to composite blades in many applications. The Woven Wheel technology, which is constructed out of continuous composite fiber, could be employed in a hydraulic turbine application using a CTPAT setup, is useful to investigate literature to see how composites can perform under cavitation conditions.

Studies by Yamatogi et al. investigated the cavitation resistance of composite propellers and the mechanism by which composite impellers are damaged by cavitation. Samples of three types of composites using reinforced fibers were tested under cavitation conditions, carbon fiber, glass fiber, and aramid fibers. Specimens made of epoxy resin and aluminum bronze molded NAB (CAC703) were also tested. The study demonstrated the aramid fiber reinforced composite materials exhibited less erosion than carbon or glass fibers under cavitation. It was found the resistance to cavitation erosion was superior in situations where the adhesion between fiber and resin was stronger [34].

A study by M. Ćosić, M. Dojčinović & Z. Aćimović-Pavlović measured the cavitation resistance of aluminum matrix composite with silicon carbide reinforcement particles, and found the mass loss as the result of cavitation erosion was close to the mass lost for the same test performed for CA6NM stainless steel (a 13Cr–4Ni soft martensitic stainless steel). CA6NM is known for good corrosion and cavitation resistance, and is commonly used in hydraulic machinery [33]. These studies suggest that most composite blades are more susceptible to corrosion via cavitation than metal, and careful choice of fiber and resin is required to use composites for hydro propellers.

1.16. Discussion of Loss Mechanisms

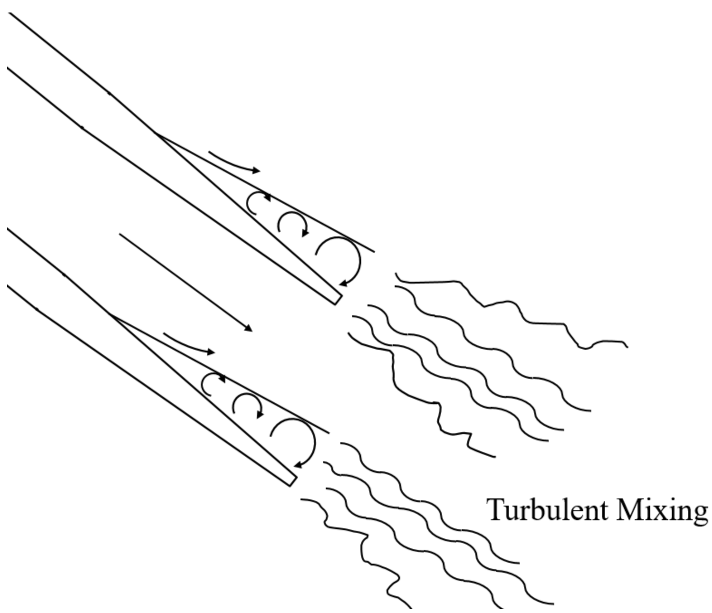

Figure 1.27. Trailing edge of blade with separated boundary layer [32]

Denton described the mechanisms surrounding viscous friction and entropy production in turbomachines [35]. Viscous friction is the result of viscous shear, which can occur in either boundary layers or mixing processes. A large portion of entropy generation in turbomachines is due to viscous shear, when the fluid undergoes a rate of shear strain. Velocity gradients which cause viscous shear are experienced at the boundary layers, the leading and trailing edges, and anywhere where flow separation is seen. Viscous shear stress is defined below in equation 1-73, where u is the local flow velocity, τ is the local shear stress, and y is position along a boundary layer [35]:

$$\tau(y) = \frac{\mu \partial u}{\partial y} \tag{1-73}$$

The rate of entropy generation per unit surface volume in a boundary layer is shown below in equation 1-74, where T is the local temperature [35]:

$$\dot{S} = \frac{1}{T} \tau \frac{du}{dy} \tag{1-74}$$

Entropy production in the boundary layer is proportional to the velocity cubed. This is why the entropy is generated more rapidly on the suction side of turbine blades than on the pressure side, where velocity is higher. Most boundary layers have velocity changing the most rapidly in the inner part of the boundary layer, especially for turbulent flow, the inner layer is where most entropy is generated within a boundary layer [32].

The wake left by the trailing edge of a turbine blade is considered a major source of losses. When two fluid streams at different velocity, pressure, or temperature mix together, entropy is generated. High shearing rates occur in wakes left after the trailing edge. Figure 1.27 above shows an example turbine blade trailing edge with separated boundary layer. Denton estimated the loss that can be attributed to the trailing edge can be estimated to be about 32% of the boundary layer losses or 21% of the total losses in a subsonic turbine blade row. Thicker blades are correlated with additional losses at the trailing edge [35].

Due to the adverse pressure gradient arising from flow diffusion on the suction surface downstream of the minimum pressure, boundary layer separation near the trailing edge can occur, and is considered a major source of blade profile losses [35]. As flow moves from leading to trailing edge along the suction side and decelerates, the adverse pressure gradient can lead to backflow in the boundary layer. Flow separation can occur when there is backflow in the boundary layer, where local change velocity along the boundary layer $\frac{du}{dy}$ becomes negative. This can lead to a distinct wake region, and for blades with high Zweifel coefficient, flow separation is of added concern [29]. With higher Zweifel coefficients, pressure on the suction side is reduced and pressure on the pressure side is increased, the resulting increased difference in velocity from the suction side to the pressure side can lead to additional shear stress, entropy generation, and losses at the trailing edge. Turbine designs with higher Zweifel coefficients have a higher degree of flow deceleration on the suction side of the blades downstream the point of minimum pressure [24]. Another major source of loss is referred to as "secondary loss", and includes friction losses resulting from the hub and shroud surfaces, as well as losses resulting from secondary flows near the hub and shroud [35]. Denton estimated that for turbines, the secondary losses are considered a major source of loss, contributing typically 1/3 of the overall loss [35].

1.17. Goals of This Thesis and Description of Work

This work explores the viability of using the CTPAT turbine design scheme for low-head hydroelectric applications, at speeds inside and outside of the recommendations of the Cordier line. This work also aims to evaluate the applicability of the literature recommendations of the value of Zweifel coefficient for these types of machines, and to see how varying Zweifel coefficient by varying blade length effects performance.

Operating with highest Zweifel coefficients requires careful design of the blade profile, as turbines with higher Zweifel loading coefficient are correlated with adverse pressure gradients on the suction side of the blades, and have an added risk of separation. In this work, the performance of the constant thickness blades in an axial turbine of the CTPAT type under varying Zweifel coefficients are tested using CFD. In the gas turbine industry, blade profiles are carefully designed using CFD in an effort to maximize performance at higher Zweifel coefficients. However detailed design of blade profiles can be computationally expensive and detailed precise blade profiles can be more expensive to machine. This work approaches this problem from a different perspective, using a simple blade profile and observing how it performs under differing conditions in simulation, with differing specific speeds and Zweifel coefficients.

The first hypothesis tested is that designs of the type simulated with specific speed recommended by the Cordier line will perform with lower efficiency than designs with specific speed lower than that recommended by the Cordier line. This work investigated whether designs below the Cordier line (lower than recommended specific speed) perform with lower efficiency than designs of similar geometry, on the Cordier line. The second hypothesis tested is that peak efficiency will be obtained in CFD for designs with Zweifel coefficients in the range between 0.75 and 1.2, and decreased efficiency will be experienced at Zweifel coefficients above and below that range.

To evaluate the applicability of the CTPAT design scheme to a low head hydro application and to evaluate these hypotheses, turbine designs were generated which defined the inputs and geometry for the CFD simulations. Losses resulting from a penstock pipe for a hydroelectric dam retrofit application were estimated to estimate the total inlet pressure. Six sets of turbine specifications were investigated in CFD. First for the "Speed Study", designs at each set of specifications at different rotational speeds were developed to test the performance of designs inside and outside of the Cordier recommendations. The highest efficiency designs from each case in the Speed Study were then simulated in the "Blade Length Study", with varying axial blade lengths to investigate the effect of varying Zweifel coefficient on performance. The effect of varying specific speed and Zweifel coefficient on efficiency, trailing edge losses, friction losses from the blades and hub and shroud surfaces, flow deviation, and cavitation are investigated. Constraints were imposed on the geometry to ensure the designs fit the geometric and manufacturing constraints of the CTPAT design scheme and the Woven Wheel manufacturing process. The analytical model was set up to obtain CFD boundary conditions which were applicable for a proposed application of a CTPAT turbine for use as a retrofit unit to fit in front of dam spillways. Chapter 2 focuses on the analysis setup, the results of the CFD simulations are discussed in Chapter 3.

CHAPTER 2. ANALYSIS DESCRIPTION AND METHODS

2.1. Description of Setup

An example application of a CTPAT turbine in a hydroelectric application is for hydroelectric dam retrofits, discussed in Chapter 1 of this work. The analytical model was set up to obtain CFD boundary conditions which were applicable for a proposed application of a CTPAT turbine for use as a retrofit turbine unit to fit on the front of dam spillways. Figure 2.1 below shows a simplified schematic of the setup.

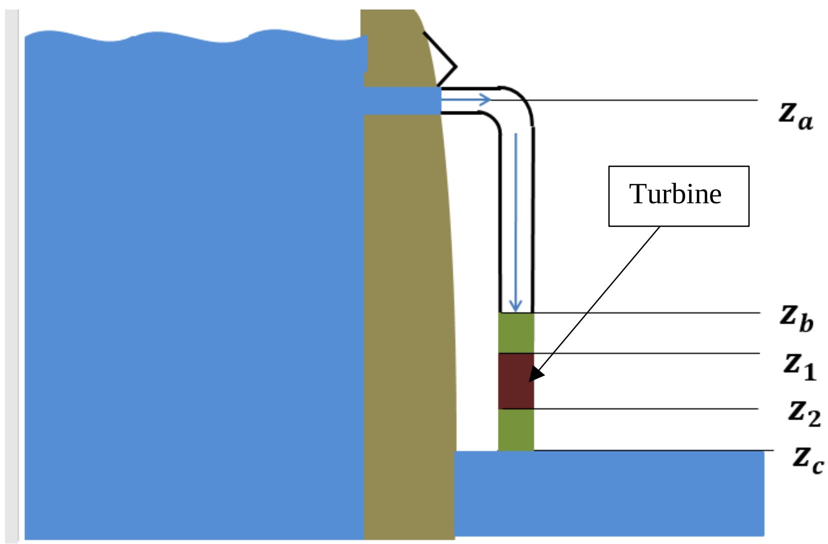

Figure 2.1. Hydroelectric dam retrofit schematic with height positions

The heights defined by z_a, z_b, z_1, z_2, z_c are input for this analysis. Each position is defined below.

- Position a: water surface/inlet of penstock pipe
- Position b: outlet of penstock pipe/inlet of turbine entry annulus
- Position 1: Turbine leading edge/outlet of turbine entry annulus
- Position 2: Turbine trailing edge /inlet of turbine exit annulus
- Position c: Outlet of turbine exit annulus, water level

2.2. Analysis Description, Description of Specifications

An analytical model was constructed in Microsoft Excel to define the inputs and boundary conditions needed for the CFD analysis. To simulate the designs in CFD, the below inputs are required. The purpose of the analytical model was to obtain these inputs.

- Total pressure at inlet of the turbine entry annulus, P_{tb}, accounting for estimated friction losses in penstock pipe
- Mass flow rate $\dot{m}$
- Tip speed of rotor $U_1 = U_2$
- Relative blade angles at leading and trailing edges, β_{b1} and β_{b2} respectively
- Density of water ρ
- Geometry:
    - Inside and outside radius of turbine rotor r_h, r_s respectively, equal to radii of entry and exit annuli
    - Blade thickness t
    - Number of blades N_b

This model takes turbine and penstock geometry, head, and flow rates as inputs and calculates values of absolute and relative flow speeds/angles, estimated total pressure at the turbine entry annulus, as well as blade angles for CFD analysis. The analytical model was made to take account for losses in a penstock pipe, including friction resulting from the pipe surfaces, and the friction loss associated with a 90 degree turn of the penstock. Six different sets of specifications relevant to low-head hydro applications were investigated. Three size turbines were considered, at two different values of total available head, H. Each of the six sets of specifications had its own input volume flow rate. Designs at each set of specifications, referred to as a “case”, were generated at differing rotational speeds for the Speed Study. After finding the RPM where efficiency was measured highest through CFD, a new set of designs were generated for each case, each with a different axial blade length and corresponding Zweifel coefficient. This second set of designs were simulated during the Blade Length Study.

- Case 1: $H = 2m$, .2 m OD, .12m ID, $\dot{V} = .46\,\frac{m^3}{s}$
- Case 2: $H = 2m$, .3 m OD, .18 m ID, $\dot{V} = 1.05\,\frac{m^3}{s}$
- Case 3: $H = 2m$, .5 m OD, .3 m ID, $\dot{V} = 2.85\,\frac{m^3}{s}$
- Case 4: $H = 4m$, .2 m OD, .12m ID, $\dot{V} = .6\,\frac{m^3}{s}$
- Case 5: $H = 4m$, .3 m OD, .18 m ID, $\dot{V} = 1.5\,\frac{m^3}{s}$
- Case 6: $H = 4m$, .5 m OD, .3 m ID, $\dot{V} = 4.1\,\frac{m^3}{s}$

The surface roughness of 314 stainless steel was used for the penstock pipe friction calculations. The temperature of the water flow was assumed to be 20 degrees Celsius for the calculations. This temperature was needed to find the kinematic viscosity and vapor pressure of the water flow. The analysis and CFD simulations did not include a draft tube, an important and necessary part of a turbine installation which can be used to decelerate the flow. For use in a real application a draft tube will need to be included as a part of the design.

2.3. Estimation of Friction Losses

The purpose of this section is to demonstrate how the inputs for CFD described above were determined for the designs later simulated in CFD. For this analysis, Bernoulli’s equation was used to estimate the total work extraction from the fluid, e, which was needed to define the relative and absolute flow angles needed to generated designs for CFD analysis, as well as the total pressure at the inlet of the entry annulus, P_{tb}. Bernoulli’s equation is a modified version of the energy conservation equation, and is defined below in equation 2-1, Where P is static gage pressure, C is absolute flow speed, z is vertical distance from the datum, water level, g is the gravitational acceleration constant, F_f is the friction work done per unit mass of a fluid element while moving from positions i and j along a streamline in the direction of flow, and e represents total mass-specific energy extraction from positions i to j [4]:

$$\frac{P_i}{\rho} + \frac{C_i^2}{2} + gz_i = \frac{P_j}{\rho} + \frac{C_j^2}{2} + gz_j + F_f + e \tag{2-1}$$

For the analysis in this work, e was estimated by carrying out Bernoulli's equation between each system position, a through c, then combining the equations to obtain an expression for e. This begins with points a and b, from the water surface to the outlet of the penstock pipe, shown below in equation 2-2.:

$$\frac{P_a}{\rho} + \frac{C_a^2}{2} + gz_a = \frac{P_b}{\rho} + \frac{C_b^2}{2} + gz_b + F_{fab} \tag{2-2}$$

For this analysis it is assumed that the velocity at the water surface is zero, and the gage static pressure at the water surface is zero. Thus $C_a, P_a = 0$. It is also assumed that the motion of the water at the outlet of the penstock pipe is purely axial in direction. The velocity of the water at the outlet of the penstock pipe can be calculated using equation 2-3 below, using the continuity equation.

$$C_b = \frac{\dot{m}}{\rho A_{ma}} \tag{2-3}$$

Mass-specific friction loss from positions a to b F_{fab} is calculated using the friction loss equation for flow in a pipe added to the friction loss equation due to a 90 degree bend, where ξ_p is the friction loss coefficient for the penstock pipe, and K is the friction loss coefficient resulting from the 90 degree turn, shown below in equation 2-4:

$$F_{fab} = \frac{\xi_p C_b^2}{2} + \frac{K C_b^2}{2} \tag{2-4}$$

ξ_p is found using the below equation 2-5, a re-ordered version of the Darcy-Weisbach equation, where L_t is the length of the penstock pipe, f_{ab} is the friction factor for the penstock pipe, and r_b is the radius of the penstock pipe [36]:

$$\xi_p = \frac{f_{ab} L_t}{2 r_b g} \tag{2-5}$$

There are many equations which can be used to estimate this friction factor for a full-flowing circular pipe, for this analysis the Haaland equation is used, valid for turbulent flow. The accuracy of the friction factor calculated using this equation is within $\pm 2\%$ for Reynolds numbers above 3000 [36]. First Re_b is calculated using equation 2-6 below, the Reynolds number at position b, where μ is the kinematic viscosity of water [4]:

$$Re_b = \frac{C_b r_b}{\mu} \tag{2-6}$$

Then the Haaland equation is applied below in equation 2-7, ε_r is the surface roughness [36].

$$f_{ab} = \frac{1}{\left(-1.8 \log\left(\frac{6.9}{Re_b} + \left(\frac{\frac{\varepsilon_r}{2r_b}}{3.7}\right)^{1.11}\right)\right)^2} \tag{2-7}$$

The penstock pipe modeled as a part of this analysis turns 90 degrees, before the flow reaches the turbine leading edge. The losses resulting from turning the flow 90 degrees were predicted. The friction loss coefficient resulting from the 90 degree turn, K, is predicted using correlations from literature, specifically a chart for predicting K for 90 degree bends of uniform diameter obtained from the Hydraulic Institute's Pipe Friction Manual [37]. After obtaining the predicted friction factors, Equation 2-4 was then simplified and re-arranged to form equation 2-8 below:

$$\frac{P_b}{\rho} = g(z_a - z_b) - \frac{C_b^2}{2}\left(1 + \xi_p + K\right) \tag{2-8}$$

Then Bernoulli's equation for positions b to 1 (from the inlet of the entry annulus to the leading edge of the turbine) is applied in equation 2-9 below.

$$\frac{P_b}{\rho} + \frac{C_b^2}{2} + gz_b = \frac{P_1}{\rho} + \frac{C_1^2}{2} + gz_1 + F_{fb1} \tag{2-9}$$

The region between the inlet of the entry annulus to the leading edge of the turbine are simulated as a part of the CFD analysis. As such the friction loss from positions b to 1, F_{fb1}, is accounted for in the CFD simulation. The expression for $\frac{P_b}{\rho}$ (equation 2-8) is then plugged into equation 2-9 to obtain equation 2-10 below:

$$g(z_a - z_b) - \frac{C_b^2}{2}\left(1 + \xi_p + K\right) + \frac{C_b^2}{2} + g(z_b - z_1) = \frac{P_1}{\rho} + \frac{C_1^2}{2} \tag{2-10}$$

Equation 2-10 is then simplified to obtain equation 2-11 below:

$$g(z_a - z_1) - \frac{\xi_p C_b^2}{2} - \frac{K C_b^2}{2} = \frac{P_1}{\rho} + \frac{C_1^2}{2} \tag{2-11}$$

Rearranging equation 2-11 to solve for $\frac{P_1}{\rho}$, equation 2-12 is formed:

$$\frac{P_1}{\rho} = g(z_a - z_1) - \frac{\xi_p C_b^2}{2} - \frac{K C_b^2}{2} - \frac{C_1^2}{2} \tag{2-12}$$

Bernoulli's equation is then applied for positions 1 to 2 (turbine leading edge to trailing edge) in equation 2-13 below. The total work extracted from the fluid by the turbine is e.

$$\frac{P_1}{\rho} + \frac{C_c^2}{2} + gz_1 = \frac{C_2^2}{2} + \frac{P_2}{\rho} + gz_2 - e \tag{2-13}$$

Plugging equation 2-12 into equation 2-13 and rearranging, equation 2-14 below is formed,

$$g(z_a - z_1) - \frac{\xi_p C_b^2}{2} - \frac{K C_b^2}{2} = \frac{C_2^2}{2} + \frac{P_2}{\rho} + g(z_2 - z_1) + e \tag{2-14}$$

Bernoulli's equation is then applied for positions 2 to c, from the turbine trailing edge to the outlet of the exit annulus, seen below in equation 2-15.

$$\frac{P_2}{\rho}+\frac{C_2^2}{2}+gz_2=\frac{P_c}{\rho}+\frac{C_c^2}{2}+gz_c+F_{f2c} \tag{2-15}$$

The region between the trailing edge of the turbine to the outlet of the exit annulus are simulated as a part of the CFD analysis. The friction loss from positions 2 to c, F_{fde}, is accounted for in the CFD simulations. As position c is located at the datum, water level, $P_c = 0$. Rearranging equation 2-15 and simplifying, equation 2-16 below is formed:

$$\frac{P_2}{\rho}=\frac{C_c^2}{2}+g(z_c-z_2)-\frac{C_2^2}{2} \tag{2-16}$$

Plugging equation 2-16 into equation 2-14 and solving for e gives equation 2-17 below:

$$e=-\frac{C_c^2}{2}+g(z_a-z_c)-\frac{\xi_p C_b^2}{2}-\frac{KC_b^2}{2} \tag{2-17}$$

With mass flow rate and geometry as inputs, absolute meridional flow speed at the leading edge C_{m1} can be calculated using the continuity equation, applied below in equation 2-18:

$$C_{m1}=\frac{\dot{m}}{A_m\rho} \tag{2-18}$$

The turbine is designed so C_m stays constant from leading to trailing edge, such that $C_{m1} = C_{m2}$. Flow angle at the leading edge α_1 is also input, allowing C_{u1} to be calculated using equation 1-19, applied below in equation 2-19:

$$C_{u1}=\frac{C_{m1}}{\tan\alpha_1} \tag{2-19}$$

Equation 2-17 is then rearranged to be expressed in terms of variables with known values. To simplify the estimation of e, C_c, the velocity of the flow at the outlet of the exit annulus, is assumed to be equal to C_2, the velocity at the trailing edge. C_2 is then expressed in terms of the mass-specific turbine shaft work $\tilde{e}$, by first expressing C_2 in terms of its meridional and tangential velocity components, seen below in equation 2-20:

$$C_2^2 = C_{m2}^2 + C_{u2}^2 \tag{2-20}$$

Euler's equation of turbomachinery, expressed in equation 1-40, is then applied between positions 1 and 2 (leading edge to trailing edge of turbine rotor), and then solved for C_{u2}, shown below in equation 2-21:

$$C_{u2} = \frac{\tilde{e} + C_{u1}\,U_1}{U_2} \tag{2-21}$$

Using $e = \frac{\tilde{e}}{\eta}$, where η is isentropic turbine efficiency, equation 2-21 is expressed in equation 2-22:

$$C_{u2} = \frac{e\eta + C_{u1}\,U_1}{U_2} \tag{2-22}$$

For the designs considered in this analysis, hub and shroud radii stayed constant from leading to trailing edge, such that $U_1 = U_2$. For this analysis it was assumed that C_m stays constant from leading to trailing edges, such that $C_{m1} = C_{m2}$. Equation 2-22 above is then plugged into equation 2-20 to express C_2 in terms of known variables, shown below in equation 2-23:

$$C_2^2 = C_{m1}^2 + \left(\frac{e\eta + C_{u1}\,U_1}{U_2}\right)^2 \tag{2-23}$$

Equation 2-23 is then plugged into equation 2-17 to express e in terms of known variables, shown below in equation 2-24:

$$e = -\frac{C_{m1}^2 + \left(\frac{e\eta + C_{u1}\,U_1}{U_2}\right)^2}{2} + g(z_a - z_c) - \frac{\xi_p C_b^2}{2} - \frac{K C_b^2}{2} \tag{2-24}$$

To determine the absolute and relative flow speeds and angles, a value of η = 100% (ideal) was assumed, which allows for preliminary calculation of relative flow angles at the trailing edge that are necessary for generating designs for CFD. The quadratic equation is used to solve equation 2-24 for e. After e was calculated, C_{u2} needed to be determined in order to obtain the relative and absolute flow angles necessary for defining the turbine blade geometry. As the efficiency of the machine is not yet known, accurate values of C_{u2}, $\tilde{e}$, and β_2 cannot yet be determined, and for this analysis are obtained via CFD simulations.

The CFD simulations require inputting blade angles, β_{b1} and β_{b2}. For an ideal turbine, $\tilde{e}$ is equal to e, and β_2 is then $\beta_{b2} = \beta_2$. However, the turbine will not perform at 100% efficiency, and the flow does not follow the blades perfectly, so the trailing edge relative flow angle β_2 was reached in CFD by specifying an trailing edge blade angle β_{b2} and adjusting it until the total mass-specific work extraction achieved through CFD was equal to e.

An initial value of β_{b2} was required as an input to conduct the first simulation, this is defined as β_{b2i}. Flow speeds and angles were calculated by first inputting an efficiency of 100% into equation 2-22 to obtain an initial, idealized value of absolute circumferential trailing edge velocity C_{u2i}. Then initial, idealized values of W_2, W_{u2}, C_2, α_2, β_1 were calculated, denoted in this work as W_{2i}, W_{u2i}, C_{2i}, α_{2i}, β_{1i}. Equations 1-18,1-31,1-17,1-19, and 1-20 were used, respectively, to calculate these initial values. Finally, equation 1-20 was used to obtain β_{b2i}, substituting β_{b2i} for β_2 in the expression. An initial value of $\beta_{b1} = \beta_{1i}$ was used for the first simulation. After conducting a first simulation with $\beta_{b2} = \beta_{b2i}$, β_{b2} was reduced iteratively until the desired value of e was reached in CFD. After obtaining the desired work extraction through CFD, $\tilde{e}$, β_2, C_{u2}, and efficiency η were logged.

The calculations to obtain the flow speeds and angles were carried out at three positions along the blade: at the hub, shroud, and 50% span. Relative flow and blade angles were calculated such that the product of the rotor tangential speed multiplied by the ideal absolute tangential flow speed $U_\theta C_{ui}$ is constant across the blade span at the trailing edge.

The total pressure at the inlet of the turbine entry annulus, P_{tb} was then calculated, this value was used as a total pressure boundary condition for the annulus inlet for the CFD simulations. To simplify the analysis the gravitational potential energy of the turbine $\rho g(z_c - z_a)$ was applied in the form of total pressure at the annulus inlet for CFD simulations P_{tb}. This is shown below in equation 2-25, where F_{fac} is the sum of the friction losses considered above per unit mass from points a to c.

$$P_{tb} = \rho g(z_a - z_c) + P_{atm} - gF_{fac} = \rho g(z_a - z_c) + P_{atm} - \rho \frac{\xi_p C_b^2}{2} - \rho \frac{K C_b^2}{2} \qquad (2\text{-}25)$$

2.4. CFD Methodology and Assumptions

2.4.1. CFD Overview

The analytical model was used to obtain the boundary conditions and inputs for computational fluid dynamics (CFD) software. The software package used was ANSYS. The CFD analysis was carried out in ANSYS CFX. Computational Fluid Dynamics (CFD) software solves modified forms of the Navier-Stokes equations, as well as continuity. The Navier-Stokes equations describe how the flow velocity, pressure, temperature, and density of a viscous fluid are related. The Navier-Stokes equations in the x, y, and z direction are listed below for incompressible flow with constant viscosity, where u represents the local velocity, equation 2-26 is in the x direction, equation 2-27 in the y direction, and equation 2-28 is in the z direction:

$$\rho(\frac{\partial u_x}{\partial t} + u_x \frac{\partial u_x}{\partial x} + u_y \frac{\partial u_x}{\partial y} + u_z \frac{\partial u_x}{\partial z}) = -\frac{\partial P}{\partial x} + \rho g_x + \mu(\frac{\partial^2 u_x}{\partial x^2} + \frac{\partial^2 u_x}{\partial y^2} + \frac{\partial^2 u_x}{\partial z^2}) \qquad (2\text{-}26)$$

$$\rho(\frac{\partial u_y}{\partial t} + u_x\frac{\partial u_y}{\partial x} + u_y\frac{\partial u_y}{\partial y} + u_z\frac{\partial u_y}{\partial z}) = -\frac{\partial P}{\partial y} + \rho g_y + \mu(\frac{\partial^2 u_y}{\partial x^2} + \frac{\partial^2 u_y}{\partial y^2} + \frac{\partial^2 u_y}{\partial z^2}) \quad (2\text{-}27)$$

$$\rho(\frac{\partial u_z}{\partial t} + u_x\frac{\partial u_z}{\partial x} + u_y\frac{\partial u_z}{\partial y} + u_z\frac{\partial u_z}{\partial z}) = -\frac{\partial P}{\partial z} + \rho g_z + \mu(\frac{\partial^2 u_z}{\partial x^2} + \frac{\partial^2 u_z}{\partial y^2} + \frac{\partial^2 u_z}{\partial z^2}) \quad (2\text{-}28)$$

The continuity equation is below in equation 2-29 for incompressible flow:

$$\frac{\partial u_x}{\partial x} + \frac{\partial u_y}{\partial y} + \frac{\partial u_z}{\partial z} = 0 \quad (2\text{-}29)$$

The four equations are all coupled. Time dependent solutions of the Navier-Sokes equations are too computationally expensive to be feasible for most situations. Reynolds-averaging is used to simplify the process of solving the equations, in a way such that small scale turbulent fluctuations do not need to be simulated. The Reynolds averaged Navier-Stokes equations are time-averaged versions of the Navier-Stokes equations. For Reynolds averaging, the velocity and scalar variables of the Navier-Stokes equations are converted into mean (time averaged) and fluctuating components, shown below in equation 2-30, where $\overline{u_j}$ are the mean velocity components (j=1,2,3) and $u_j{}'$ are the fluctuating velocity components:

$$u_j = \overline{u_j} + u_j{}' \quad (2\text{-}30)$$

Pressure and the other scalar quantities in the Navier-Stokes equations are converted into mean and fluctuating components as well. The variables in this form are substituted into the Navier-Stokes continuity and momentum equations to derive the Reynolds averaged Navier-Stokes (RANS) equations, shown below in index notation in equation 2-32, where δ_{jk} is the Kroneker delta, the definition of which is listed in equation 2-31 [36].

$$\delta_{jk} = \begin{cases} 0 \; for \; j \neq k \\ 1 \; for \; j = k \end{cases} \quad (2\text{-}31)$$

$$\frac{\partial \overline{u_j}}{\partial t} + \overline{u_k}\frac{\partial \overline{u_j}}{\partial x_k} = \frac{1}{\rho}\frac{\partial}{\partial x_k}(-\overline{P}\delta_{jk} + \mu\frac{\partial \overline{u_j}}{\partial x_k} - \rho\overline{u_j' u_k'}) \quad (2\text{-}32)$$

The last term represents the Reynolds stresses, τ'_{jk}, defined below in equation 2-33.

$$\tau'_{jk} = -\rho\overline{u'_j u'_k} \tag{2-33}$$

The nonlinearity of the Navier-Stokes equations has the result that the velocity fluctuations still appear in the RANS equations in the Reynold stress term. To obtain forms of the RANS equations which contain only the mean velocity and pressure, the Reynolds stress term needs to be modeled in terms of mean flow, removing references to the fluctuating component of the velocity. The Reynolds stresses are modeled using the Boussinesq hypothesis, which relates the Reynolds stresses to mean velocity gradients [38]. Joseph Boussinesq introduced the concept of eddy viscosity, and proposed relating the Reynolds stresses to the mean velocity gradients. μ_t is the turbulence eddy viscosity, k is the turbulence kinetic energy, defined as $k = \frac{1}{2}\overline{u'_j u'_k}$. Equation 2-34 below describes this relationship [38]:

$$\overline{u'_j u'_k} = \mu_t\left(\frac{\partial\overline{u_j}}{\partial x_k} + \frac{\partial\overline{u_k}}{\partial x_j}\right) - \frac{2}{3}(\rho k + \mu_t\frac{\partial\overline{u_j}}{\partial x_j})\delta_{jk} \tag{2-34}$$

The Boussinesq hypothesis was used for the $k-\epsilon$ and $k-\omega$ turbulence models used in the simulations. The $k-\epsilon$ and $k-\omega$ turbulence models use two additional transport equations to compute μ_t as a function of k, ω and ϵ. ϵ is the turbulence dissipation rate and ω is the specific dissipation rate. The $k-\epsilon$ turbulence model is considered most useful for free-shear flows with smaller pressure gradients. The $k-\omega$ turbulence model aims to model near-wall flow features more accurately than the $k-\epsilon$ turbulence model. For the CFD simulations conducted as a part of this work, the Shear Stress Transport (SST) RANS turbulence model was used. The SST turbulence model combines the $k-\epsilon$ and $k-\omega$ turbulence models, where $k-\omega$ is used in the inner region of the boundary layer, and $k-\epsilon$ is used in the free shear flow.

2.4.2. CFD Methodology and Assumptions

For all CFD simulations in this study, a single axial turbine stage was simulated. Each design simulated included an annulus entry and exit section, each with an axial length of 0.3 meters. The blade profiles for each CFD run was of a constant thickness with rounded leading and trailing edges. Blade designs were generated using BladeGen. Figure 2.2 below shows example turbine geometry, and Figure 2.3 below shows the example turbine geometry in Bladegen.

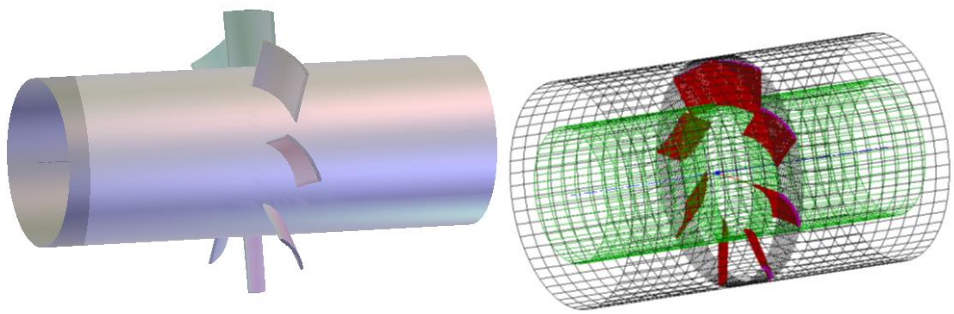

Figure 2.2. Design 1j5 generated in BladeGen

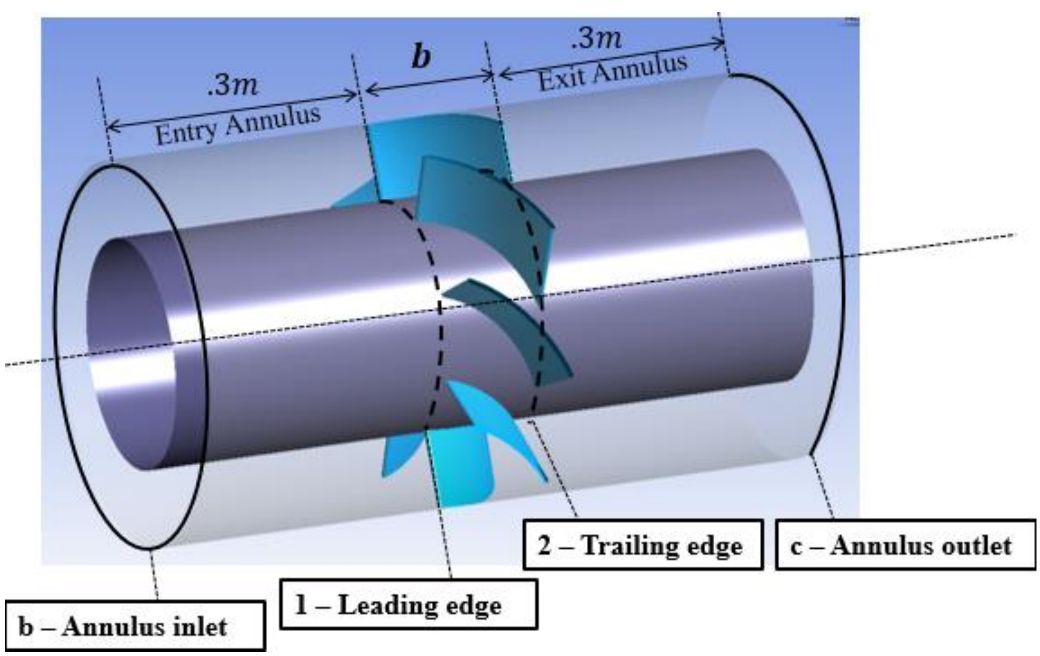

Figure 2.3. Example turbine geometry with entry and exit annuli

An outer shroud was included in the simulations, eliminating tip leakage from the simulation. Meshes were generated using ANSYS TurboGrid. All simulations were steady state, and were run until convergence was reached. To track convergence the total pressure at the annulus outlet and turbine efficiency were monitored until their values stabilized. All CFD runs were tested using the boundary condition set Total Pressure Inlet/Mass Flow Rate Outlet. Total pressure at the annulus inlet was input, taking into account the friction losses from the penstock pipe. Figure 2.2 shows renderings of one of the designs generated in BladeGen. The turbines simulated ranged in power output from 3KW to 137KW, with heads ranging from 2 to 4 meters. A number of different flow characteristics and performance metrics were measured for each CFD run. All data was recorded using CFX-Post.

For the simulations within each case, the total work extraction from the fluid (counting both shaft work and losses) was kept constant between each design. This was achieved by changing the trailing edge blade angles β_{b2}until the total pressure at the outlet of the exit annulus P_{tc} reaches the desired value, atmospheric pressure. This allows for the efficiency and performance of each turbine to be compared with each other on equal ground. Blade thickness was also kept constant within each case.

CFD simulations are not perfect recreations of a physical system, some assumptions need to be made to simplify the modeling, to reduce computation time. Gravity was not modeled in the simulations, instead the pressure as the result of gravitational force was applied to the inlet of the turbine entry annulus. The designs tested in CFD do not include an inlet guide vane. The CFD simulations assume a uniform flow velocity across the inlet which was assumed to have no pre-swirl, such that $C_{u1} = 0, \alpha_1 = 90°$. A single flow path with blade was modeled in the CFX simulations, the outputs were dependent upon an assumption of symmetry across each flow path. Only water was simulated in the blade path, cavitation was not modeled, although areas of low pressure are tracked using ANSYS CFD-POST. The simulations assumed an inlet water temperature of 20°C. The simulations did not take account for flow disturbances and turbulence resulting from the penstock pipe bend, friction losses were taken into account to obtain a total inlet pressure for CFD, as described in section 2.2. When employed in a physical application, a flow-guiding nose cone at the inlet and outlet of the annulus sections will be required, something the simulations in this work do not include. These simulations did not take surface roughness of the blades and walls into account, and assume no-slip wall conditions.

Efficiency was obtained from the CFD results, in the form of isentropic efficiency. $\dot{W}$ is the shaft power output, and was calculated in CFD by first multiplying the forces imparted on the blades in x,y, and z axis directions by the absolute flow velocities in those directions, then summing up the components and multiplying that by the number of blades. This is expressed below in equation 2-35:

$$\dot{W} = \sum_{1}^{N_b} (F_x C_x + F_y C_y + F_z C_z) \tag{2-35}$$

Isentropic efficiency was calculated in CFD-Post using the below equation 2-36, where H is the total available head.

$$\eta = \frac{\dot{W}}{\dot{V}\, Hg\rho} \tag{2-36}$$

2.5. Description and Inputs for Speed Study

In this work, each set of specifications described in section 2.2 were referred to as a “Case”. Designs were generated and simulated at least 6 different rotational speeds for each case, in addition to the rotational speed recommended by the Cordier diagram. Idealized relative flow angles at the leading and trailing edges were calculated and used to define the initial blade shape. First a value of Z = .8 was used to determine the axial blade length at each rotational speed tested. Each RPM had its own corresponding axial blade length b which was adjusted to keep Zweifel coefficient at .8.

In this analysis, preliminary geometries were first generated in the analytical model, with leading edge and trailing edge flow beta angles specified. For each rotational speed tested, new leading edge and trailing edge relative flow angles were calculated using the analytical model. For the first simulations, the leading edge blade angle β_{b2} was kept the same as the ideal flow beta angle β_{2i}. The total pressure at the annulus outlet will not reach the desired value, so for each design the trailing edge blade beta angle was reduced until the total pressure at the annulus outlet P_{tc} reached within 200 pA of the desired value, atmospheric pressure. When the total pressure at the annulus outlet reached the desired value, the data was recorded. For the Speed Study, Zweifel coefficient was kept at the original recommendation by Zweifel, Z = 0.8. This was achieved by using equation 1-72 to calculate axial blade length b, using a value of 0.8 for Z.

Each of the six cases had a rotational speed at which the highest efficiency and power output was measured. The cases at which these geometries produced the highest power/efficiency were considered for the next analysis, the Blade Length Study. A flow chart describing the CFD simulation process for the Speed Study is shown in Figure 2.4 below. The below process was repeated for all six cases.

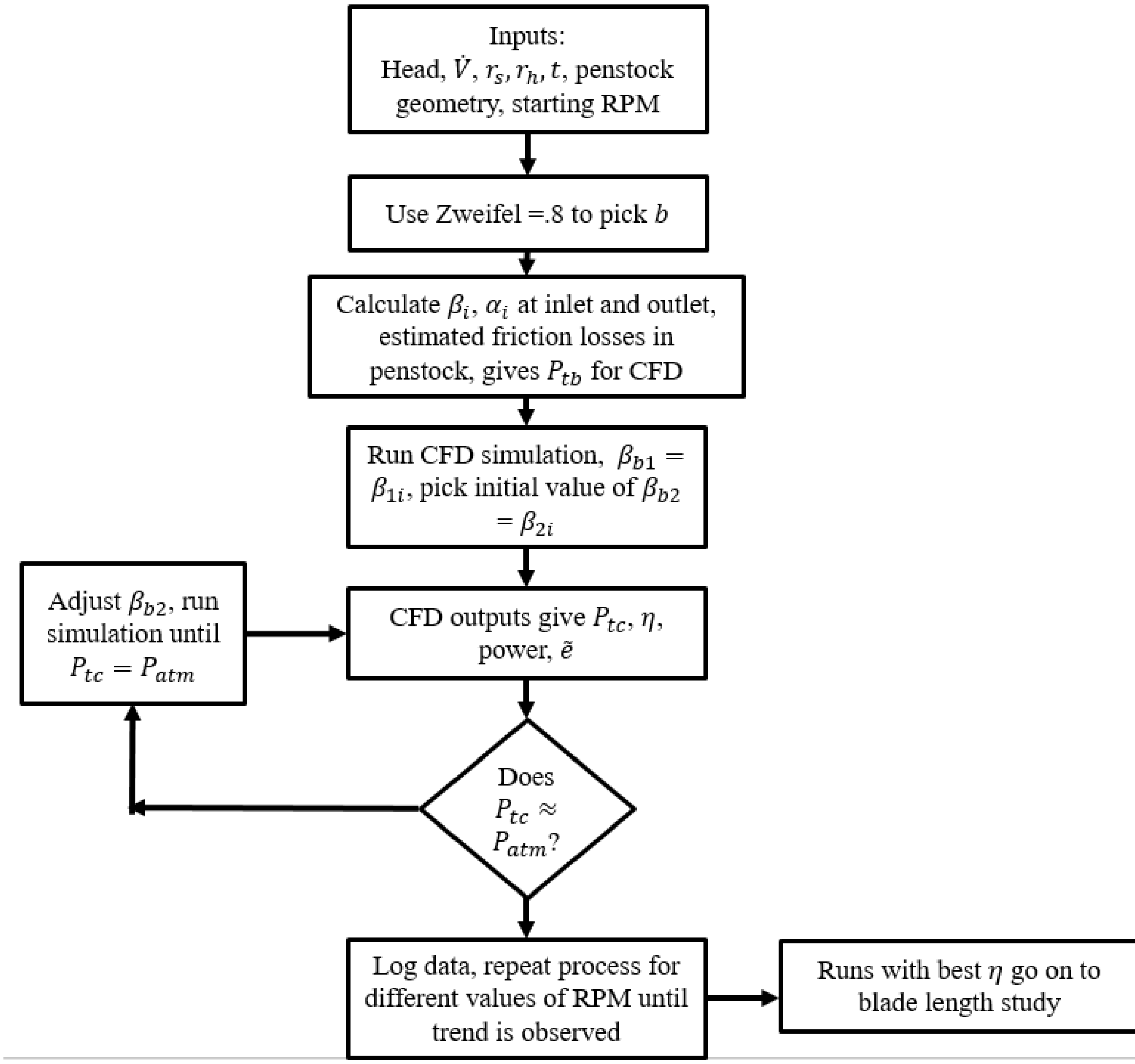

Figure 2.4. Process flow chart for Speed Study

Table 2.1 below shows the geometric parameters, idealized flow speeds, flow angles, and ideal absolute circumferential flow speed at the trailing edge C_{u2i} which was used to obtain β_{2i} for the first simulation, for two designs within Case 1 of the Speed Study, designs 1j and 1CORD. The table also shows the final values of β_{b2} that were used to obtain the results. For the simulations of each design, β_{b1} was kept equal to β_{1i}, as first simulations showed incidence $i'$was close to zero for every design simulated. Table 2.1 below shows how the higher speed designs in the Speed Study, in this case 1CORD, require a smaller axial blade length to keep Z at

.8. The designs were set up such that the product of the ideal circumferential flow speed and the circumferential rotor velocity, $U_\theta C_{ui}$ was kept constant at all positions across the blade span.

Table 2.1. Case 1 Geometric Parameters and Flow Angles

1j												
t	r_θ	U_θ	C_{u1}	C_{u2i}	$U_\theta C_{ui}$	α_{2i}	β_{1i}	β_{1b}	β_{2i}	β_{b2}	b	Z
m	m	m/s	m/s	m/s	$\frac{m^2}{s^2}$	deg	deg	deg	deg	deg	m	
0.005	0.200	3.6	0.0	-5.1	-18.0	129.9	59.1	59.1	34.6	26.8	0.098	0.8
0.005	0.160	2.8	0.0	-6.3	-18.0	136.1	64.4	64.4	33.0	25.2	0.098	0.8
0.005	0.165	2.9	0.0	-6.1	-18.0	135.3	63.8	63.8	33.3	25.5	0.098	0.8
0.005	0.120	2.1	0.0	-8.4	-18.0	144.0	70.3	70.3	29.6	21.8	0.098	0.8
1cord												
t	r_θ	U_θ	C_{u1}	C_{u2i}	$U_\theta C_{ui}$	α_{2i}	β_{1i}	β_{1b}	β_{2i}	β_{b2}	b	Z
m	m	m/s	m/s	m/s	$\frac{m^2}{s^2}$	deg	deg	deg	deg	deg	m	
0.005	0.200	15.4	0.0	-1.2	-18.1	101.0	21.1	21.1	19.7	14.4	0.022	0.8
0.005	0.160	12.3	0.0	-1.5	-18.1	103.6	25.8	25.8	23.3	18.0	0.022	0.8
0.005	0.165	12.7	0.0	-1.4	-18.1	103.2	25.1	25.1	22.8	17.5	0.022	0.8
0.005	0.120	9.3	0.0	-2.0	-18.1	107.9	32.7	32.7	28.0	22.7	0.022	0.8

Velocity triangles of the designs were produced, Figures 2.5 and 2.6 show velocity triangles at leading and trailing edges for design 1j 1Cord of the Speed Study respectively, superimposed over the blade profile design produced using BladeGen. The higher speed designs, including 1Cord, have lower relative flow angles at leading and trailing edges, this is due to the higher rotational speed of the rotor for these designs.

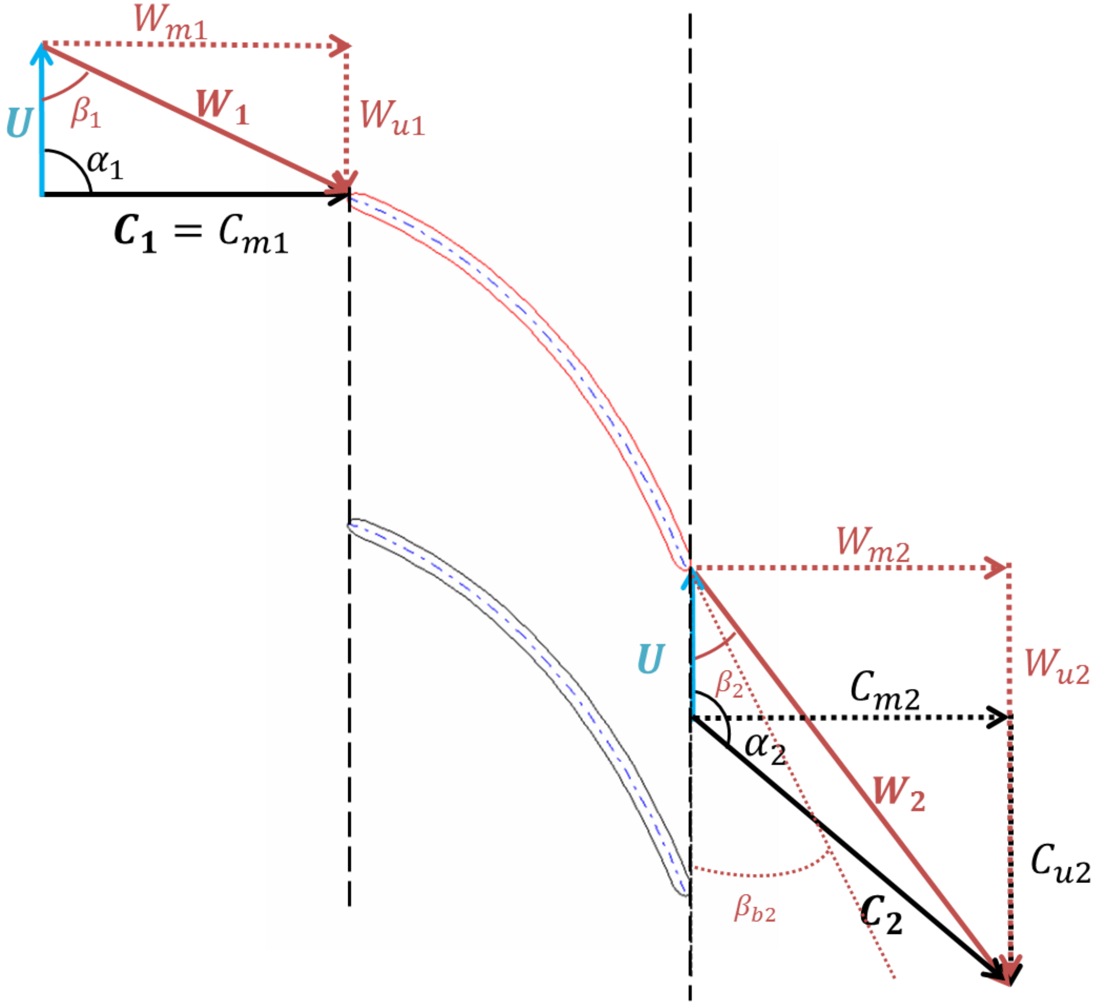

Figure 2.5. Velocity triangles for leading and trailing edges of design 1j of the Speed Study (50% span)

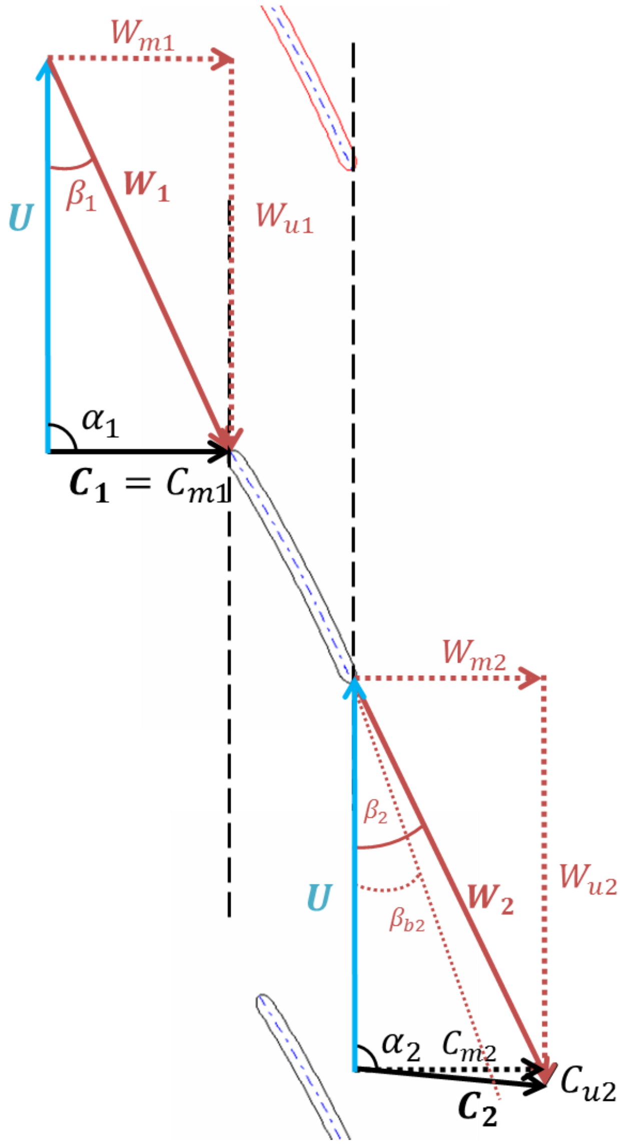

Figure 2.6. Velocity triangles for leading and trailing edges of design 1CORD of the Speed Study (50% span)

The below tables show the rotational speeds, axial blade length, and non-dimensional coefficients of the designs tested in CFD for each case for the Speed Study.

Table 2.2. Case 1 Speed Study Inputs

Case 1	Run	Total Head (m)	b (m)	RPM	ϕ	Ω_s	D_s	ψ
$\dot{V} = 0.46\,\frac{m^3}{s}$	b	1.88	0.045	350	0.79	2.80	1.22	0.34
$r_h = .12$ m	d	1.86	0.056	300	0.92	2.41	1.22	0.46
$r_s = .2$ m	f	1.86	0.070	250	1.12	2.01	1.22	0.66
	h	1.84	0.086	200	1.39	1.62	1.22	1.03
	j	1.85	0.098	170	1.63	1.37	1.22	1.43
	l	1.88	0.106	140	1.98	1.12	1.22	2.14

Table 2.3. Case 2 Speed Study Inputs

Case 2	Run	Total Head (m)	b (m)	RPM	ϕ	Ω_s	D_s	ψ
$\dot{V} = 1.050\,\frac{m^3}{s}$	b	1.90	0.031	350	0.53	4.19	1.22	0.15
$r_h = .2$ m	d	1.85	0.044	300	0.62	3.67	1.21	0.20
$r_s = .3$ m	f	1.88	0.060	250	0.75	3.01	1.21	0.30
	h	1.88	0.086	200	0.94	2.42	1.21	0.47
	j	1.88	0.105	170	1.10	2.05	1.21	0.65
	l	1.85	0.126	140	1.34	1.71	1.21	0.94
	n	1.87	0.142	120	1.56	1.45	1.21	1.29

Table 2.4. Case 3 Speed Study Inputs

Case 3	Run	Total Head (m)	b (m)	RPM	ϕ	Ω_s	D_s	ψ
$\dot{V} = 2.85\,\frac{m^3}{s}$	f	1.90	0.034	250	0.45	4.92	1.23	0.11
$r_h = .3$ m	h	1.89	0.061	200	0.56	3.96	1.23	0.17
$r_s = .5$ m	j	1.92	0.104	150	0.74	2.94	1.23	0.31
	l	1.91	0.148	120	0.93	2.36	1.23	0.47
	n	1.88	0.199	90	1.24	1.79	1.23	0.83
	p	1.88	0.260	60	1.86	1.19	1.23	1.87

Table 2.5. Case 4 Speed Study Inputs

Case 4	Run	Total Head (m)	b (m)	RPM	ϕ	Ω_s	D_s	ψ
$\dot{V} = 0.6\,\frac{m^3}{s}$	b	3.73	0.05	450	0.80	2.45	1.27	0.41
$r_h = .12$ m	d	3.72	0.06	400	0.90	2.19	1.27	0.52
$r_s = .2$ m	f	3.68	0.07	350	1.03	1.93	1.27	0.67
	h	3.70	0.08	300	1.20	1.64	1.27	0.92
	j	3.70	0.09	250	1.45	1.37	1.27	1.33
	l	3.70	0.10	220	1.64	1.21	1.27	1.71

Table 2.6. Case 5 Speed Study Inputs

Case 5	Run	Total Head (m)	b (m)	RPM	ϕ	Ω_s	D_s	ψ
$\dot{V} = 1.5\frac{m^3}{s}$	b	3.73	0.04	450	0.59	3.88	1.20	0.18
$r_h = .2$ m	d	3.67	0.05	400	0.67	3.49	1.20	0.23
$r_s = .3$ m	f	3.71	0.06	350	0.76	3.03	1.20	0.30
	h	3.70	0.08	300	0.89	2.60	1.20	0.41
	j	3.72	0.10	250	1.07	2.16	1.20	0.59
	l	3.72	0.11	220	1.21	1.90	1.20	0.76
	n	3.70	0.13	190	1.41	1.65	1.20	1.02
	p	3.72	0.15	160	1.67	1.38	1.20	1.44

Table 2.7. Case 6 Speed Study Inputs

Case 6	Run	Total Head (m)	b (m)	RPM	ϕ	Ω_s	D_s	ψ
$\dot{V} = 4.1\frac{m^3}{s}$	b	3.79	0.11	200	0.79	2.82	1.22	0.34
$r_h = .3$ m	d	3.79	0.14	170	0.93	2.39	1.22	0.47
$r_s = .5$ m	f	3.78	0.18	140	1.13	1.98	1.22	0.69
	h	3.78	0.22	110	1.43	1.55	1.22	1.12
	j	3.79	0.26	80	1.97	1.13	1.22	2.12
	l	3.75	0.08	250	0.63	3.55	1.22	0.21

2.6. Description and Inputs for Blade Length Study

The Blade Length Study was conducted to test the effect of changing Zweifel coefficient on turbine performance. For each turbine geometry and specified rotational speed, the axial blade length b was systematically changed to alter the Zweifel coefficient. Designs with both short blades (large Zweifel coefficient) and long blades (small Zweifel coefficient) were simulated. Similar to the Blade Length Study, as blade length was changed β_{b2} was changed and simulations were run until P_{tc} was within 200 Pa of P_{atm}. Figure 2.7 below is a flow chart which describes the steps required to obtain the desired data in CFD.

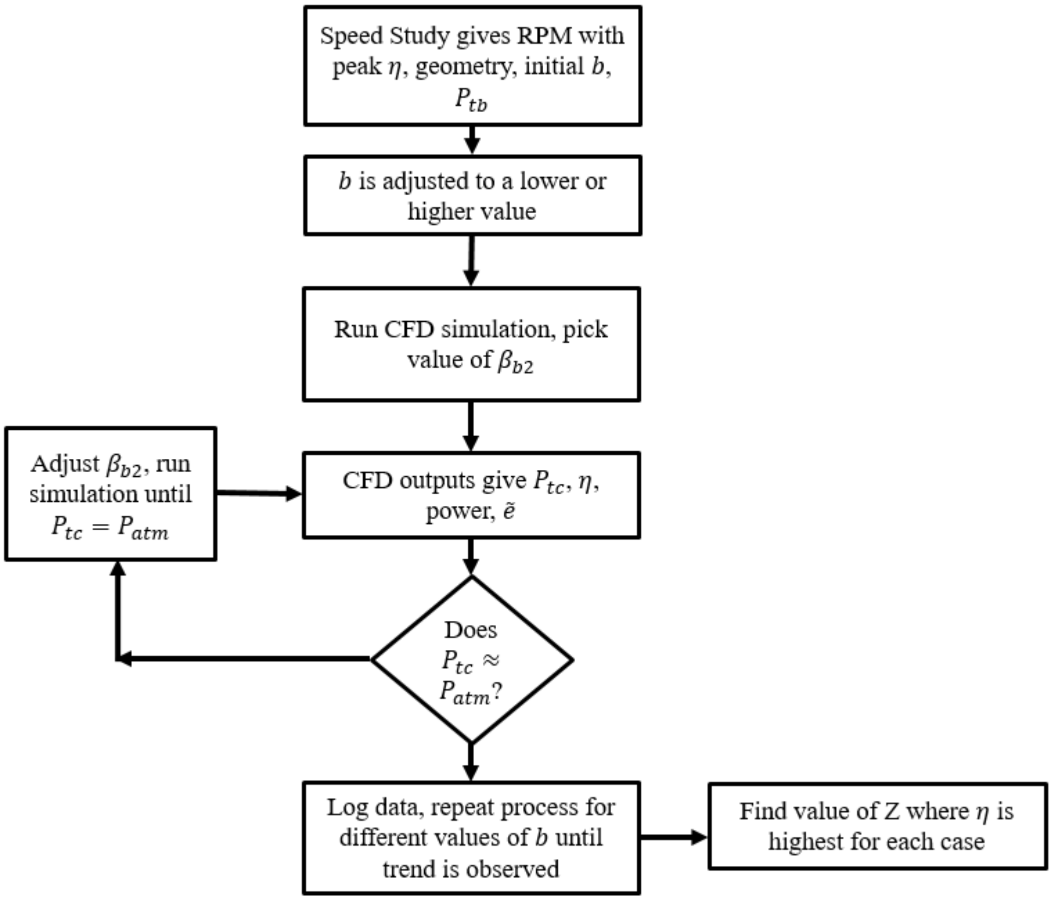

Figure 2.7. Blade Length Study process flow chart

Velocity triangles of the designs were produced, Figure 2.8 and 2.9 shows velocity triangles at leading and trailing edges for designs 2l and 2l8 of the Speed Study respectively, superimposed over the blade profile design produced using BladeGen.

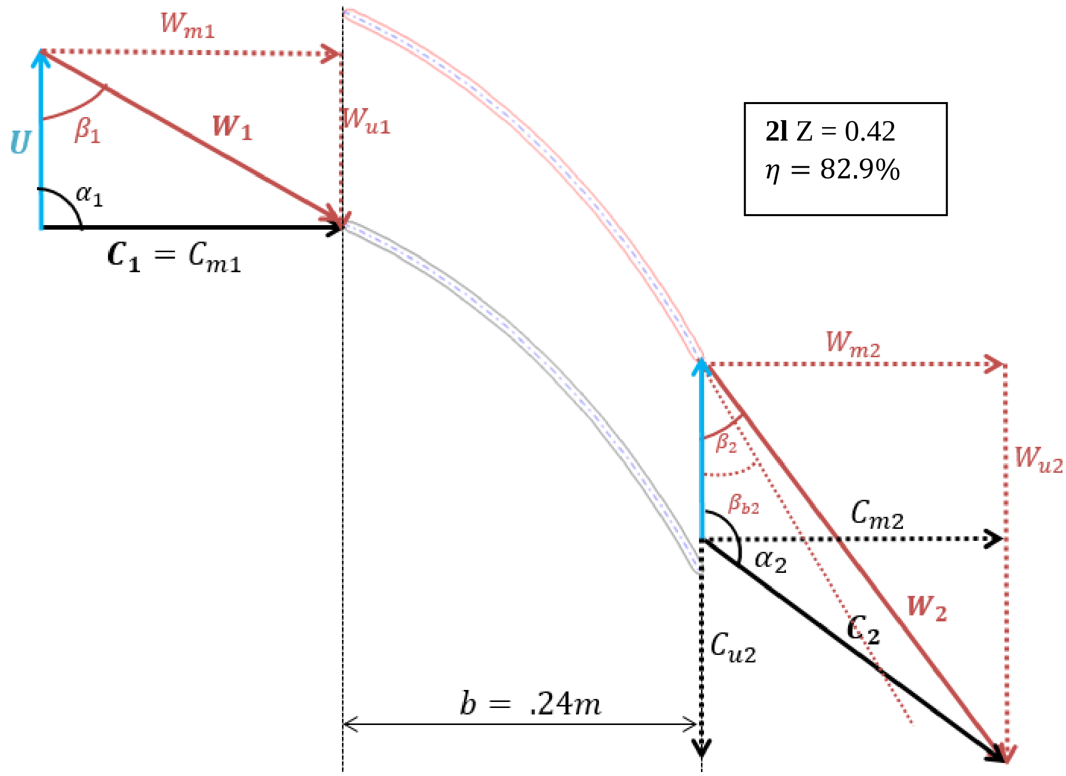

Figure 2.8. Velocity triangles for leading and trailing edges of design 2l of the Blade Length Study (50% span)

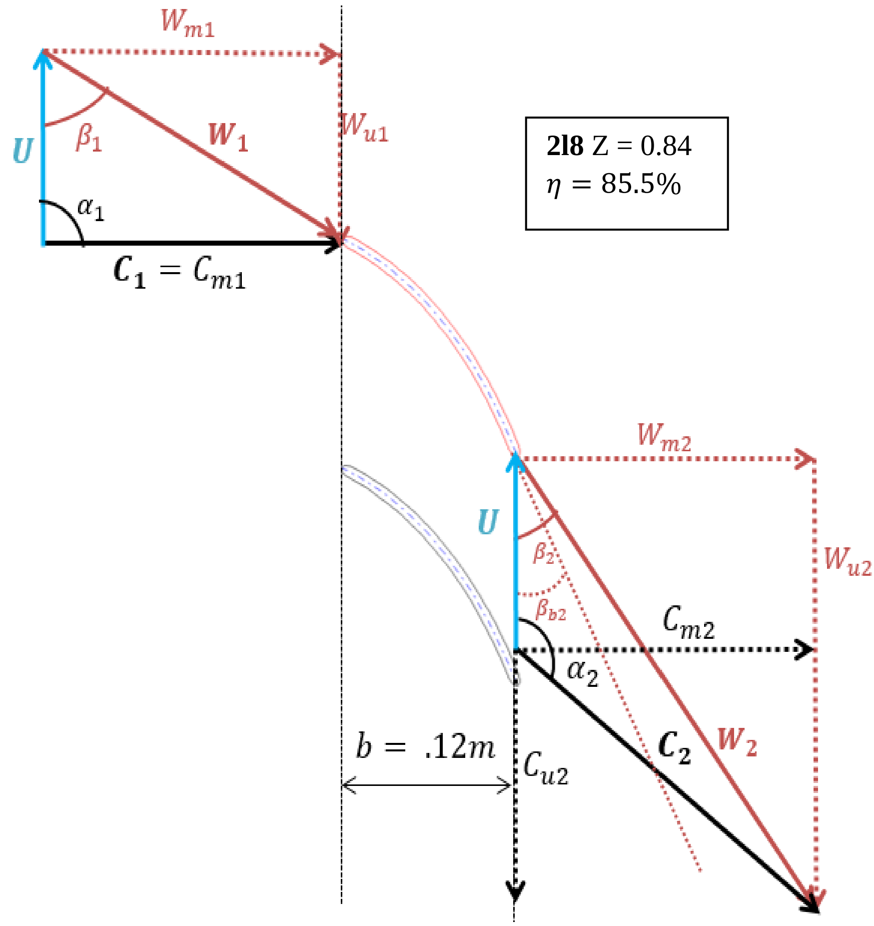

Figure 2.9. Velocity triangles for leading and trailing edges of design 2l8 of the Blade Length Study (50% span)

At least eight designs with differing blade lengths were simulated for each case. Designs with blade lengths corresponding to Zweifel coefficients from .36 to 1.49 were simulated for the Blade Length Study. The below Table 2.7 shows each simulation which was run for the Blade Length Study, showing the blade length and Zweifel coefficient for each design.

Table 2.8. Blade Length Study Runs and Inputs

Case	**Run**	$b\ (m)$	**Z**	**Case**	**Run**	$b\ (m)$	**Z**	**Case**	**Run**	$b\ (m)$	**Z**
1j	1	0.162	0.48	**2l**	1	0.24	0.42	**3n**	1	0.40	0.40
1j	2	0.122	0.63	**2l**	2	0.19	0.53	**3n**	2	0.35	0.46
1j	3	0.090	0.85	**2l**	3	0.15	0.67	**3n**	3	0.30	0.53
1j	4	0.070	1.09	**2l**	4	0.11	0.91	**3n**	4	0.25	0.64
1j	5	0.050	1.49	**2l**	5	0.08	1.24	**3n**	5	0.20	0.79
1j	6	0.190	0.41	**2l**	6	0.10	1.05	**3n**	6	0.15	1.05
1j	7	0.080	0.96	**2l**	7	0.13	0.78	**3n**	7	0.13	1.20
1j	8	0.096	0.80	**2l**	8	0.12	0.84	**3n**	8	0.11	1.42
-	-	-	-	-	-	-	-	**3n**	9	0.18	0.90
Case	**Run**	$b\ (m)$	**Z**	**Case**	**Run**	$b\ (m)$	**Z**	**Case**	**Run**	$b\ (m)$	**Z**
4h	1	0.16	0.40	**5n**	1	0.24	0.44	**6h**	1	0.40	0.44
4h	2	0.14	0.46	**5n**	2	0.27	0.39	**6h**	2	0.44	0.41
4h	3	0.18	0.36	**5n**	3	0.20	0.52	**6h**	3	0.47	0.38
4h	4	0.11	0.58	**5n**	4	0.16	0.65	**6h**	4	0.50	0.36
4h	5	0.08	0.80	**5n**	5	0.12	0.87	**6h**	5	0.37	0.48
4h	6	0.06	1.06	**5n**	6	0.10	1.03	**6h**	6	0.33	0.54
4h	7	0.09	0.71	**5n**	7	0.08	1.28	**6h**	7	0.29	0.61
4h	8	0.05	1.26	**5n**	8	0.11	0.94	**6h**	8	0.25	0.70
4h	9	0.07	0.91	**5n**	9	0.11	0.80	**6h**	9	0.21	0.83
-	-	-	-	-	-	-	-	**6h**	10	0.16	1.08
-	-	-	-	-	-	-	-	**6h**	11	0.13	1.31
-	-	-	-	-	-	-	-	**6h**	12	0.20	0.90

2.7. Mesh Independence Study

A mesh independence study was conducted first to ensure a fine enough mesh was used for each simulation to capture the flow features necessary to resolve the power, efficiency, and pressure difference accurately. Simulations with a finer mesh can resolve more flow details, but are more difficult to obtain convergence. A design was simulated for each case from the Speed Study, logging the performance characteristics, then the mesh size factor in ANSYS TurboGrid was changed systematically to see how mesh count affected power output. A base mesh count was picked at a point where increasing the mesh count further does not have a significant effect on power output. As each design has its own axial length, to ensure similarity across each design simulated, mesh density was kept constant across each design, such that the cell count per meter stays constant across each design per case. Figure 2.10 below shows the power output for a single design measured with different cell counts in case 1, Figure 2.11 shows this for case 2, Figure 2.12 shows this for case 3, Figure 2.13 shows this for case 4, Figure 2.14 shows this for case 5, Figure 2.15 shows this for case 6.

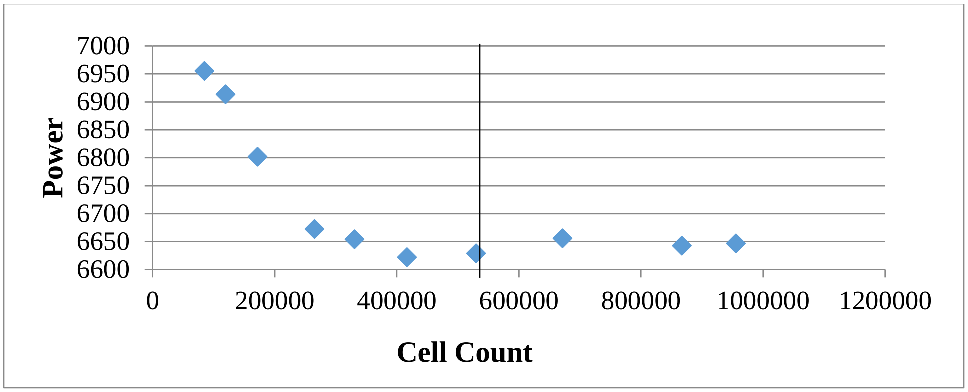

Figure 2.10. Mesh cell count vs. Power for case 1 mesh Study

Base mesh count of 550000 was used for the case 1 simulations, corresponding to an axial blade length of .14 meters. For case 1, simulations used a cell count of 3.9x10^6 cells/m.

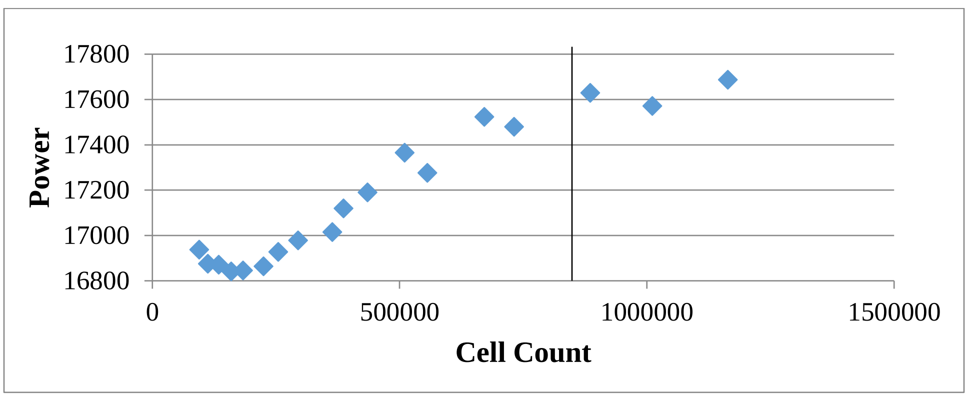

Figure 2.11. Mesh cell count vs. Power for case 2 mesh Study

A base mesh count of 800000 was used for the case 2 simulations, corresponding to an axial blade length of .16 meters. For case 2, simulations used a cell count of 5.0x10^6 cells/m.

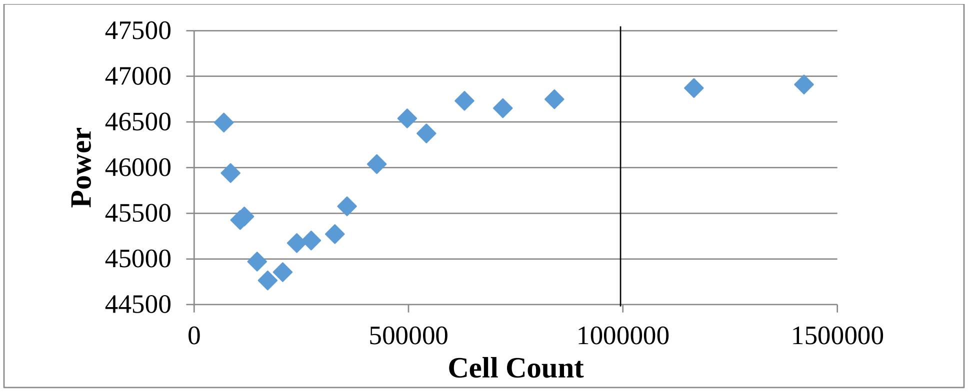

Figure 2.12. Mesh cell count vs. Power for case 3 mesh Study

A base mesh count of 1000000 was used for the case 3 simulations, corresponding to an axial blade length of .3 meters. For case 3, simulations used a cell count of 3.3x10^6 cells/m.

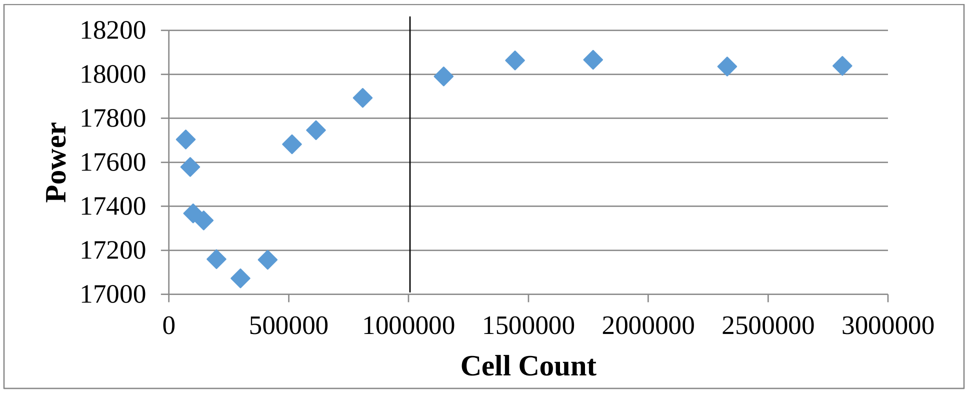

Figure 2.13. Mesh cell count vs. Power for case 4 mesh Study

A base mesh count of 1000000 was used for the case 4 simulations, corresponding to an axial blade length of .18 meters. For case 4, simulations used a cell count of 5.5x10^6 cells/m.

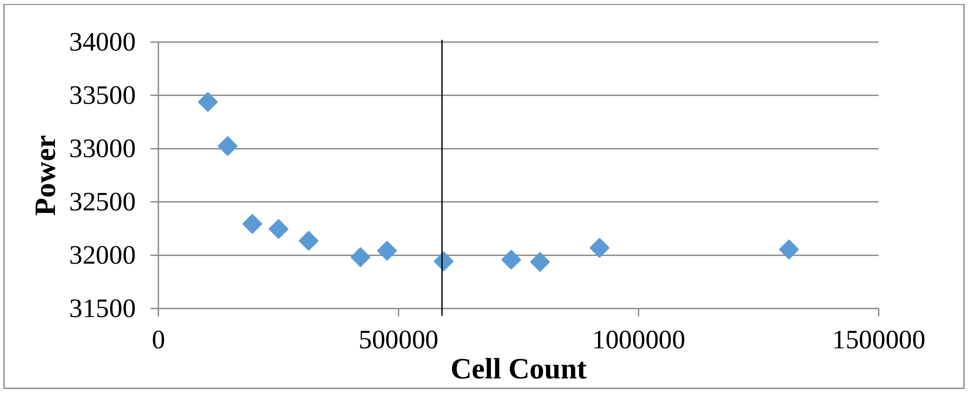

Figure 2.14. Mesh cell count vs. Power for case 5 mesh Study

A base mesh count of 600000 was used for the case 5 simulations, corresponding to an axial blade length of .2 meters. For case 5, simulations used a cell count of 3x10^6 cells/m.

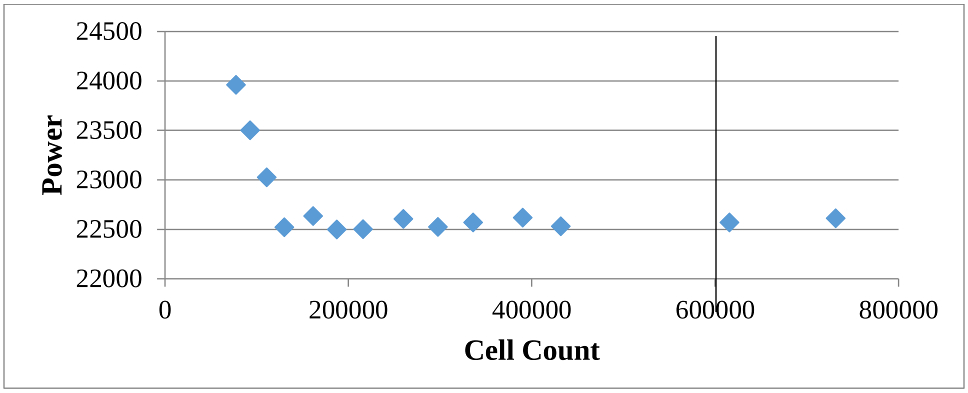

Figure 2.15. Mesh cell count vs. Power for case 6 mesh Study

A base mesh count of 600000 was used for the case 6 simulations, corresponding to an axial blade length of .25 meters. For case 6, simulations used a cell count of 2.4x10^6 cells/m.

CHAPTER 3. CFD RESULTS AND DISCUSSION

3.1. Speed Study CFD Results

The Speed Study tested designs with similar geometry at varying rotational speeds. Axial blade length was changed for each design such that $Z = .8$ for each design tested in the Speed Study. The below tables show how varying rotational speed effected efficiency for the different designs.

Table 3.1. Case 1 Speed Study CFD Results

Case 1	Case	Run	H(m)	b(m)	$\tilde{e}$ $(\frac{m^2}{s^2})$	Efficiency η	RPM	U (m/s)	ϕ	Ω_s	ψ	$\dot{W}$ (kW)
$\dot{V} = 0.46\frac{m^3}{s}$	1	b	1.88	0.045	14.38	77.09	350	7.33	0.79	2.80	0.27	6.62
$r_h = .12$ m	1	d	1.86	0.056	14.60	79.04	300	6.28	0.92	2.41	0.37	6.72
$r_s = .2$ m	1	f	1.86	0.070	14.69	79.66	250	5.24	1.12	2.01	0.54	6.76
	1	h	1.84	0.086	14.69	80.47	200	4.19	1.39	1.62	0.84	6.76
	1	j	1.85	0.098	14.77	80.58	170	3.56	1.63	1.37	1.17	6.79
	1	l	1.88	0.106	14.45	77.53	140	2.93	1.98	1.12	1.68	6.65
	1	CORD.	2.07	0.022	6.45	34.87	737	15.44	0.38	5.47	0.03	2.97

Peak efficiency was observed at a specific speed of 1.4, RPM 170. Decreased efficiency was measured at rotational speeds above 300 RPM.

Table 3.2. Case 2 Speed Study CFD Results

Case 2	Case	Run	H(m)	b(m)	$\tilde{e}$ $(\frac{m^2}{s^2})$	Efficiency η	RPM	U (m/s)	ϕ	Ω_s	ψ	$\dot{W}$ (kW)
$\dot{V} = 1.050\frac{m^3}{s}$	2	b	1.90	0.031	13.62	73.35	350	11.00	0.53	4.19	0.11	14.30
$r_h = .2$ m	2	d	1.85	0.044	14.64	78.62	300	9.42	0.62	3.67	0.16	15.37
$r_s = .3$ m	2	f	1.88	0.060	15.31	82.48	250	7.85	0.75	3.01	0.25	16.08
	2	h	1.88	0.086	15.93	84.95	200	6.28	0.94	2.42	0.40	16.73
	2	j	1.88	0.105	16.02	85.38	170	5.34	1.10	2.05	0.56	16.83
	2	l	1.85	0.126	15.85	85.49	140	4.40	1.34	1.71	0.82	16.64
	2	n	1.87	0.142	15.80	84.65	120	3.77	1.56	1.45	1.11	16.59
	2	CORD.	1.92	0.027	10.07	52.57	497	15.61	0.38	5.91	0.04	10.57

Peak efficiency was observed at a specific speed of 1.7, RPM of 140. A sharp decrease in efficiency was measured at rotational speeds above 250 RPM.

Table 3.3. Case 3 Speed Study CFD Results

Case 3	Case	Run	H(m)	b(m)	$\tilde{e}$ $(\frac{m^2}{s^2})$	Efficiency η	RPM	U (m/s)	ϕ	Ω_s	ψ	$\dot{W}$ (kW)
$\dot{V} = 2.85 \frac{m^3}{s}$	3	f	1.90	0.034	15.45	82.56	250	13.09	0.45	4.92	0.09	44.04
$r_h = .3$ m	3	h	1.89	0.061	15.58	83.98	200	10.47	0.56	3.96	0.14	44.41
$r_s = .5$ m	3	j	1.92	0.104	16.65	88.24	150	7.85	0.74	2.94	0.27	47.44
	3	l	1.91	0.148	16.83	89.59	120	6.28	0.93	2.36	0.43	47.97
	3	n	1.88	0.199	16.59	89.76	90	4.71	1.24	1.79	0.75	47.28
	3	p	1.88	0.260	16.14	87.39	60	3.14	1.86	1.19	1.64	46.01
	3	CORD.	1.84	0.042	12.40	68.15	295	15.45	0.38	5.95	0.05	35.35

Peak efficiency was observed at a specific speed of 1.8, corresponding to an RPM of 90. A sharp decrease in efficiency was measured at rotational speeds above 150 RPM.

Table 3.4. Case 4 Speed Study CFD Results

Case 4	Case	Run	H(m)	b(m)	$\tilde{e}$ $(\frac{m^2}{s^2})$	Efficiency η	RPM	U (m/s)	ϕ	Ω_s	ψ	$\dot{W}$ (kW)
$\dot{V} = 0.6 \frac{m^3}{s}$	4	b	3.73	0.05	29.43	79.62	450	9.42	0.80	2.45	0.33	17.66
$r_h = .12$ m	4	d	3.72	0.06	29.89	81.05	400	8.38	0.90	2.19	0.43	17.93
$r_s = .2$ m	4	f	3.68	0.07	29.92	81.96	350	7.33	1.03	1.93	0.56	17.95
	4	h	3.70	0.08	30.11	81.99	300	6.28	1.20	1.64	0.76	18.07
	4	j	3.70	0.09	29.81	81.22	250	5.24	1.45	1.37	1.09	17.89
	4	l	3.70	0.10	29.30	79.98	220	4.61	1.64	1.21	1.38	17.58
	4	n	3.70	0.05	28.61	77.94	500	10.47	0.72	2.74	0.26	17.16
	4	CORD.	3.73	0.03	13.95	37.98	997	20.88	0.36	5.44	0.03	8.37

Peak efficiency was observed at a specific speed of 1.6, RPM of 300. Decreased efficiency was measured at rotational speeds above 400 RPM.

Table 3.5. Case 5 Speed Study CFD Results

Case 5	Case	Run	H(m)	b(m)	$\tilde{e}$ $(\frac{m^2}{s^2})$	Efficiency η	RPM	U (m/s)	ϕ	Ω_s	ψ	$\dot{W}$ (kW)
$\dot{V} = 1.5 \frac{m^3}{s}$	5	b	3.73	0.04	28.62	77.54	450	14.14	0.59	3.88	0.14	42.93
$r_h = .2$ m	5	d	3.67	0.05	29.36	80.70	400	12.57	0.67	3.49	0.19	44.04
$r_s = .3$ m	5	f	3.71	0.06	30.01	82.43	350	11.00	0.76	3.03	0.25	45.01
	5	h	3.70	0.08	31.18	85.21	300	9.42	0.89	2.60	0.35	46.77
	5	j	3.72	0.10	31.69	86.17	250	7.85	1.07	2.16	0.51	47.54
	5	l	3.72	0.11	31.62	86.29	220	6.91	1.21	1.90	0.66	47.43
	5	n	3.70	0.13	31.64	85.96	190	5.97	1.41	1.65	0.89	47.47
	5	p	3.72	0.15	30.15	82.82	160	5.03	1.67	1.38	1.19	45.23
	5	CORD.	3.68	0.04	19.13	52.44	704	22.12	0.38	6.13	0.04	28.69

Peak efficiency was observed at a specific speed of 1.7, RPM of 190. A sharp decrease in efficiency was measured at rotational speeds above 300 RPM.

Table 3.6. Case 6 Speed Study CFD Results

Case 6	Case	Run	H(m)	b(m)	$\tilde{e}$ ($\frac{m^2}{s^2}$)	Efficiency η	RPM	U (m/s)	ϕ	Ω_s	ψ	$\dot{W}$ (kW)
$\dot{V} = 4.1\frac{m^3}{s}$	6	b	3.79	0.11	33.37	89.22	200	10.47	0.79	2.82	0.30	136.83
$r_h = .3$ m	6	d	3.79	0.14	33.65	90.02	170	8.90	0.93	2.39	0.42	137.97
$r_s = .5$ m	6	f	3.78	0.18	33.70	90.21	140	7.33	1.13	1.98	0.63	138.17
	6	h	3.78	0.22	33.44	89.70	110	5.76	1.43	1.55	1.01	137.12
	6	j	3.79	0.26	32.61	87.25	80	4.19	1.97	1.13	1.86	133.70
	6	l	3.75	0.08	32.12	86.74	250	13.09	0.63	3.55	0.19	131.68
	6	CORD.	3.69	0.06	25.08	68.84	419	21.94	0.38	6.02	0.05	131.68

Peak efficiency was observed at a specific speed of 2.0, RPM of 140. Decreased efficiency was measured at rotational speeds above 170 RPM.

3.2. Discussion of Cordier Recommendations and Location on Diagram

The specific speed (and rotational speed) recommended by the Cordier line are greater than the speed at which highest efficiency was measured in the CFD simulations. The efficiency at the Cordier-recommended speed was lower for each case tested in the Speed Study; however cases 3 and 6, which had the largest flow rate, had the smallest decrease in efficiency as speed increased. The efficiency obtained in CFD was graphed against the specific speed for each case in the Speed Study, shown in Figure 3.1 below.

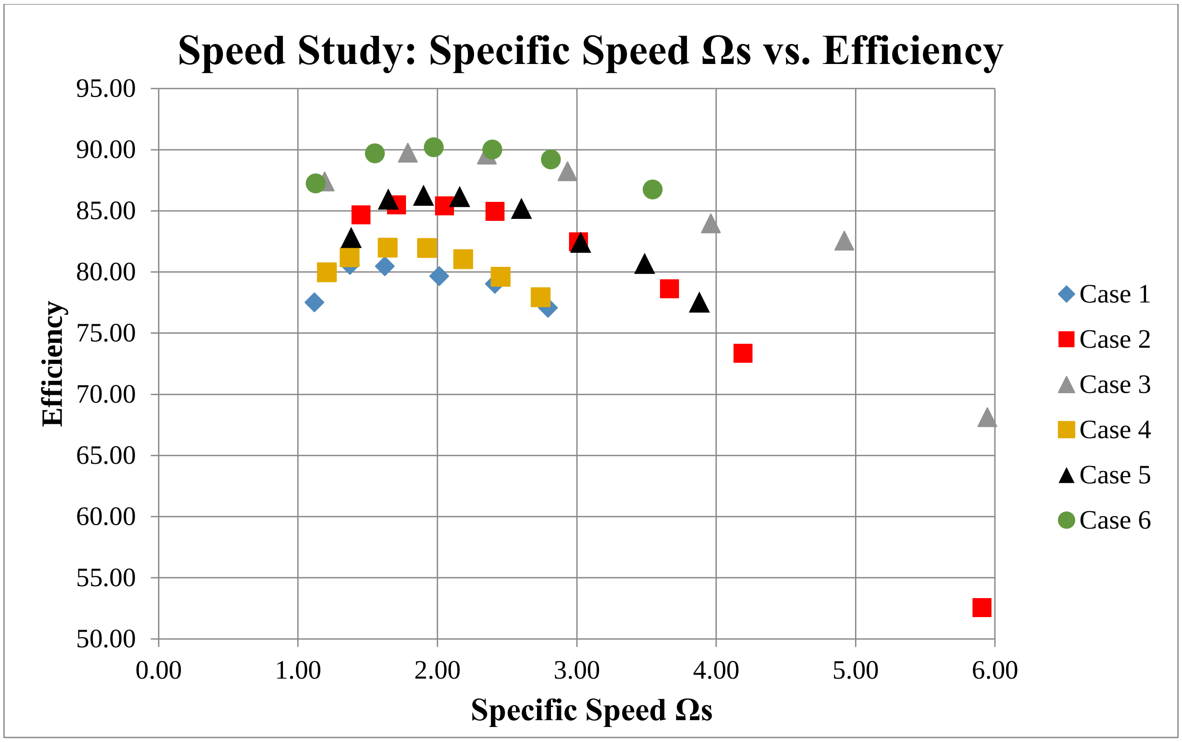

Figure 3.1 Specific speed Ω_s Vs. Efficiency of Speed Study designs

Efficiency at the specific speeds recommended by the Cordier line was lower than the efficiency at lower rotational speeds. Highest values of efficiencies were measured at specific speeds Ω_s between 1.4 and 1.9, lower than the values of specific speed which were recommended by the Cordier line, between 5.5 and 6.1. The highest efficiency was measured for the designs which ran at speeds between 12 and 33% of the Cordier-recommended speed. The RPM, specific speed, and specific diameter where highest efficiency was measured in CFD for each case was logged, and compared to efficiency at the RPM and specific speed recommended by the Cordier line, recorded below in Table 3.7.

Table 3.7. Performance of Cordier Recommendations of Cases in Speed Study

Case	Units	1	2	3	4	5	6
H	m	1.85	1.88	1.91	3.70	3.70	3.70
r_s	m	0.2	0.3	0.5	0.2	0.3	0.5
r_h	m	.12	.18	.3	.12	.18	.3
$\dot{V}$	$\frac{m^3}{s}$	0.46	1.05	2.85	0.60	1.50	4.10
D_s		1.218	1.214	1.232	1.268	1.202	1.212
RPM at highest η	RPM	170	140	90	300	90	140
Ω_s (highest η)	rad	1.37	1.69	1.77	1.65	0.78	2.01
Highest η from Speed Study	%	80.58	85.49	89.76	81.99	85.96	90.21
Cordier Recommendations: Changing Speed							
Ω_s (Cordier)	rad	5.9	6.0	5.8	5.5	6.1	6.0
RPM (Cordier)	RPM	737	497	295	997	704	419
U (Cordier)	m/s	15	16	15	21	22	22
η at Cordier point	%	34.87	52.57	68.15	37.98	52.44	68.84

The below Figure 3.2 shows the six highest efficiency cases from the first study placed on the Cordier diagram from Wright [18].

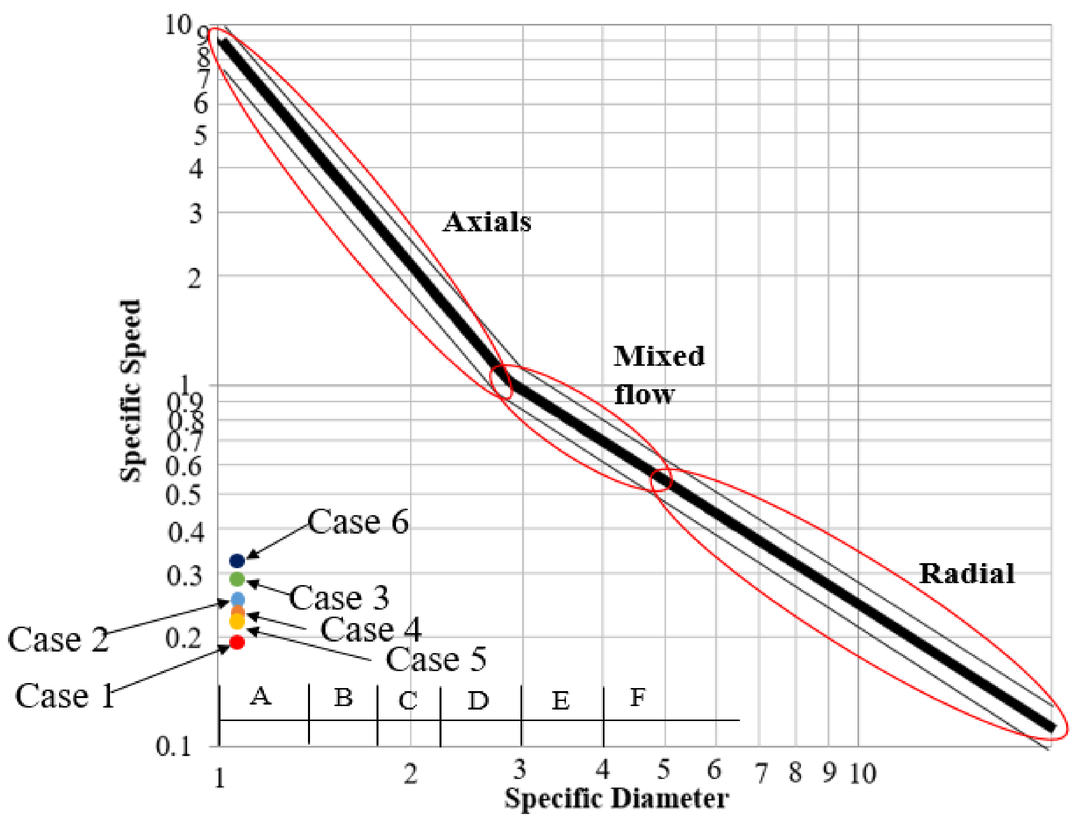

Figure 3.2. Location of peak efficiency points for each case on Ω_s vs D_s diagram with Cordier line

Although the designs have specific diameter which the literature would recommend using an axial turbine, the designs with highest efficiency measured in the CFD study were located below the Cordier line, at rotational speeds less than half of that recommended by the Cordier line. The peak efficiency designs operated at specific speeds which were close to the specific speeds at which radial turbines typically operate. The specific diameter of the designs suggest the designs fall into Wright's region A on the Cordier diagram, typically populated by axial turbines. The specific speeds of the peak efficiency designs, however, fit with Wright's region F on the Cordier diagram, where high pressure blowers, centrifugal compressors, and high head liquid pumps are typically used.

3.3. Discussion of Speed Study Results

3.3.1. Overall Summary

For each of the designs simulated in the Speed Study, specific diameter was relatively constant, and had a value of D_s between 1.20 and 1.27. The Speed Study analysis used three sets of hub and shroud radii and blade thickness, with two values of total available head. Cases 1 and 4, 2 and 5, and 3 and 6 had the similar geometry, and had similar efficiencies, although the higher head designs (4 meters) were slightly higher efficiency than the designs for 2 meters. For each of the cases it was observed that as specific speed Ω_s was increased past 2, turbine efficiency decreased. This is shown in Figure 3.3. As rotational speed was changed, tip speed U changed, and flow coefficient φ changed. The below Figure 3.4, which shows efficiency graphed vs. flow coefficient, designs which had flow coefficients between 1.1 and 1.6 had the highest efficiency measured in simulations. Efficiency was lowest in the designs with the lowest flow coefficients, where rotational speed was high.

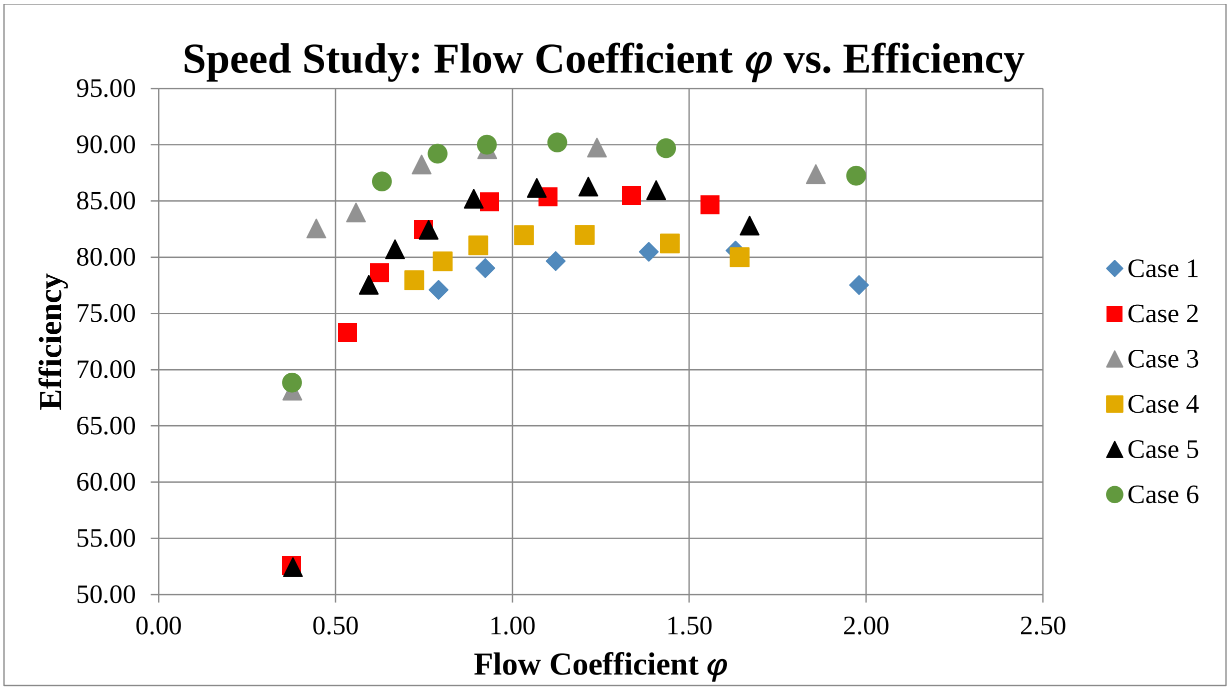

Figure 3.3 Flow coefficient vs. Efficiency of Speed Study designs

Designs which produced the highest efficiency had blade loading coefficients between 0.63 and 1.17. This is shown below in Figure 3.4. Efficiency was lowest for the designs with the lowest head coefficients, the designs which ran with Ω_s above 2.5.

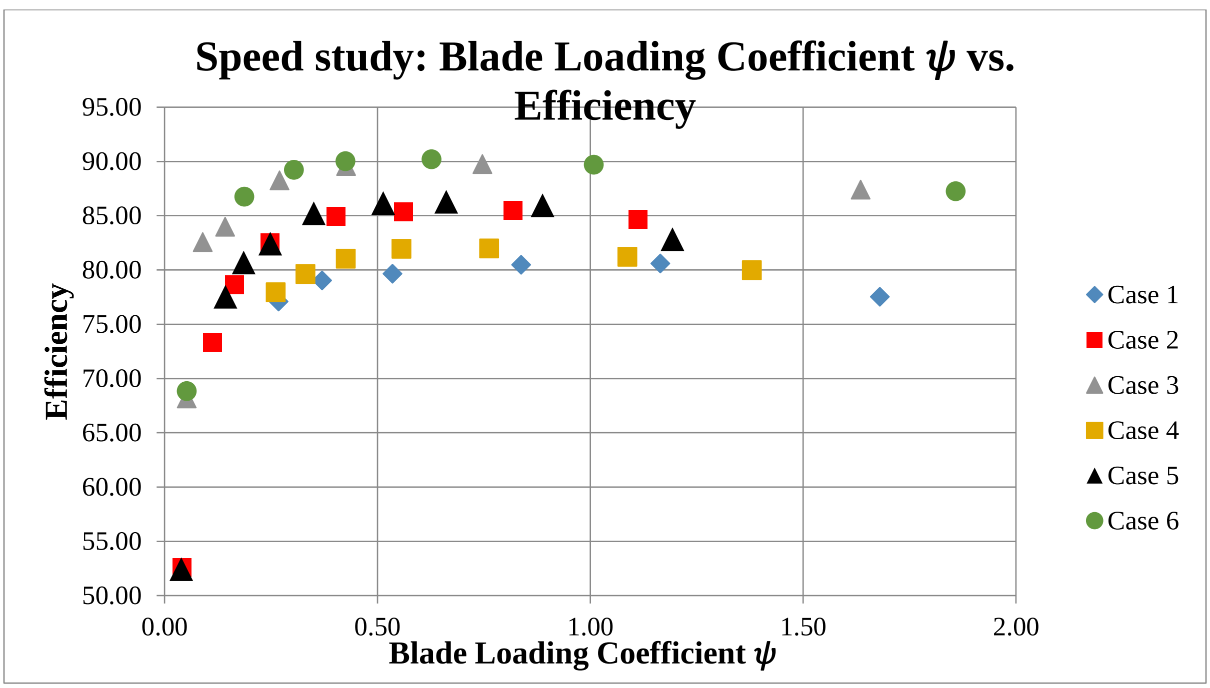

Figure 3.4. Blade loading coefficient vs. Efficiency of Speed Study designs

3.3.2. Flow Visualization and Vectors

The simulations of designs with high rotational speed predicted flows with higher relative flow speed. The higher speed designs also experienced larger flow velocity gradients at the leading and trailing edges. Towards the trailing edge on the pressure side, the flow accelerated and pressure decreased. This effect was more severe for higher rotational speed designs. Relative velocity vector diagrams were generated for each design, and show the velocity gradients at the leading and trailing edges. Figure 3.5 shows the flow of three designs in case 1, Figure 3.6 shows the flow of three designs in case 2, Figure 3.7 shows the flow of three designs in case 3, Figure 3.8 shows the flow of three designs in case 4, Figure 3.9 shows the flow of three designs in case 5, Figure 3.10 shows the flow of three designs in case 6.

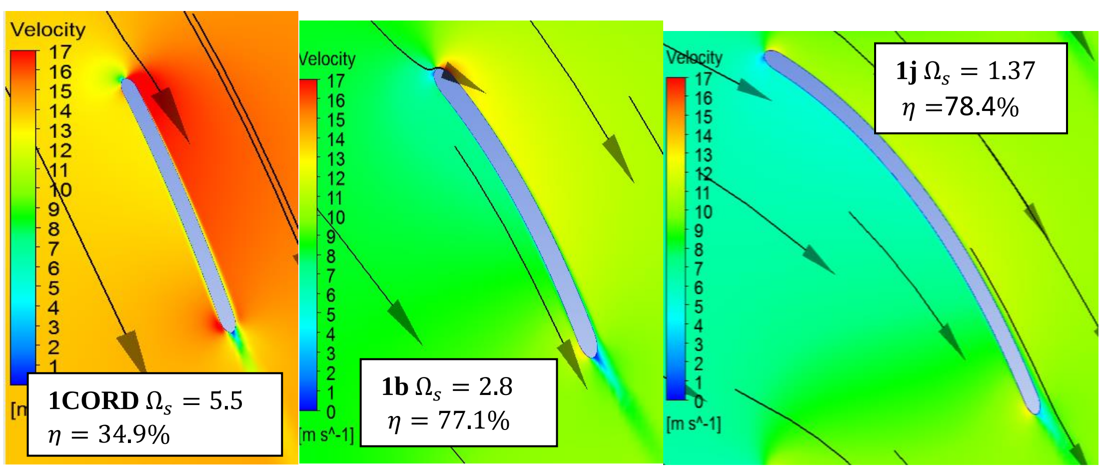

Figure 3.5. Relative velocity vectors for case 1: Span 50%

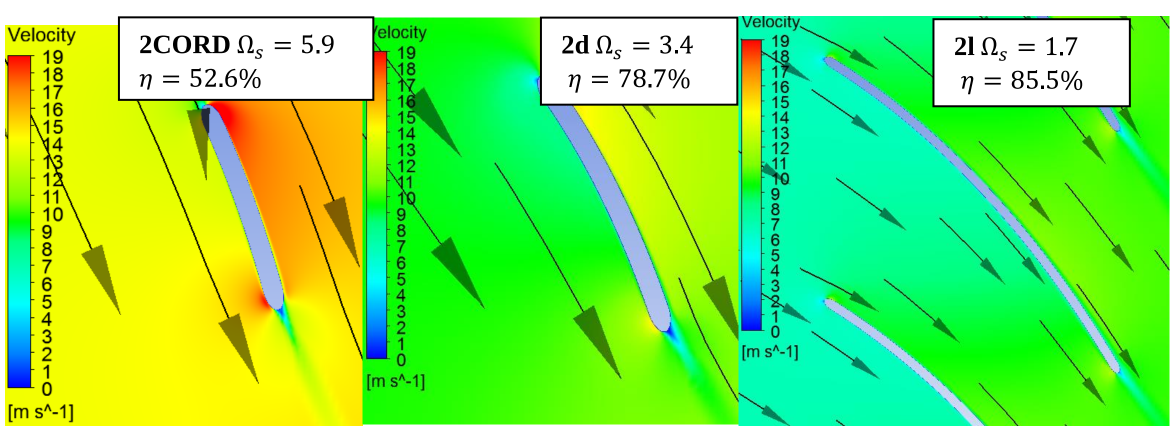

Figure 3.6. Relative velocity vectors for case 2: Span 50%

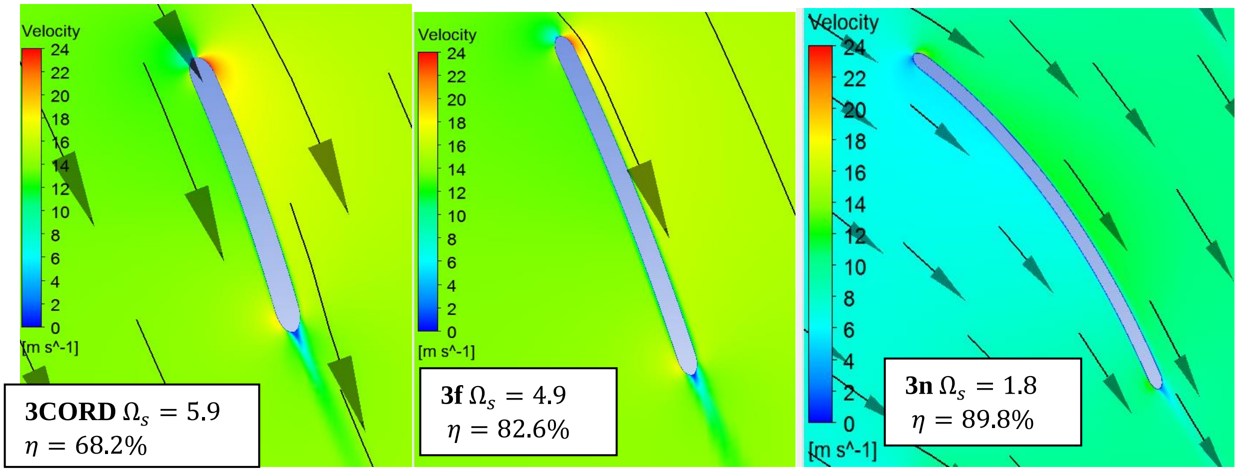

Figure 3.7. Relative velocity vectors for case 3: Span 50%

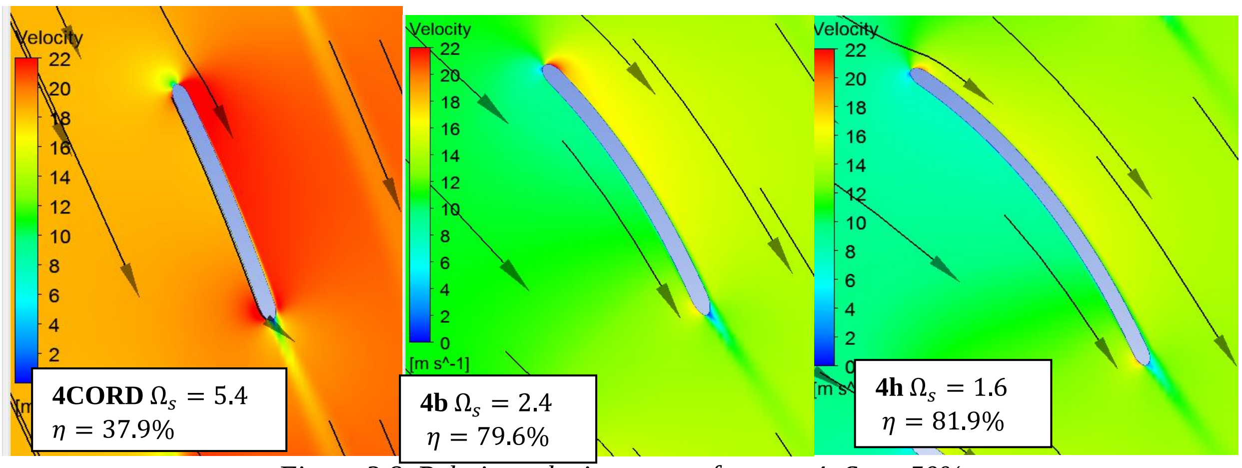

Figure 3.8. Relative velocity vectors for case 4: Span 50%

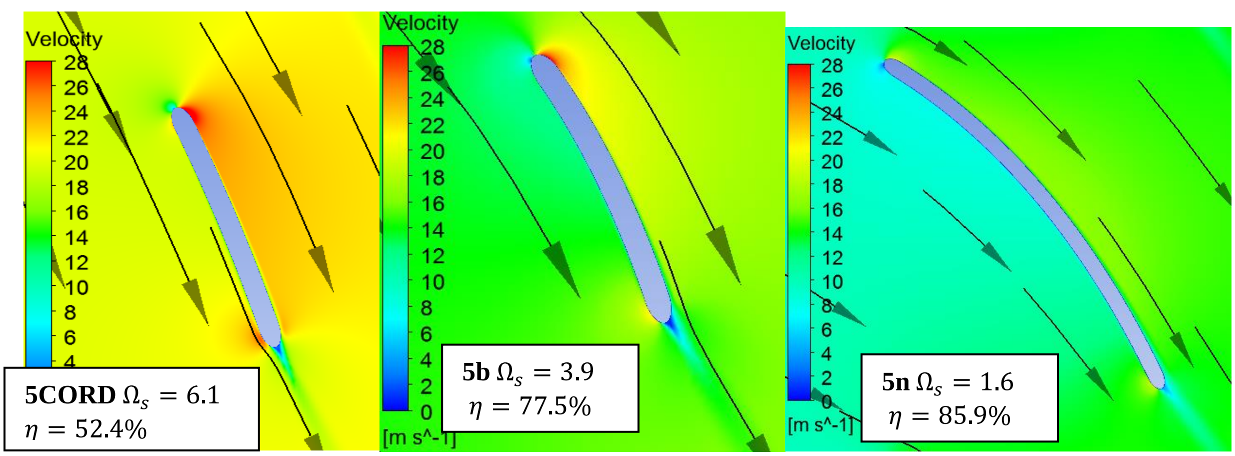

Figure 3.9. Relative velocity vectors for case 5: Span 50%

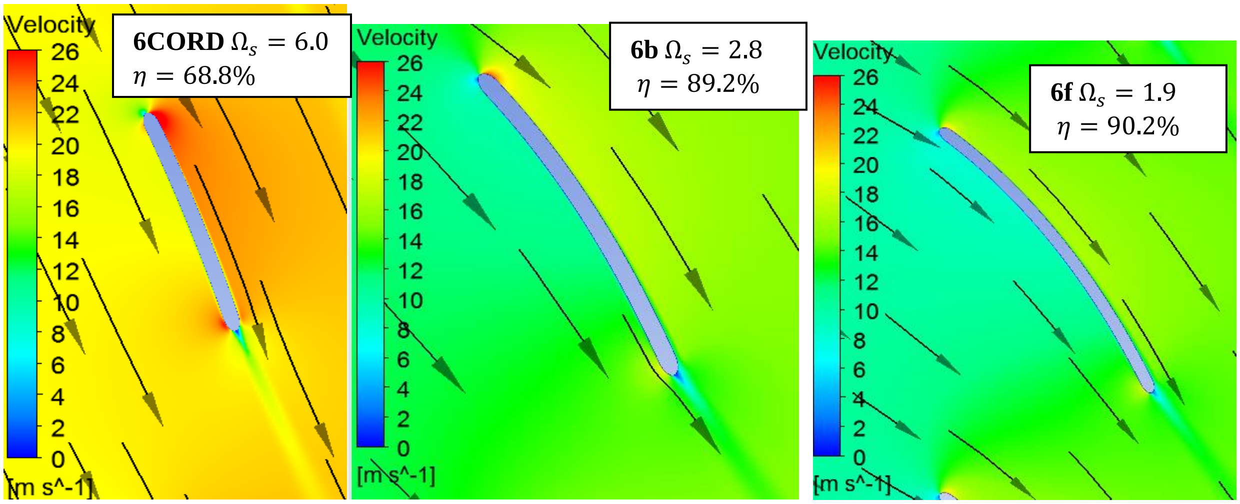

Figure 3.10. Relative velocity vectors for case 6: Span 50%

To show additional flow details, more detailed relative flow velocity vector diagrams were generated at the leading and trailing edges using the simulation results of each design. Figures 3.12, 3.13, and 3.14 show relative velocity vectors at leading edge for three designs within cases 2,1, and 3 respectively. At the leading edge, a region of flow deceleration was measured on the pressure side, located close to a region of rapid flow acceleration towards the suction side. The higher speed designs exhibited flows with a higher magnitude flow deceleration on the leading edge pressure side, and higher flow acceleration near the leading edge suction side. This same effect was observed for each of the cases simulated.

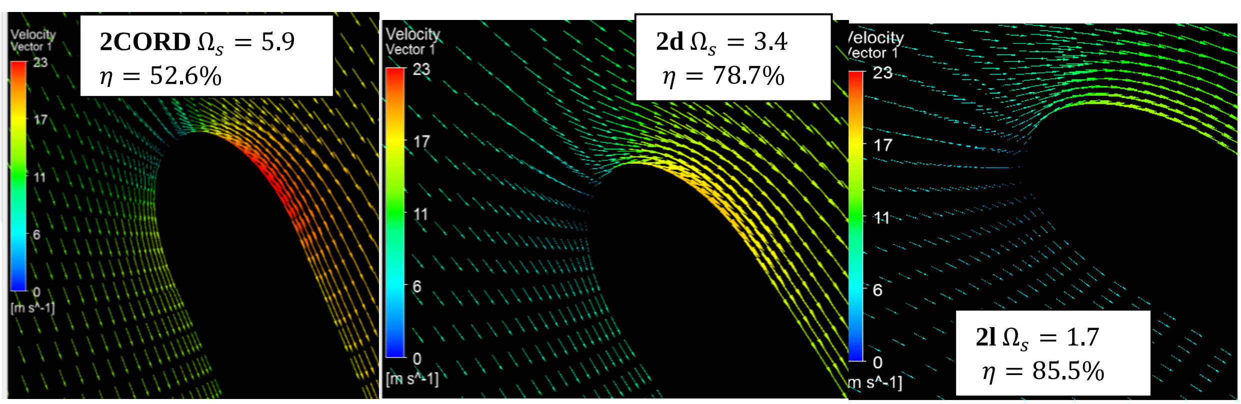

Figure 3.11. Relative velocity vectors at leading edge for case 2: 50% span

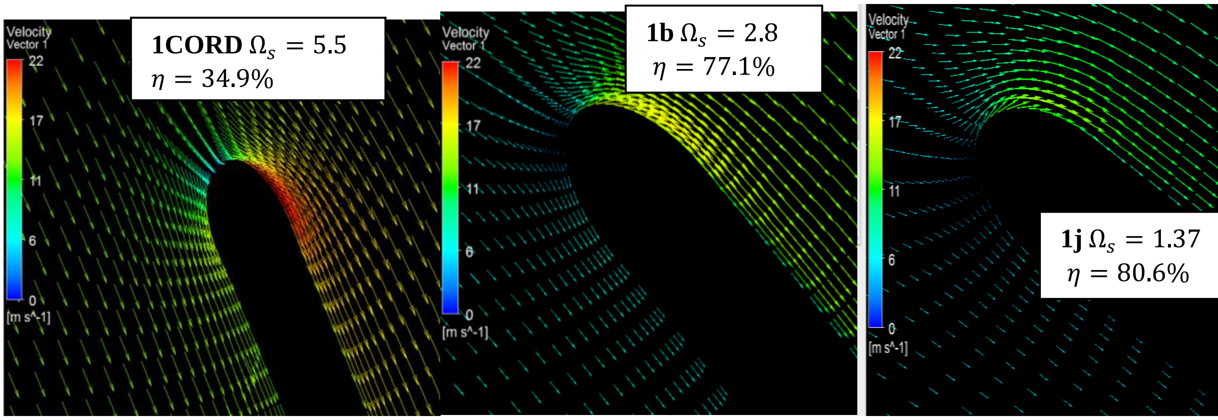

Figure 3.12. Relative velocity vectors at leading edge for case 1: Span 50%

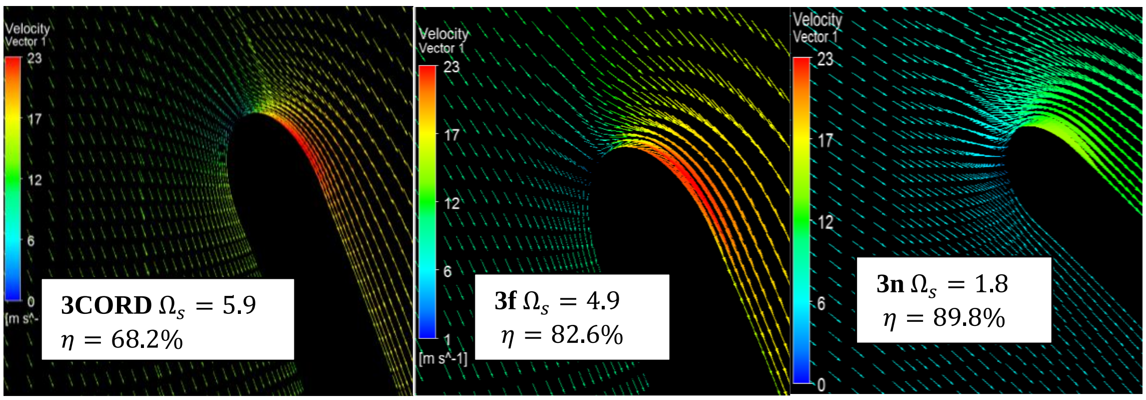

Figure 3.13. Relative velocity vectors at leading edge for case 3: Span 50%

Similarly, vector diagrams were produced for the trailing edge. The flow for the higher speed designs experienced more severe velocity gradients at and after the trailing edge. This relationship was observed for every case simulated in the Speed Study. This is shown below in Figure 3.14 for case 2, Figure 3.15 for case 1, and Figure 3.16 for case 3.

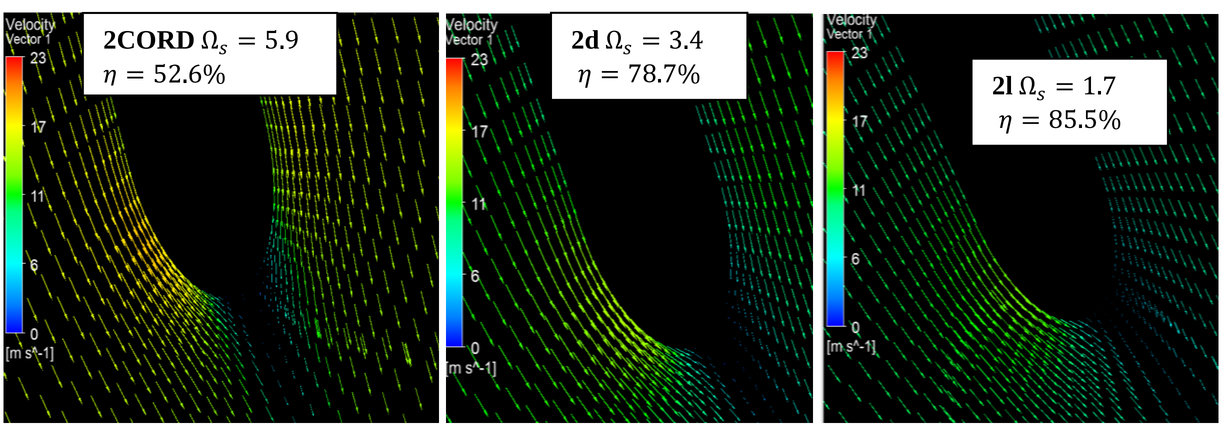

Figure 3.14. Relative velocity vectors at trailing edge for case 2: 50% span

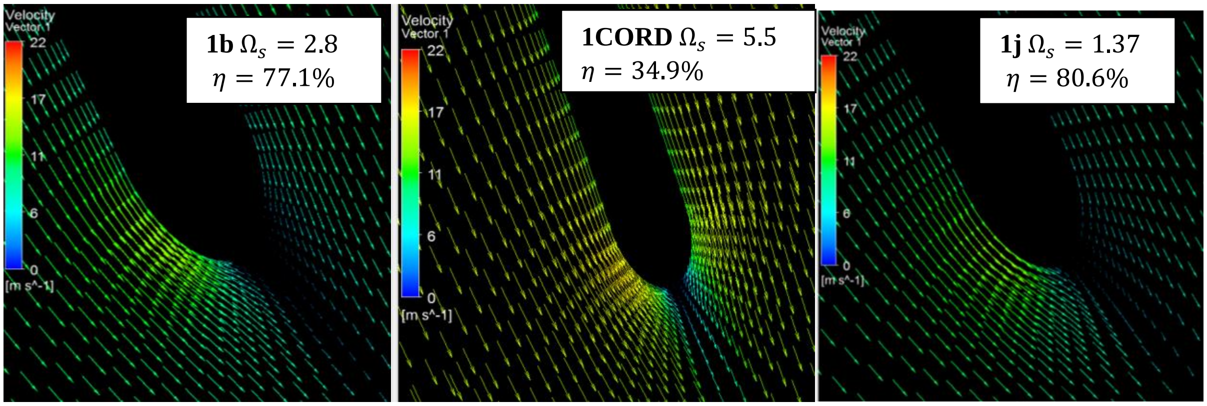

Figure 3.15. Relative velocity vectors at trailing edge for case 1: 50% span

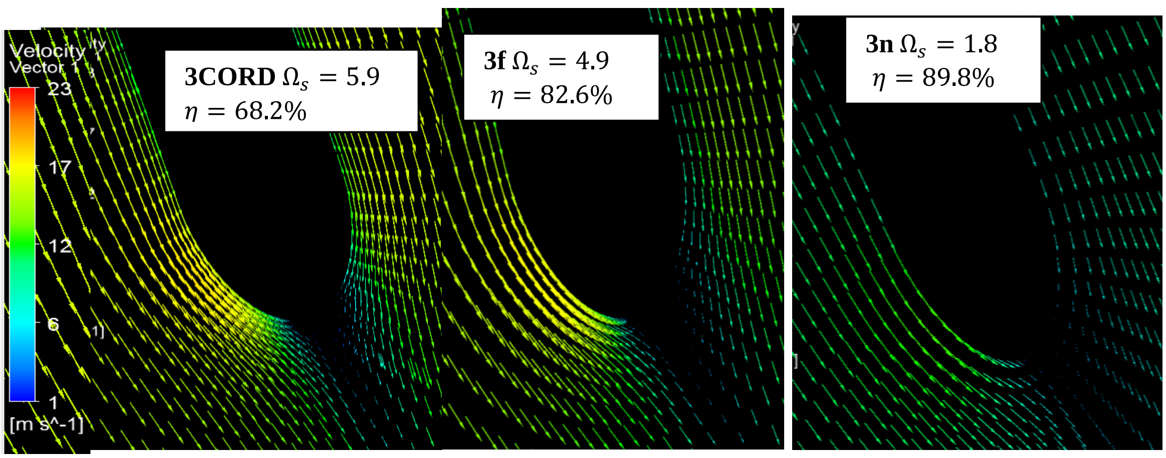

Figure 3.16. Relative velocity vectors at trailing edge for case 3: Span 50%

3.3.3 Trailing Edge Effects

The above figures illustrate how varying rotational speed effected velocity gradients at the trailing edge. If the magnitude of the velocity gradients at the trailing edge are larger, additional viscous shear could occur, resulting in flow turbulence and entropy generation [35]. The designs with higher speed exhibited flows with more extreme velocity gradients at the trailing edge, which results in added viscous shear compared to the lower speed designs. The designs recommended by the Cordier line experienced the largest velocity gradients at the trailing edge, as well as the largest flow deceleration measured after the trailing edge. This effect was observed for every case simulated in the Speed Study.

Flow will be more turbulent in areas where velocity gradients are more severe, and the higher speed designs in the Speed Study experienced greater velocity gradients at the trailing edge. Turbulence kinetic energy was recorded to track the effect of increasing rotational speed on turbulence. Turbulence kinetic energy at and after the trailing edge was higher for the designs which operated at higher rotational speeds. Figure 3.17 shows a contour of turbulence kinetic energy for two designs 3Cord, 3n, and Figure 3.18 shows this for two designs in case 1, 1Cord and 1j.

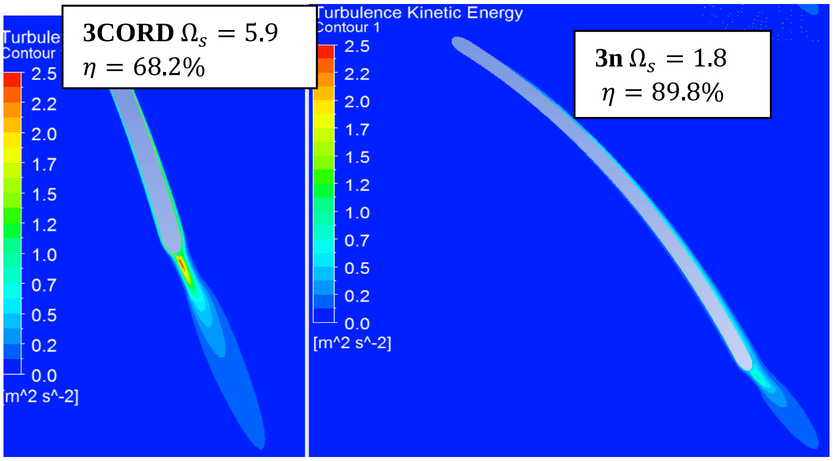

Figure 3.17. Turbulence kinetic energy contours for case 3: Span 50%

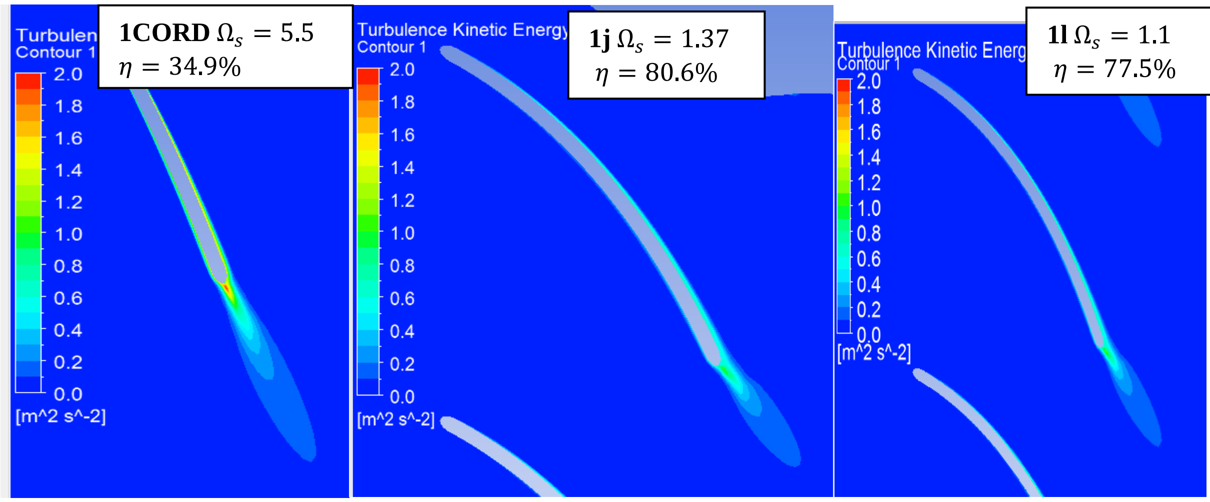

Figure 3.18. Turbulence kinetic energy contours for case 1: Span 50%

Figure 3.19 below shows the relative flow velocity for simulations of designs 1b ,1j and 1Cord of case 1 logged from 80% along the blade chord to the trailing edge. These figures illustrate the flow acceleration at the pressure side near the trailing edge, and rapid flow deceleration near the trailing edge on the suction side. As rotational speed was increased, flow velocity at the pressure side trailing edge increased and velocity at the suction side trailing edge decreased. This was observed for every case simulated in the Speed Study.

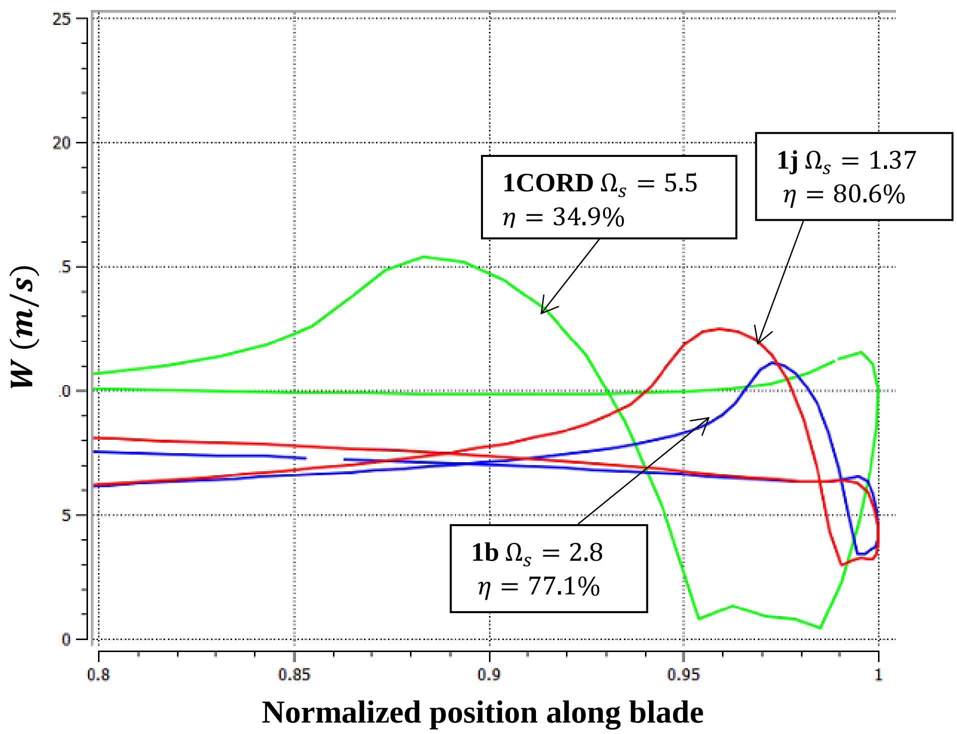

Figure 3.19. Relative velocity of case 1 Speed Study designs near the trailing edge: Span 50%

3.3.4. Blade Loading

Simulations showed that for the higher speed designs, the adverse pressure gradient on the suction side of the blades after the point of minimum pressure became more severe. Another adverse pressure gradient at the trailing edge at the suction side became more severe as speed increased. Adverse pressure gradients are correlated with boundary layer growth, entropy generation, and increased losses [35].

For each of the designs simulated in CFD, highest pressure was measured at the leading edge at the pressure side where flow was decelerated, the higher rotational speed designs demonstrated a higher pressure at this point. This effect was most extreme for the designs with rotational speeds recommended by the Cordier line. This point was located close to an area of lower pressure at the leading edge on the suction side, where flow accelerates. Simulations of the designs with higher rotational speed predicted decreased pressure at this point compared to lower speed designs. This effect was observed for each case simulated in the Speed Study. For many designs, at this point pressure reached below vapor pressure.

Towards the trailing edge on the pressure side, the flow accelerates and pressure decreases. This effect was magnified for higher rotational speed designs. The designs with Cordier speed experienced the most severe drop in pressure near the trailing edge on the pressure side. The area of low pressure at the trailing edge pressure side takes up a larger portion of the blade chord for the higher speed designs. Near the trailing edge on the suction side, pressure increases as the flow decelerates. Each of the higher rotational speed designs simulated recorded greater flow deceleration near the trailing edge on the suction side of the blades as the flow experienced an adverse pressure gradient. This is illustrated in blade loading diagrams for two of the cases, which chart pressure on the blades over the normalized position along the blade chord. Figure 3.20 shows design 2d, 2l, and the Cordier-recommended design for case 2, 2Cord, and Figure 3.21 shows design 1b, 1j, and the Cordier-recommended design for case 1, 1Cord. The adverse pressure gradients are highlighted with thicker lines.

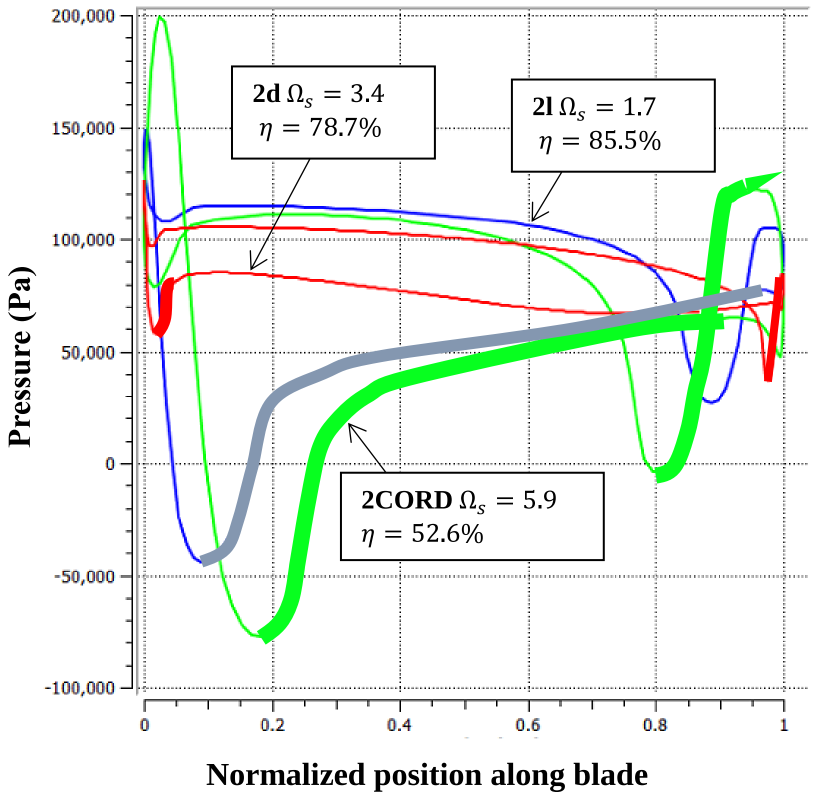

Figure 3.20. Blade loading diagrams for Speed Study case 2: Span 50%

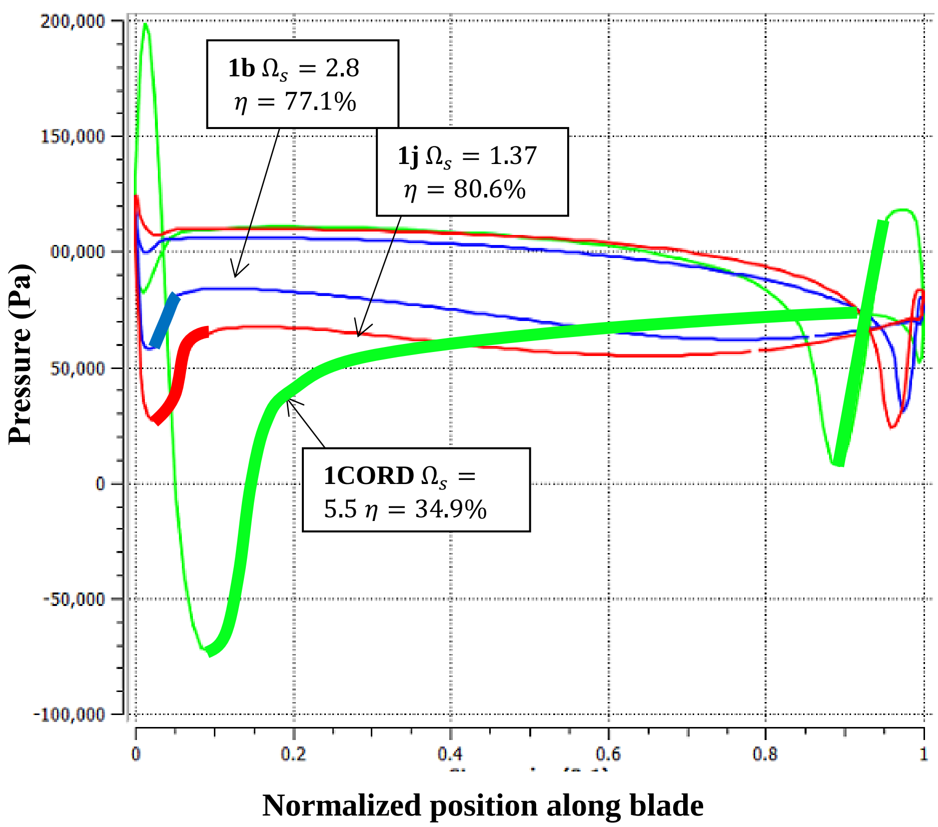

Figure 3.21. Blade loading diagrams for Speed Study case 1: Span 50%

Static pressure contours were produced for each design simulated, which display areas of increased pressure at the leading edge pressure side, decreased pressure at the leading edge on the suction side, and decreased pressure at the trailing edge pressure side. These figures illustrate that for the higher speed designs, the pressure gradients are of larger magnitude at each of these areas. This effect was observed for each case simulated in the Speed Study. Static pressure contours are shown for case 3 (Figure 3.22), case 1 (Figure 3.23), and case 3 (Figure 3.24)

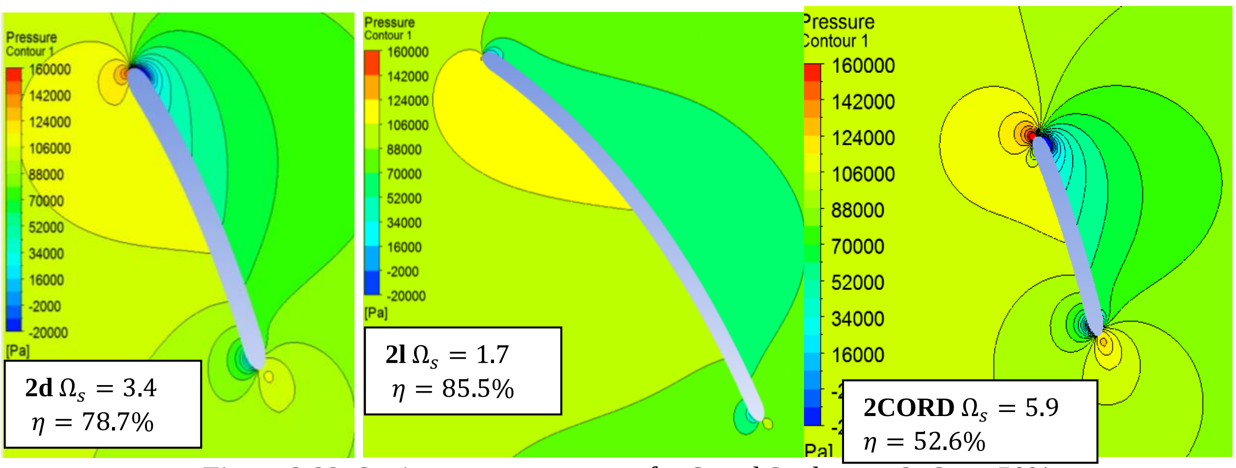

Figure 3.22. Static pressure contours for Speed Study case 2: Span 50%

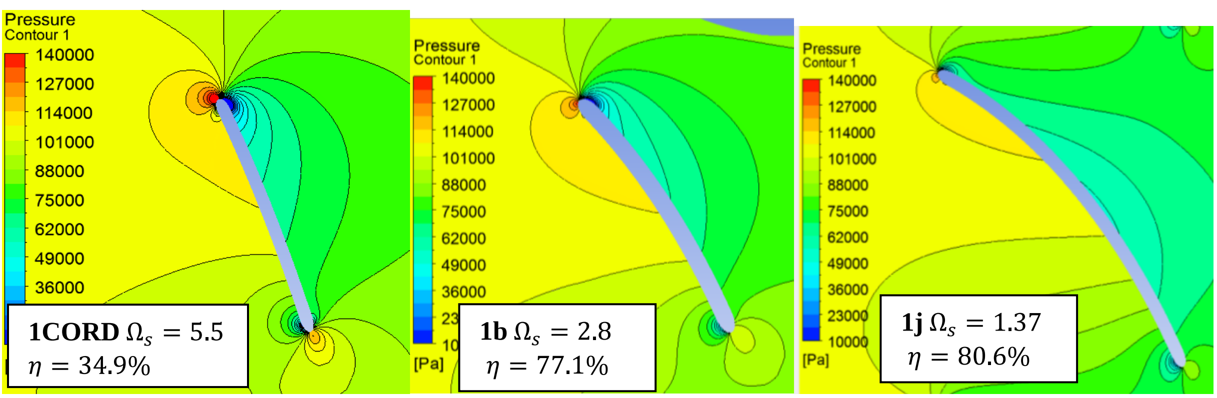

Figure 3.23. Static pressure contours for Speed Study case 1: Span 50%

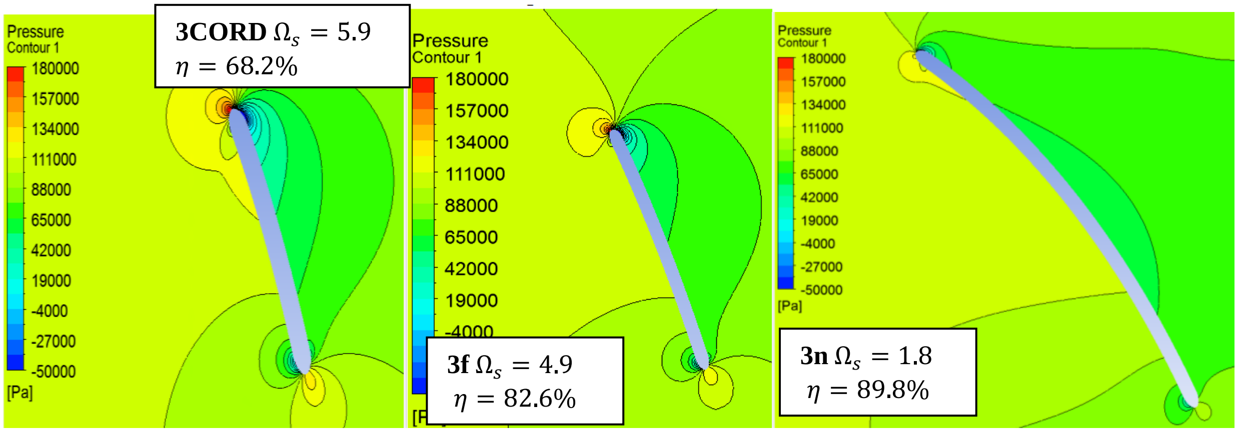

Figure 3.24. Static pressure contours for Speed Study case 3: Span 50%

Figure 3.25 and 3.27 below shows velocity triangles for two designs within the Speed Study, designs 1cord and 1j respectively, superimposed onto relative velocity vector contours. These figures illustrate how the relative velocities were higher for the designs with the Cordier recommended speeds.

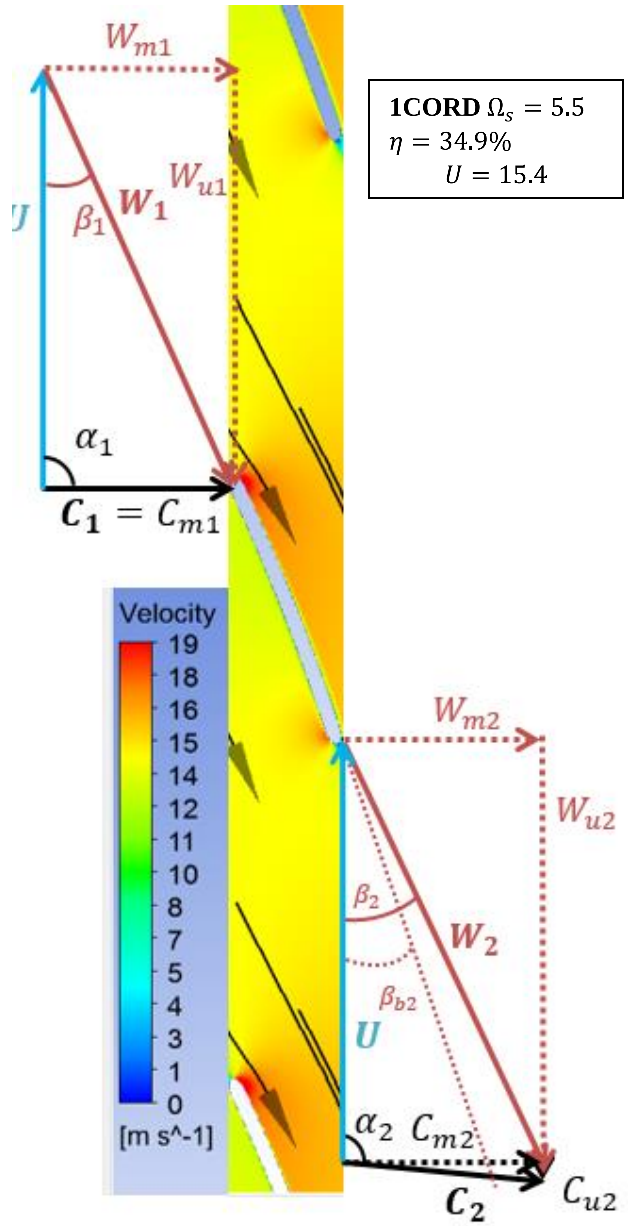

Figure 3.25. Velocity triangles with relative velocity contours for design 1CORD of the Speed Study: (Span 50%)

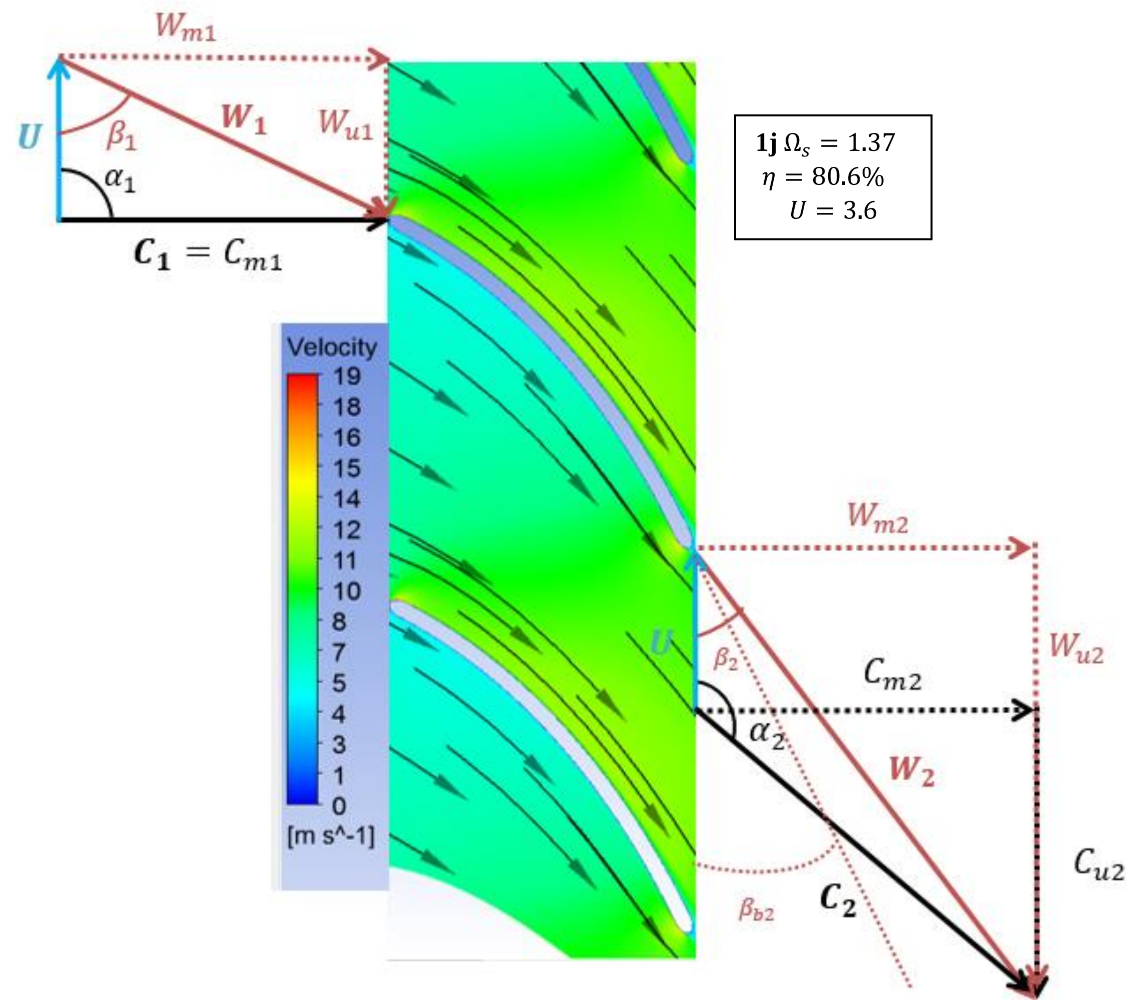

Figure 3.26. Velocity triangles with relative velocity contours for design 1j of the Speed Study: (Span 50%)

3.3.5. Hub and Shroud Effects

Decreased flow velocity was recorded near the hub and shroud surfaces for each design simulated. The higher speed designs saw relative velocity decrease the most near the hub and shroud. This effect was observed across each case in the Speed Study. Figure 3.27 shows the relative flow velocity W over the blade span at the trailing edge for four designs in case 2 of the Speed Study, and Figure 3.28 shows this for four designs within case 1.

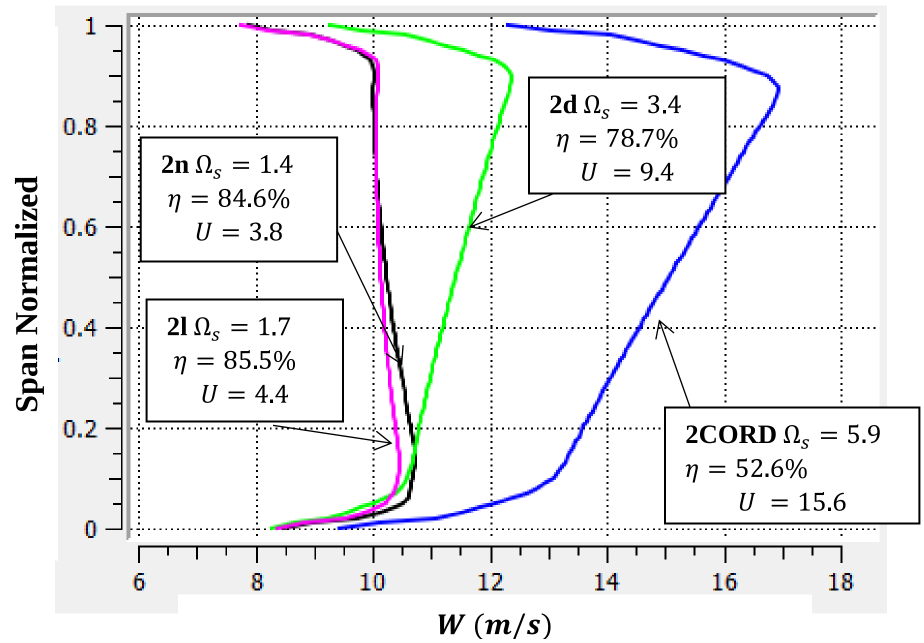

Figure 3.27. Relative velocity of Case 2 Speed Study designs at the trailing edge along span

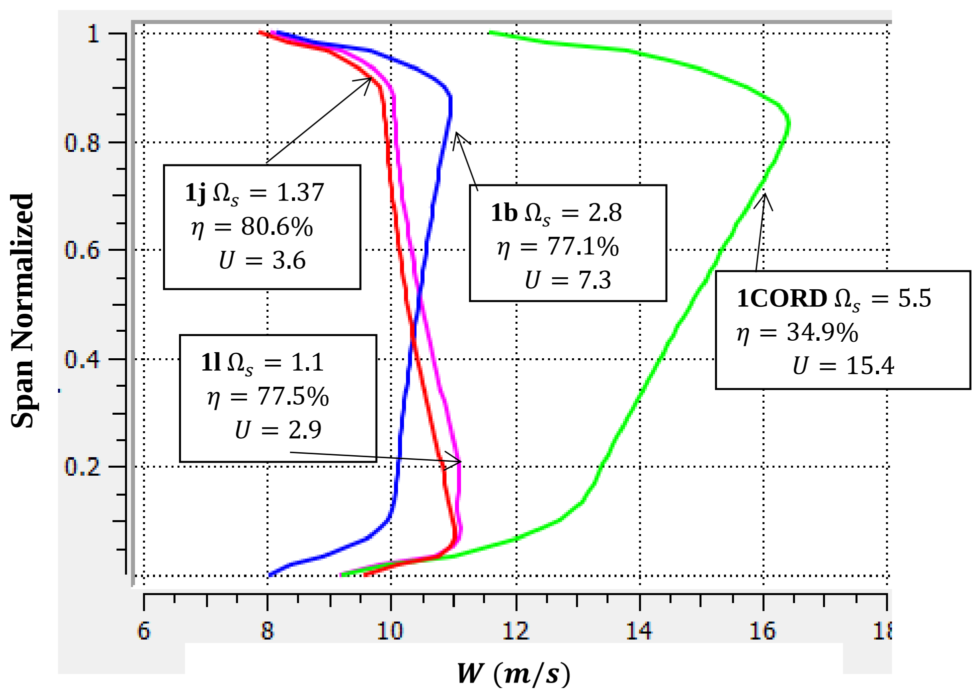

Figure 3.28. Relative velocity of Case 1 Speed Study designs at the trailing edge along span

Figure 3.29 and Figure 3.30 display relative flow velocity for the designs at which highest efficiency was recorded in the Speed Study along the span of the blades, near the leading and trailing edges respectively. Decreased flow velocity close to the hub and shroud was recorded for each design simulated.

The designs with higher head (cases 4,5,6) exhibited flows with increased relative velocity compared to those with lower head (cases 1,2,3). The designs with the smallest diameter experienced the most flow deceleration near the hub and shroud at the trailing edge, these are designs in cases 1 and 4. It can be observed that lower velocity was recorded over a larger portion of the span at the trailing edge for the simulations of the designs with lower diameter, thus the boundary layer size was larger for the smaller diameter designs. The simulations of the designs with lower diameter predicted lower efficiency; this could be attributed in part to additional friction losses at the hub and shroud. Losses in the boundary layer are higher for turbine designs with increased surface area of the blades, as well as the hub and shroud surfaces relative to the volume of the fluid region.

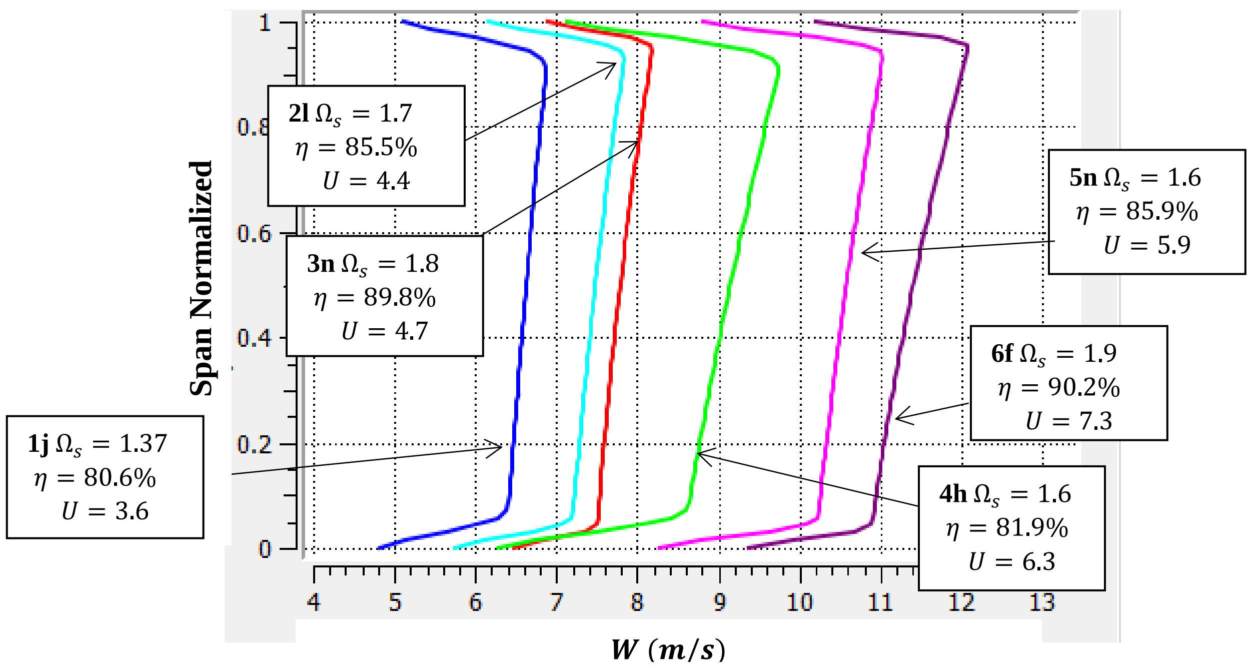

Figure 3.29. Relative velocity of highest efficiency Speed Study designs at the leading edge along span

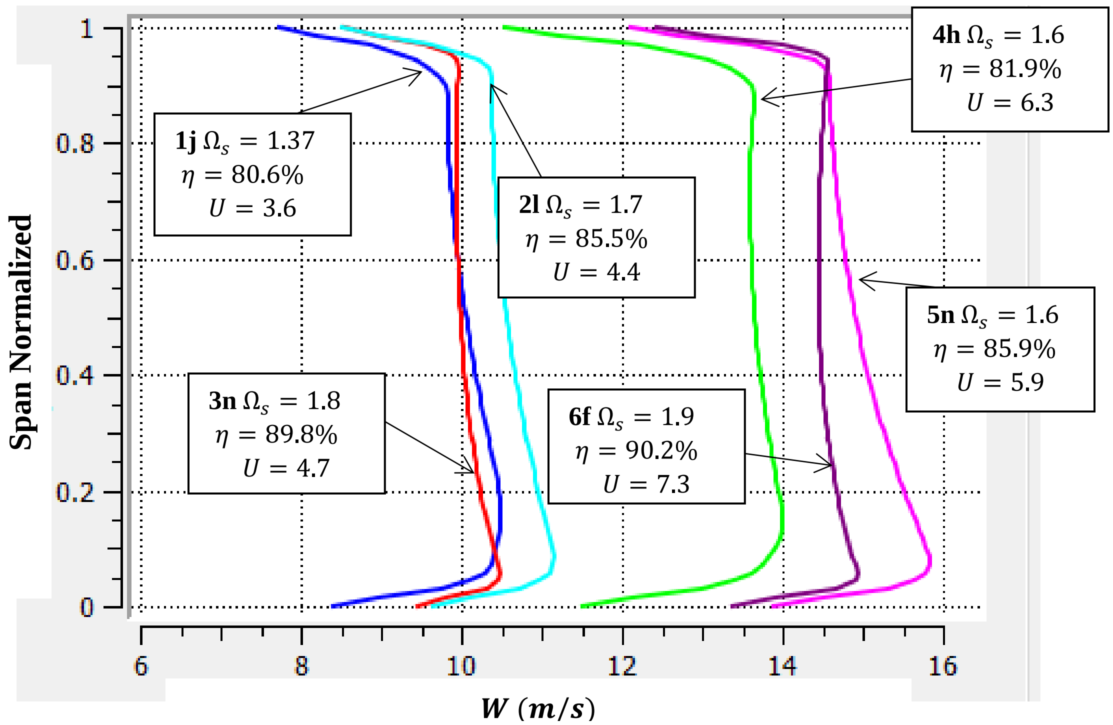

Figure 3.30. Relative velocity of highest efficiency Speed Study designs at the trailing edge along span

Below Figure 3.31 shows the turbulence kinetic energy k at the trailing edge for the highest efficiency designs in the Speed Study. Turbulence kinetic energy of the flow was higher near the hub and shroud for the designs with higher head, and the designs with lower diameter (cases 1 and 4) showed the more turbulent region of the flow takes up a larger portion of the blade span. This could be attributed to additional friction losses at the hub and shroud in the designs with smaller diameter.

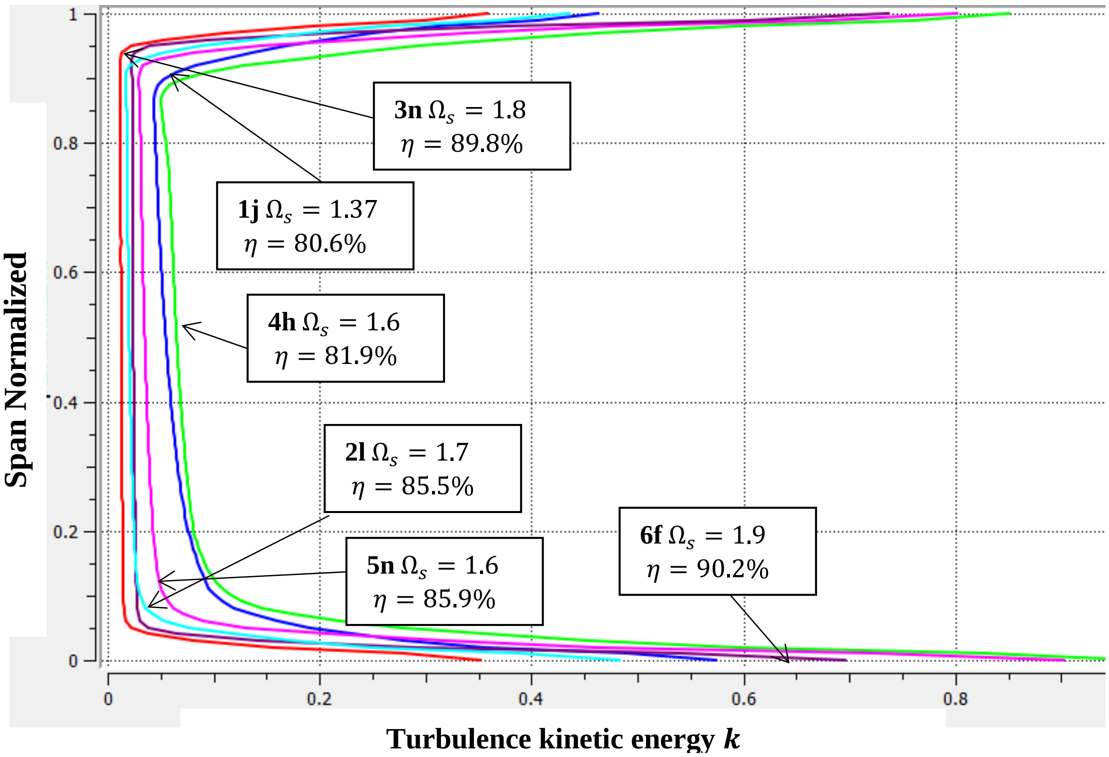

Figure 3.31. Turbulence kinetic energy of highest efficiency Speed Study designs at the trailing edge along span

3.3.6. Work Extraction

The simulations of each design predicted reduced work extraction near the hub and shroud. This is illustrated in the figures below, which display absolute circumferential flow velocity over the span of the blades at the trailing edge. Figure 3.32 shows absolute circumferential flow velocity for three designs in case 2 of the Speed Study, Figure 3.33 shows this for case 3. Designs which used the Cordier-recommended speed exhibited simulated flows with the largest decrease of circumferential flow velocity near the hub and shroud. This effect was observed for each case simulated in the Speed Study.

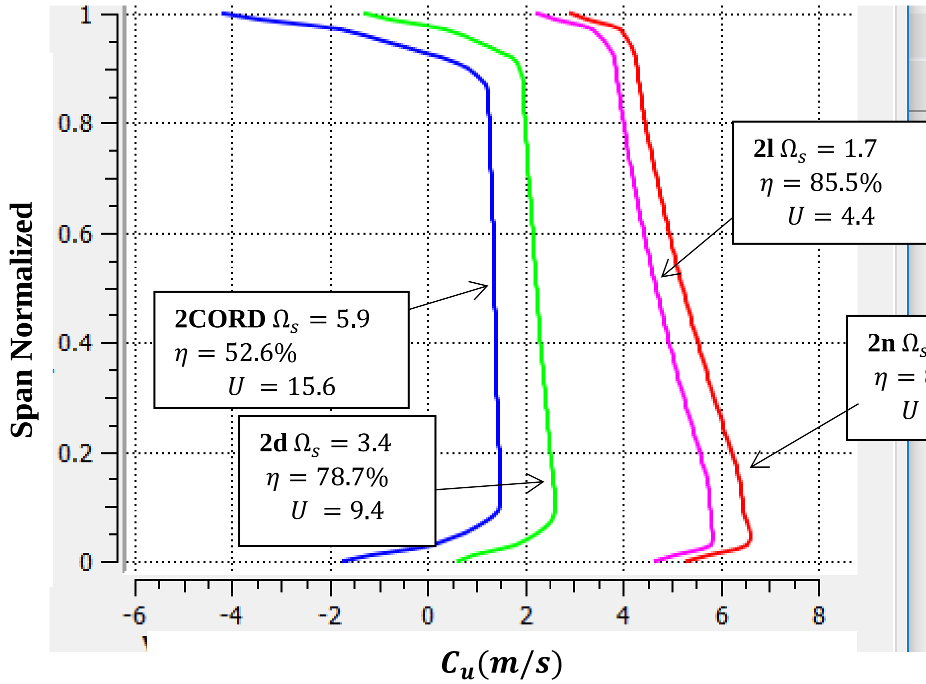

Figure 3.32. Absolute circumferential flow velocity for designs in case 2 of Speed Study at the trailing edge along span

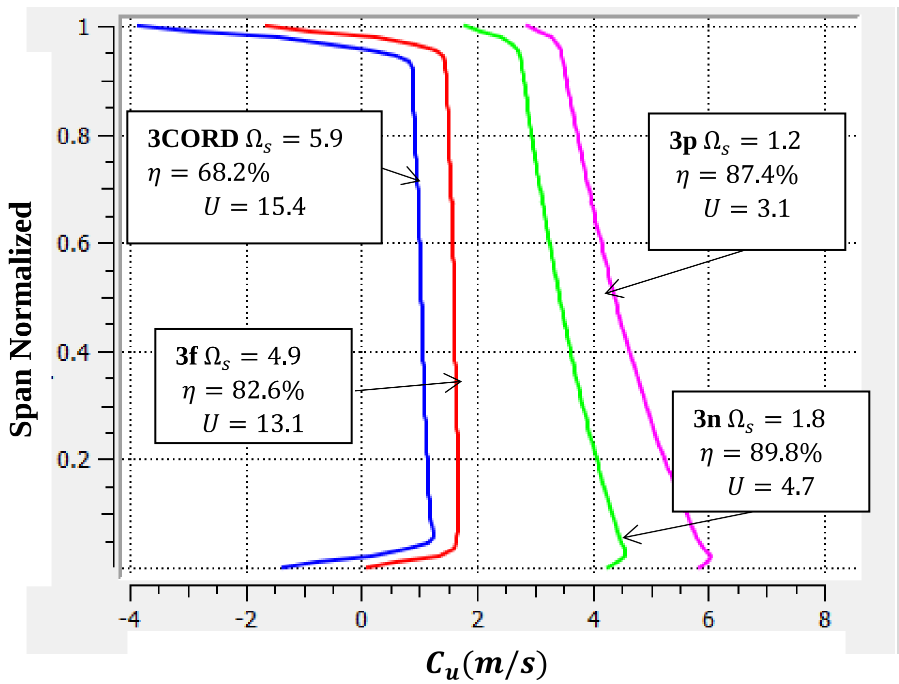

Figure 3.33. Absolute Circumferential flow velocity for designs in Case 3 of Speed Study at the trailing edge along span

For each design, C_u reached a maximum near the trailing edge, and between the trailing edge and the exit the flow decelerates, and C_u decreases. Figure 3.34 below shows average C_u from annulus inlet to outlet for three designs within case 1 of the Speed Study.

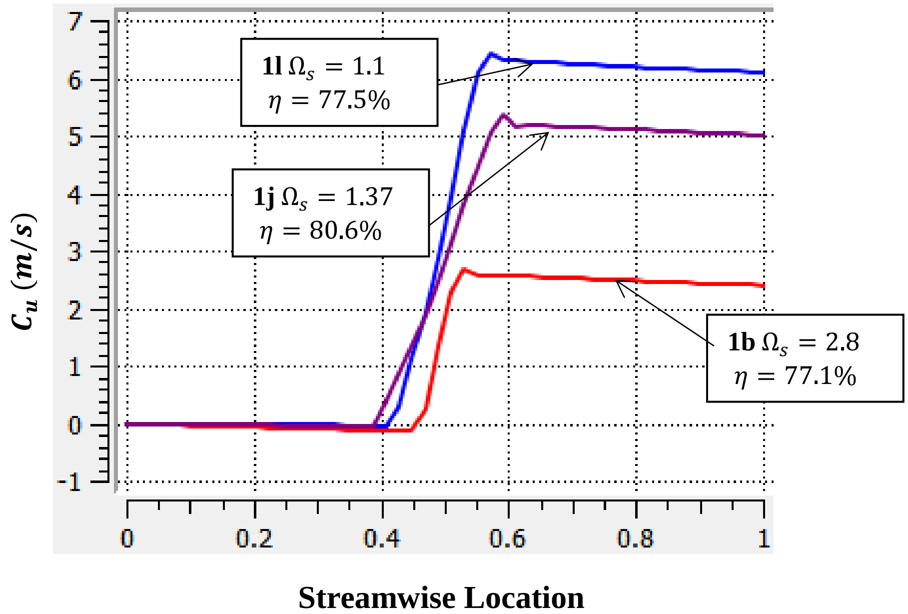

Figure 3.34. Average absolute circumferential flow velocity from inlet to outlet for designs case 1 of Speed Study

Figure 3.35 below shows the absolute circumferential flow velocity for the designs with the highest predicted efficiency in the Speed Study along the blade span at the trailing edge. C_u was higher near the hub than the shroud, this is because the relative flow angles were designed to have an equal value of $U_\theta C_{ui}$ across the span.

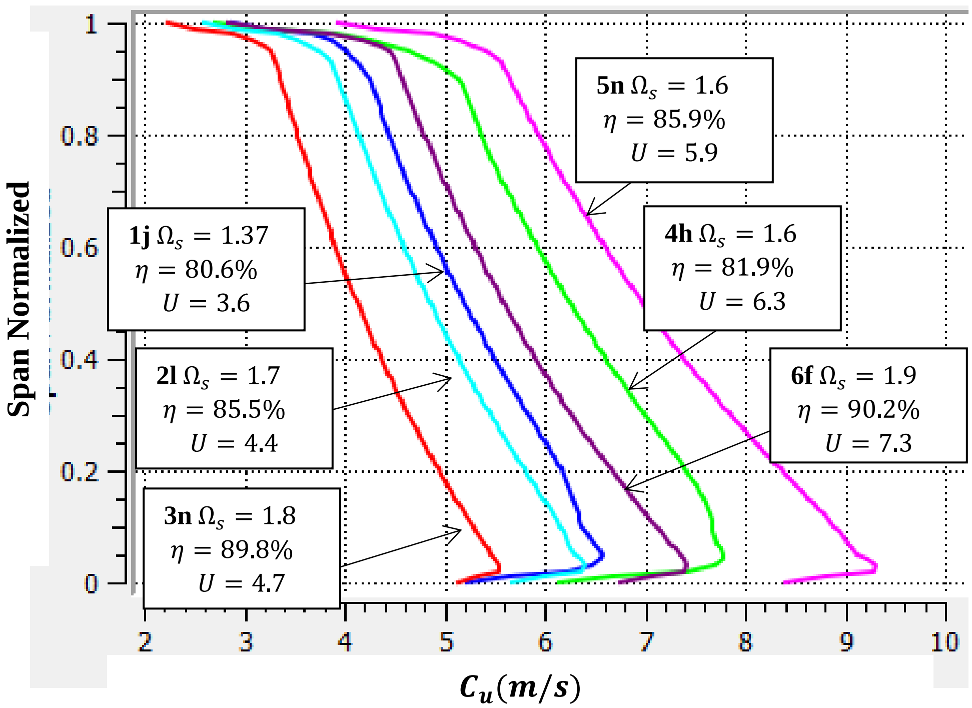

Figure 3.35. Absolute circumferential flow velocity for highest efficiency designs in Speed Study at the trailing edge along span

3.3.7. Cavitation

It is important to track how low static pressure reaches when evaluating the performance of a hydraulic turbine design in CFD. If there are any areas where pressure reaches below the vapor pressure of water in simulation, cavitation could occur in a real-life application. Contour diagrams were produced for each design, recording areas where static pressure was close to or below the vapor pressure of water. Figure 3.36 shows the low static pressure contour for case 1, Figure 3.37 for case 2, Figure 3.38 for case 3, Figure 3.39 for case 4, Figure 3.40 for case 5, and Figure 3.41 for case 6. The figures show the simulations of designs at higher speeds exhibited flows with lower pressure at the leading edge on the suction side of the blades, and have added risk of experiencing cavitation.

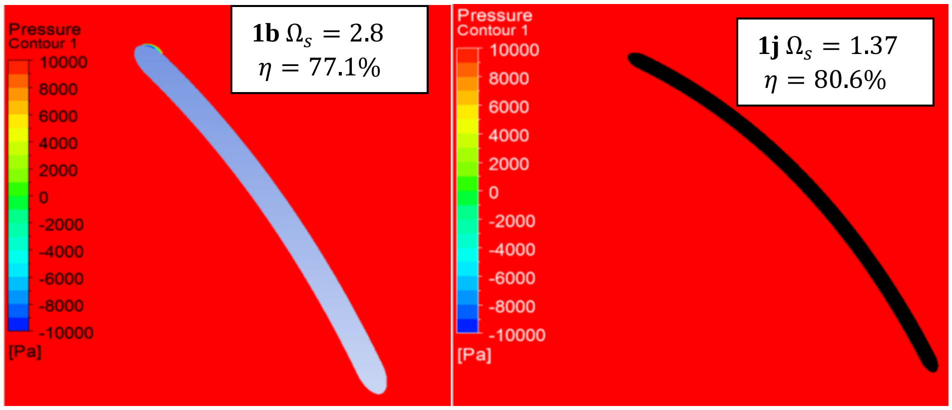

Figure 3.36. Areas of low static pressure for case 1 of Speed Study: 50% Span

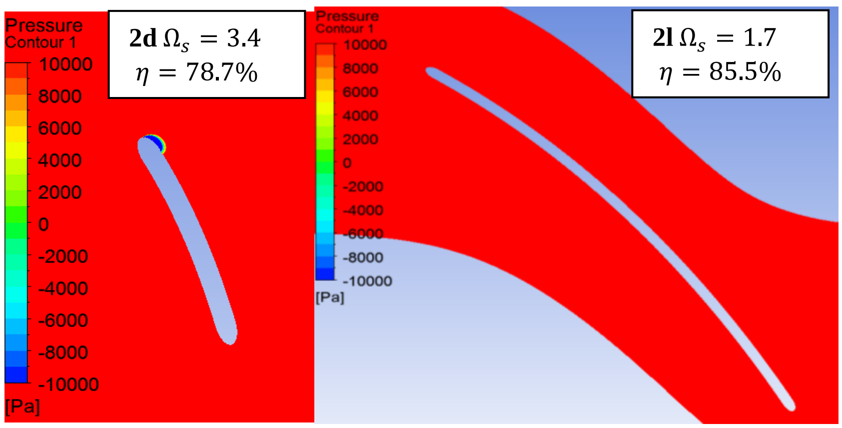

Figure 3.37. Areas of low static pressure for case 2 of Speed Study: 50% Span

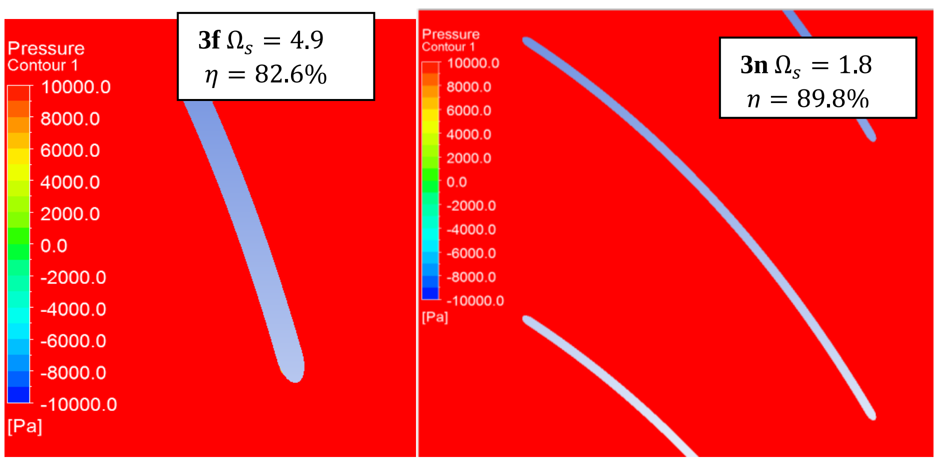

Figure 3.38. Areas of low static pressure for case 3 of Speed Study: 50% Span

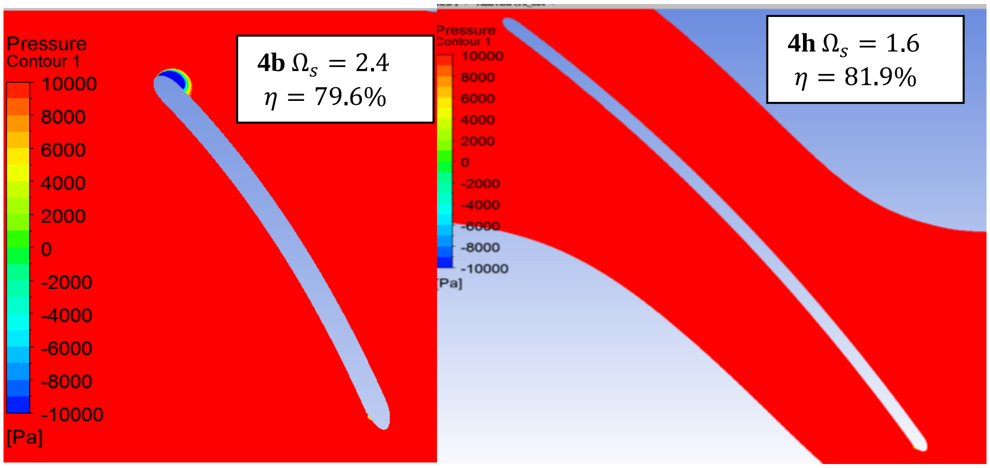

Figure 3.39. Areas of low static pressure for case 4 of Speed Study: 50% Span

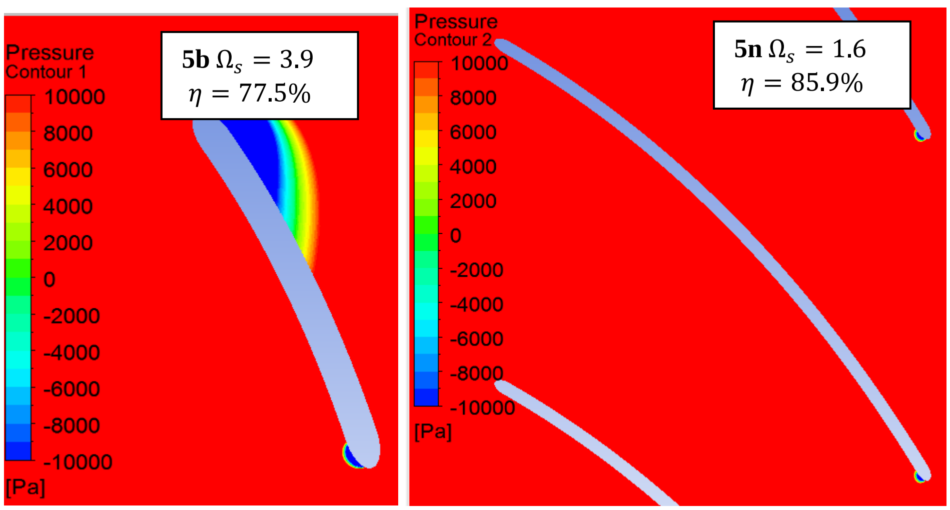

Figure 3.40. Areas of low static pressure for case 5 of Speed Study: 50% Span

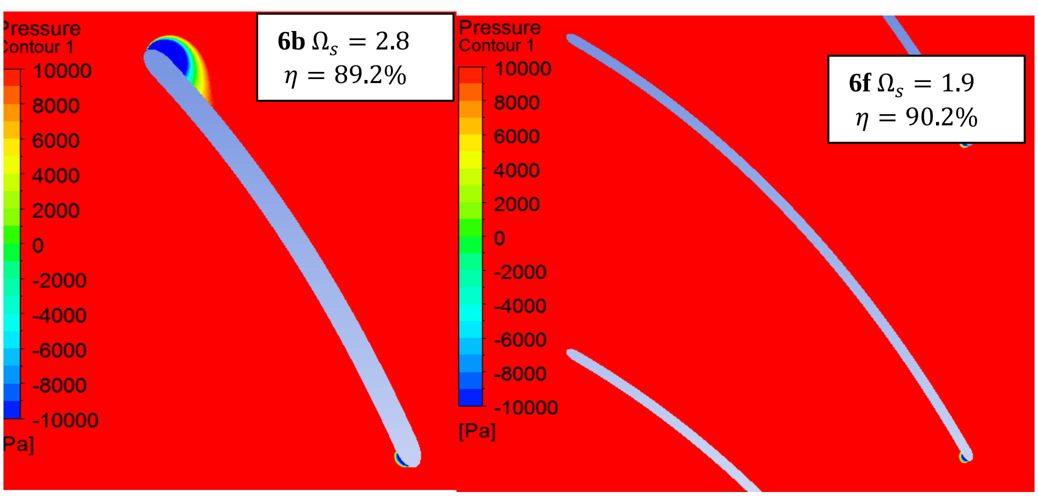

Figure 3.41. Areas of low static pressure for case 6 of Speed Study: 50% Span

3.4. Second Study: Blade Length Study

The Blade Length Study consisted of simulations of designs with varying axial blade lengths at the rotational speeds at which highest efficiency was measured in the Speed Study. Different axial blade lengths will result in different values of Zweifel coefficient. The below tables show how varying Zweifel coefficient effected isentropic efficiency and trailing edge flow deviation.

Table 3.8. Case 1 Blade Length Study Results

<table>
<tr><td rowspan="9">Case 1 - 1j
$H = 1.86$ m
$\dot{V} = 0.46\frac{m^3}{s}$
$r_h = .12$ m
$r_s = .2$ m</td><td>Case</td><td>Run</td><td>U (m/s)</td><td>$\tilde{e}(\frac{m^2}{s^2})$</td><td>$b$ (m)</td><td>Efficiency η</td><td>RPM</td><td>Trailing edge deviation δ' (deg)</td><td>Z</td><td>$\dot{W}$ (kW)</td></tr>
<tr><td>1j</td><td>1</td><td>3.56</td><td>14.45</td><td>0.162</td><td>78.40</td><td>170</td><td>7.42</td><td>0.48</td><td>6.65</td></tr>
<tr><td>1j</td><td>2</td><td>3.56</td><td>14.69</td><td>0.122</td><td>79.04</td><td>170</td><td>8.94</td><td>0.63</td><td>6.76</td></tr>
<tr><td>1j</td><td>3</td><td>3.56</td><td>14.51</td><td>0.090</td><td>79.72</td><td>170</td><td>11.86</td><td>0.85</td><td>6.68</td></tr>
<tr><td>1j</td><td>4</td><td>3.56</td><td>14.64</td><td>0.070</td><td>79.70</td><td>170</td><td>15.35</td><td>1.09</td><td>6.73</td></tr>
<tr><td>1j</td><td>5</td><td>3.56</td><td>14.34</td><td>0.050</td><td>78.21</td><td>170</td><td>19.68</td><td>1.49</td><td>6.59</td></tr>
<tr><td>1j</td><td>6</td><td>3.56</td><td>14.13</td><td>0.190</td><td>77.43</td><td>170</td><td>5.94</td><td>0.41</td><td>6.50</td></tr>
<tr><td>1j</td><td>7</td><td>3.56</td><td>14.83</td><td>0.080</td><td>80.06</td><td>170</td><td>13.03</td><td>0.96</td><td>6.82</td></tr>
<tr><td>1j</td><td>8</td><td>3.56</td><td>14.78</td><td>0.096</td><td>79.96</td><td>170</td><td>10.85</td><td>0.80</td><td>6.80</td></tr>
</table>

Table 3.9. Case 2 Blade Length Study Results

<table>
<tr><td rowspan="9">Case 2 - 2l
$H = 1.85$ m
$\dot{V} = 1.050\frac{m^3}{s}$
$r_h = .2$ m
$r_s = .3$ m</td><td>Case</td><td>Run</td><td>U (m/s)</td><td>$\tilde{e}(\frac{m^2}{s^2})$</td><td>$b$ (m)</td><td>Efficiency η</td><td>RPM</td><td>Trailing edge deviation δ' (deg)</td><td>Z</td><td>$\dot{W}$ (kW)</td></tr>
<tr><td>2l</td><td>1</td><td>4.40</td><td>15.35</td><td>0.24</td><td>82.86</td><td>140</td><td>5.71</td><td>0.42</td><td>16.12</td></tr>
<tr><td>2l</td><td>2</td><td>4.40</td><td>15.59</td><td>0.19</td><td>83.79</td><td>140</td><td>7.15</td><td>0.53</td><td>16.37</td></tr>
<tr><td>2l</td><td>3</td><td>4.40</td><td>15.80</td><td>0.15</td><td>84.65</td><td>140</td><td>8.99</td><td>0.67</td><td>16.59</td></tr>
<tr><td>2l</td><td>4</td><td>4.40</td><td>15.83</td><td>0.11</td><td>85.25</td><td>140</td><td>12.61</td><td>0.91</td><td>16.62</td></tr>
<tr><td>2l</td><td>5</td><td>4.40</td><td>15.70</td><td>0.08</td><td>84.88</td><td>140</td><td>17.10</td><td>1.24</td><td>16.48</td></tr>
<tr><td>2l</td><td>6</td><td>4.40</td><td>16.02</td><td>0.10</td><td>85.47</td><td>140</td><td>14.57</td><td>1.05</td><td>16.82</td></tr>
<tr><td>2l</td><td>7</td><td>4.40</td><td>15.96</td><td>0.13</td><td>85.14</td><td>140</td><td>10.34</td><td>0.78</td><td>16.76</td></tr>
<tr><td>2l</td><td>8</td><td>4.40</td><td>15.79</td><td>0.12</td><td>85.52</td><td>140</td><td>10.63</td><td>0.84</td><td>16.58</td></tr>
</table>

Table 3.10. Case 3 Blade Length Study Results

Case 3 - 3n	Case	Run	U (m/s)	$\tilde{e}(\frac{m^2}{s^2})$	b (m)	Efficiency η	RPM	Trailing edge deviation δ' (deg)	Z	$\dot{W}$ (kW)
$H = 1.9$ m $\dot{V} = 2.85\frac{m^3}{s}$ $r_h = .3$ m $r_s = .5$ m	3n	1	4.71	16.33	0.40	86.79	90	5.27	0.40	46.54
	3n	2	4.71	16.33	0.35	86.76	90	6.41	0.46	46.55
	3n	3	4.71	16.64	0.30	88.11	90	6.74	0.53	47.44
	3n	4	4.71	16.61	0.25	88.57	90	8.10	0.64	47.35
	3n	5	4.71	16.58	0.20	89.30	90	10.05	0.79	47.26
	3n	6	4.71	16.84	0.15	89.77	90	13.79	1.05	47.99
	3n	7	4.71	16.78	0.13	89.71	90	15.99	1.20	47.81
	3n	8	4.71	18.01	0.11	87.58	90	19.99	1.42	51.33
	3n	9	4.71	16.75	0.18	89.94	90	11.41	0.90	47.73

Table 3.11. Case 4 Blade Length Study Results

Case 4 - 4h	Case	Run	U (m/s)	$\tilde{e}(\frac{m^2}{s^2})$	b (m)	Efficiency η	RPM	Trailing edge deviation δ' (deg)	Z	$\dot{W}$ (kW)
$H = 3.69$ m $\dot{V} = 0.6\,\frac{m^3}{s}$ $r_h = .12$ m $r_s = .2$ m	4h	1	6.28	29.11	0.16	79.40	300	5.45	0.40	17.47
	4h	2	6.28	29.33	0.14	80.17	300	6.25	0.46	17.60
	4h	3	6.28	29.06	0.18	79.02	300	4.99	0.36	17.44
	4h	4	6.28	29.73	0.11	81.15	300	7.76	0.58	17.84
	4h	5	6.28	30.04	0.08	81.86	300	10.77	0.80	18.02
	4h	6	6.28	29.60	0.06	81.99	300	14.63	1.06	17.76
	4h	7	6.28	30.14	0.09	81.69	300	9.52	0.71	18.08
	4h	8	6.28	30.14	0.05	81.77	300	15.88	1.26	18.08
	4h	9	6.28	30.05	0.07	82.01	300	12.54	0.91	18.03

Table 3.12. Case 5 Blade Length Study Results

Case 5 – 5n $H = 3.73$ m $\dot{V} = 1.5\frac{m^3}{s}$	Case	Run	U (m/s)	$\tilde{e}(\frac{m^2}{s^2})$	b (m)	Efficiency η	RPM	Trailing edge deviation δ' (deg)	Z	$\dot{W}$ (kW)
$r_h = .2$ m	5n	1	5.97	30.85	0.24	83.68	190	6.08	0.44	46.27
$r_s = .3$ m	5n	2	5.97	30.48	0.27	83.03	190	5.45	0.39	45.72
	5n	3	5.97	31.07	0.20	84.38	190	7.16	0.52	46.60
	5n	4	5.97	31.05	0.16	84.93	190	8.80	0.65	46.58
	5n	5	5.97	31.41	0.12	85.77	190	11.45	0.87	47.12
	5n	6	5.97	31.48	0.10	86.04	190	13.89	1.03	47.22
	5n	7	5.97	31.40	0.08	85.57	190	17.90	1.28	47.11
	5n	8	5.97	31.55	0.11	85.86	190	12.61	0.94	47.32
	5n	9	5.97	31.49	0.11	85.97	190	10.66	0.80	47.23

Table 3.13. Case 6 Blade Length Study Results

Case 6 - 6h $H = 3.78$ m	Case	Run	U (m/s)	$\tilde{e}(\frac{m^2}{s^2})$	b (m)	Efficiency η	RPM	Trailing edge deviation δ' (deg)	Z	$\dot{W}$ (kW)
$\dot{V} = 4.1\frac{m^3}{s}$	6h	1	5.76	32.47	0.40	87.06	110	5.97	0.44	133.14
$r_h = .3$ m	6h	2	5.76	32.39	0.44	86.72	110	5.52	0.41	132.78
$r_s = .5$ m	6h	3	5.76	32.22	0.47	86.36	110	5.21	0.38	132.10
	6h	4	5.76	31.98	0.50	85.97	110	4.93	0.36	131.13
	6h	5	5.76	32.44	0.37	87.26	110	6.40	0.48	132.99
	6h	6	5.76	32.68	0.33	87.92	110	7.07	0.54	134.00
	6h	7	5.76	32.97	0.29	88.21	110	8.05	0.61	135.17
	6h	8	5.76	33.10	0.25	88.76	110	9.22	0.70	135.73
	6h	9	5.76	33.24	0.21	89.20	110	10.78	0.83	136.30
	6h	10	5.76	33.52	0.16	89.58	110	14.19	1.08	137.45
	6h	11	5.76	32.98	0.13	89.02	110	17.37	1.31	135.23
	6h	12	5.76	33.36	0.20	89.81	110	10.97	0.90	136.78

3.5. Blade Length Study Results Discussion

3.5.1. Overall Summary

For designs with long blade lengths Zweifel coefficient is small. These designs demonstrated lower efficiency in the CFD simulations than those with shorter blade lengths. Dixon suggested this is due to increased friction losses [4]. The below Figure 3.42 shows efficiency obtained at differing values of Zweifel coefficient for the simulations conducted as a part of the Blade Length Study. At Zwefiel coefficients between 0.8 and 1.1 efficiency was highest in simulations, and stayed relatively constant across designs in that range. At Zwefiel coefficients below 0.8 predicted efficiency was lower as friction losses increased. Designs with Zweifel coefficients above 1.1 experienced decreased efficiency in simulations.

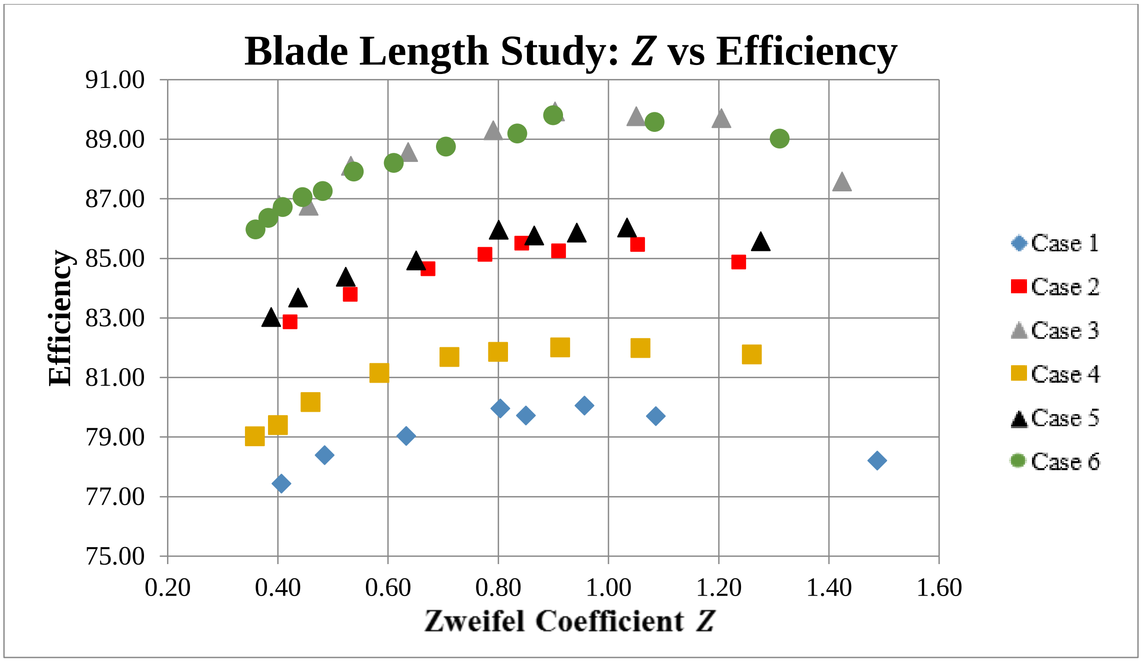

Figure 3.42. Zweifel coefficient vs. Efficiency for Blade Length Study

Flow does not follow the blade shape perfectly, and as blades are made shorter axially the blades must be made with sharper turning to obtain the same change in absolute circumferential flow speed and energy extraction. As the blade length was decreased and Zweifel coefficient increased, the trailing edge flow deviation δ' increased. In the Blade Length Study, a correlation between the Zweifel coefficient and trailing edge flow deviation was observed, this is shown below in Figure 3.43.

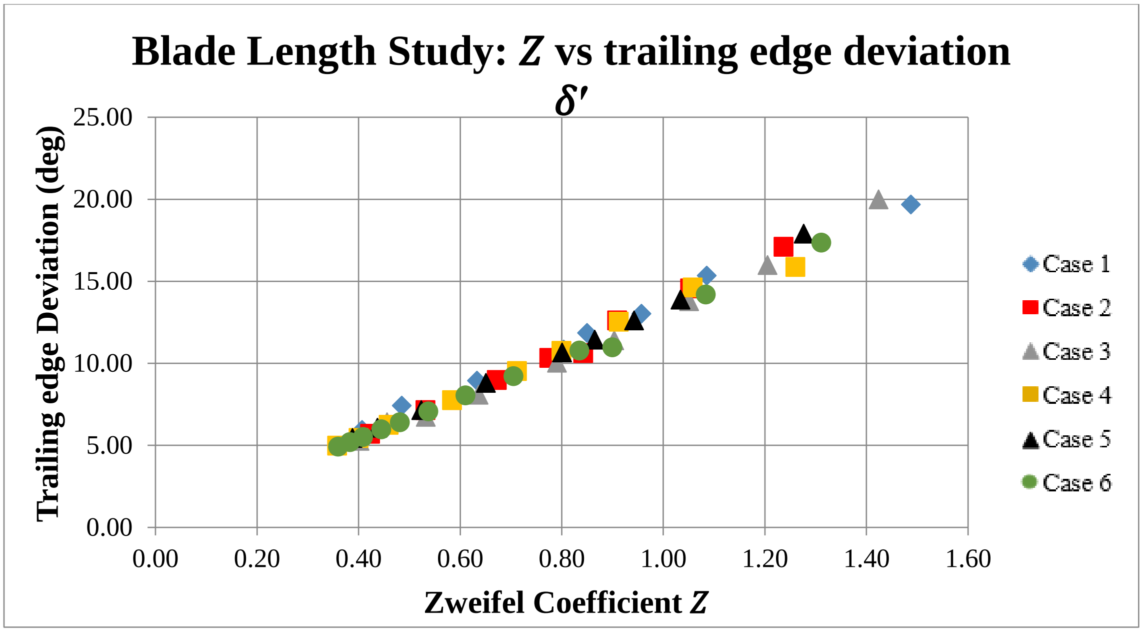

Figure 3.43. Zweifel Coefficient vs. Flow deviation at trailing edge for Blade Length Study

For the Blade Length Study simulations of turbines with both long axial blade lengths and short blade lengths were conducted, and it was observed that efficiency was highest for the simulations of designs with Zweifel coefficients between .8 and 1.1. With Zweifel coefficients below 0.8, efficiency decreased. This trend is illustrated in Figure 3.44, where the difference of the peak efficiency measured in the Speed Study and efficiency of the design simulated is shown vs. the Zweifel Coefficient for each case.

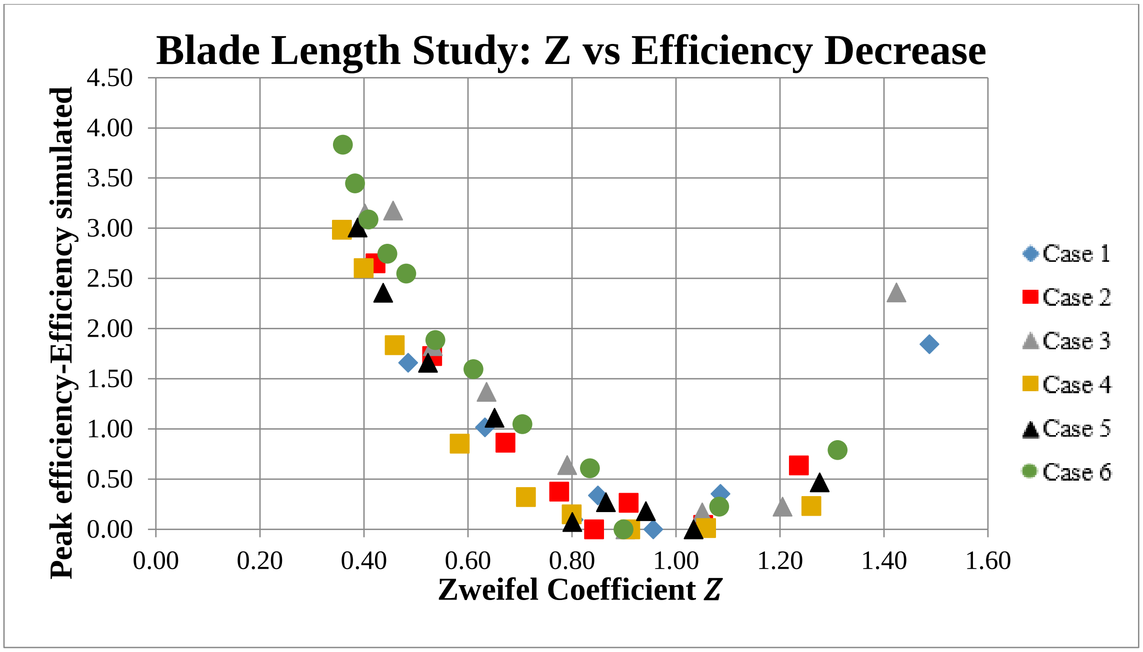

Figure 3.44. Difference of the peak efficiency and efficiency of the design vs. the Zweifel coefficient

The decrease in predicted efficiency resulting from extending the blades longer than aerodynamically necessary can be considered modest, designs with Zweifel Coefficients near .6(±.05) predicted a decrease in efficiency no larger than 1.7% compared to the peak efficiency point. Designs with a Zweifel coefficient near .5(±.05) exhibited a maximum efficiency decrease of 2.5% compared to the peak efficiency point. Blades for water turbines experience high loads, and blades for water turbines often require large blade chords as longer blades can demonstrate improved structural performance, as distributing the force over a larger area decreases stresses on the blades [4]. Structural simulations were not done as a part of this study, however if FEA analysis suggested the designs with higher Zweifel coefficients would fail, longer blades could be employed to improve strength.

3.5.2. Flow Visualization and Vectors

The relative velocity vector diagrams shown in the below figures at span 50%, show there are two areas where velocity gradients were had the highest magnitude, at the suction side leading edge, and on the pressure side at the trailing edge. These large changes in flow velocity over short distances can lead to shear stresses and losses [35]. A wake was observed after the blade trailing edge where velocity is lower. The designs which had higher Zweifel coefficient had greater magnitude velocity gradients at the leading and trailing edges, and a larger wake size. Relative velocity vector contours were produced for each design in the Blade Length Study, Figure 3.45 shows relative velocity contours with vectors for case 1, Figure 3.46 for case 2, Figure 3.47 for case 3, Figure 3.48 for case 4, Figure 3.39 for case 5, and Figure 3.40 for case 6.

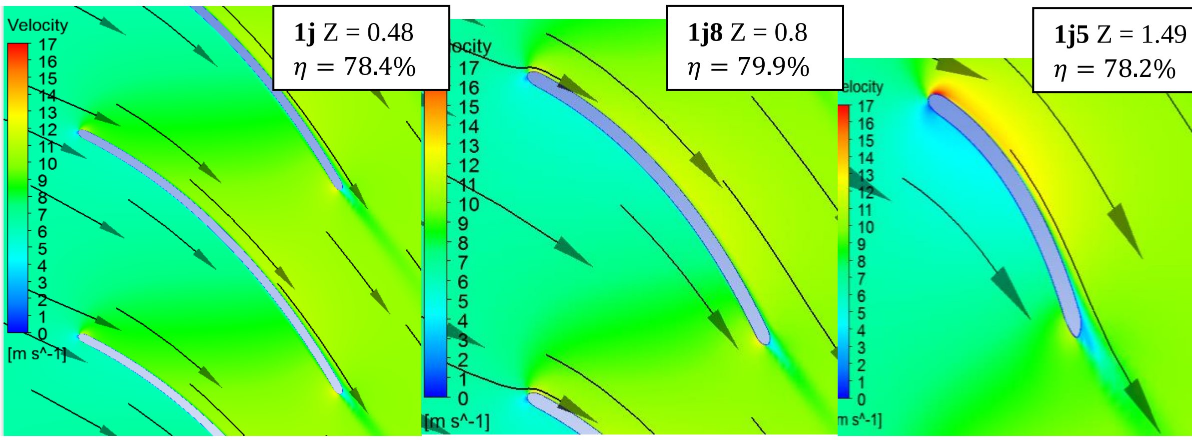

Figure 3.45. Relative velocity vectors for case 1 of Blade Length Study: Span 50%

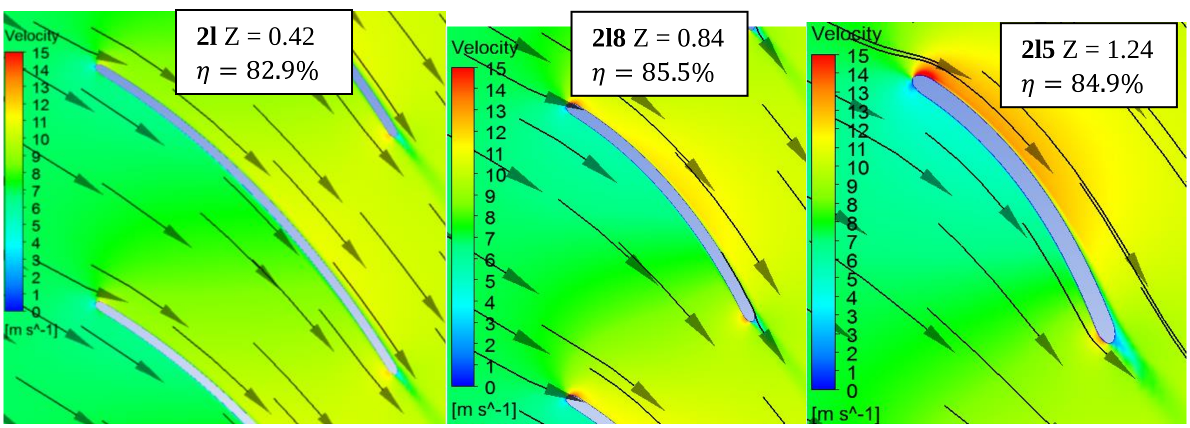

Figure 3.46. Relative velocity vectors for case 2 of Blade Length Study: Span 50%

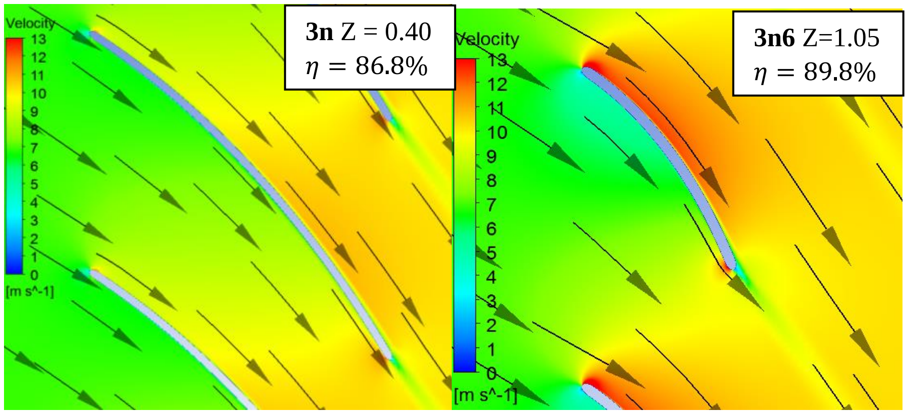

Figure 3.47. Relative velocity vectors for case 3 of Blade Length Study: Span 50%

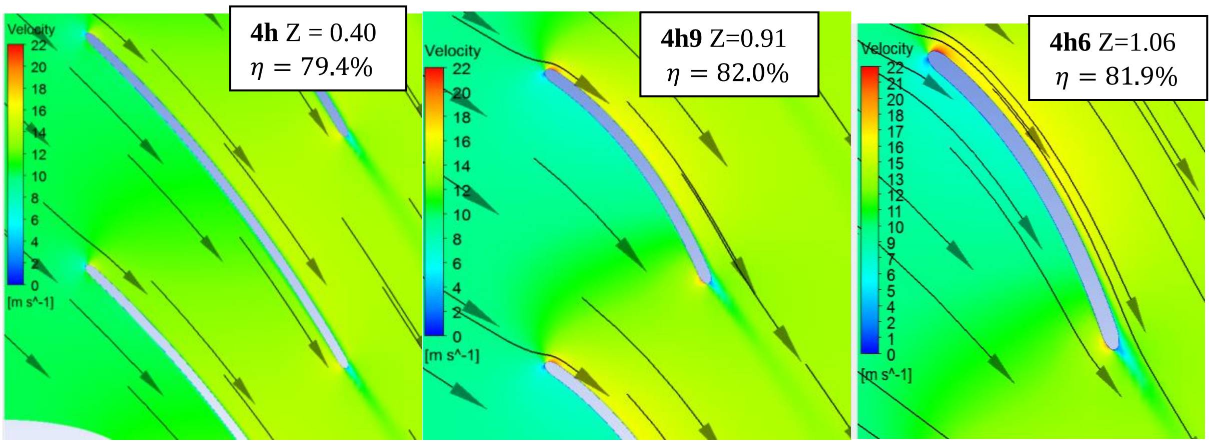

Figure 3.48. Relative velocity vectors for case 4 of Blade Length Study: Span 50%

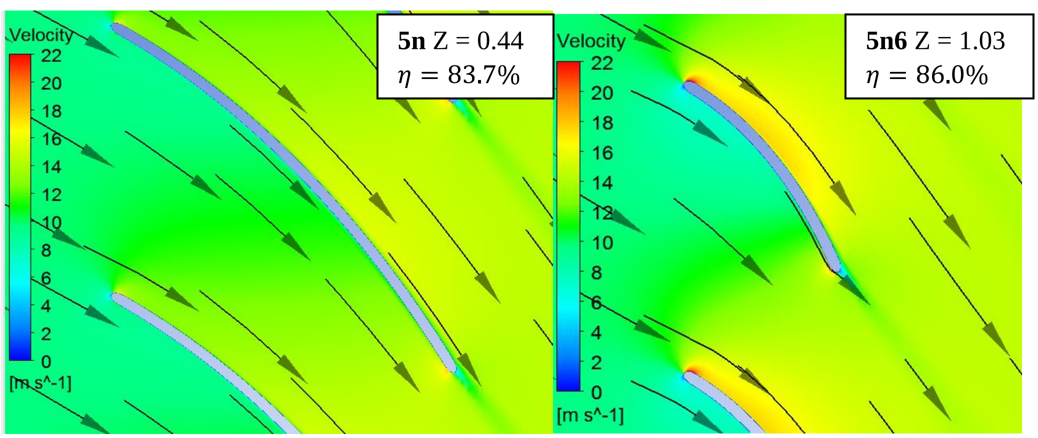

Figure 3.39. Relative velocity vectors for case 5 of Blade Length Study: Span 50%

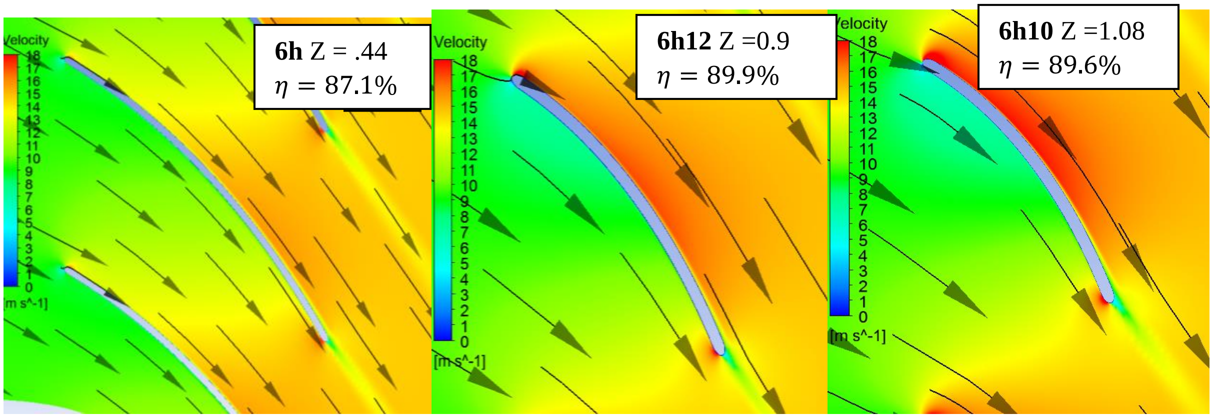

Figure 3.40. Relative velocity vectors for case 6 of Blade Length Study: Span 50%

For any turbine the flow velocity is lower on the pressure side, and the velocity is higher on the suction side. For the designs with shorter blades, the simulated flow accelerated over a shorter distance. For the designs with larger Zweifel coefficients simulated in the Blade Length Study, the relative velocity was higher at the suction side, and the relative velocity at the pressure side was lower compared to designs with lower Zweifel coefficients. To show more detail into the flow features, vector diagrams were produced at the leading and trailing edges, vectors at the leading edge are shown below in Figure 3.41 for two designs in case 5.

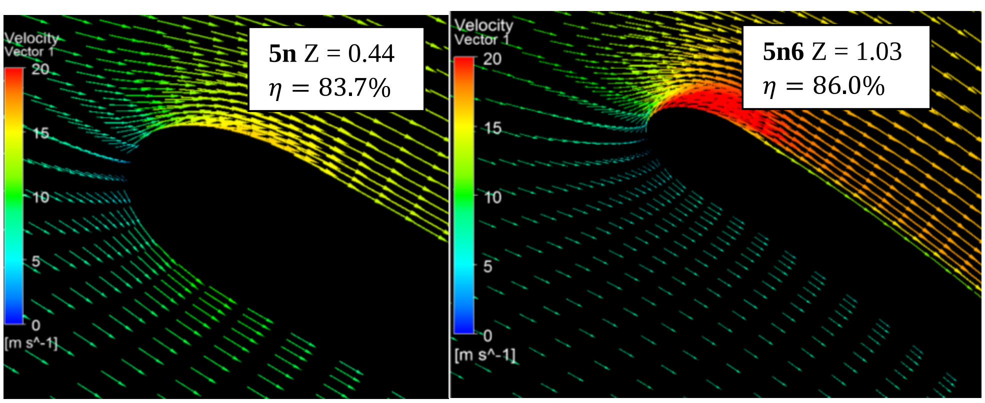

Figure 3.41. Relative velocity vectors at leading edge for case 5 of Blade Length Study (Span 50%)

As Zweifel coefficient was increased, flow acceleration at the leading edge suction side increased. This is shown in Figure 3.41 above, and is also seen below in Figure 3.42 for case 3, and Figure 3.43 for case 1. For each design simulated in the Blade Length Study, this effect was observed.

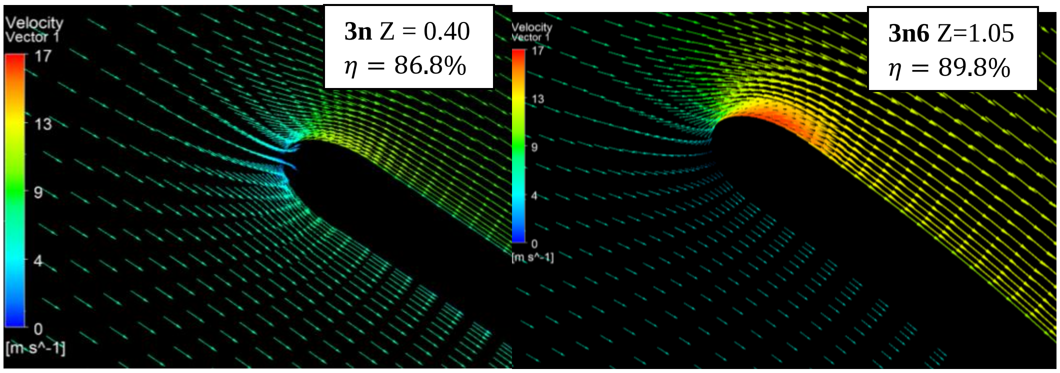

Figure 3.42. Relative velocity vectors at leading edge for case 3 of Blade Length Study (Span 50%)

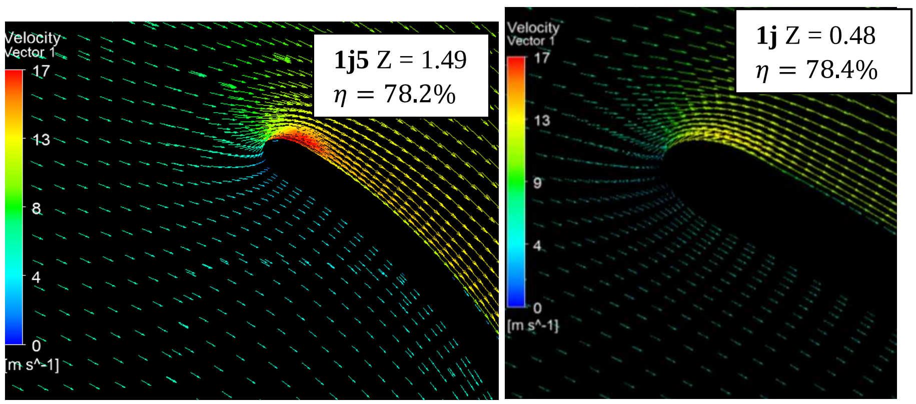

Figure 3.43. Relative velocity vectors at leading edge for case 1 of Blade Length Study (Span 50%)

The below figures show the velocity vectors at the trailing edge for designs in cases 1, 5 and 3, Figures 3.55, 3.56, and 3.57 respectively.

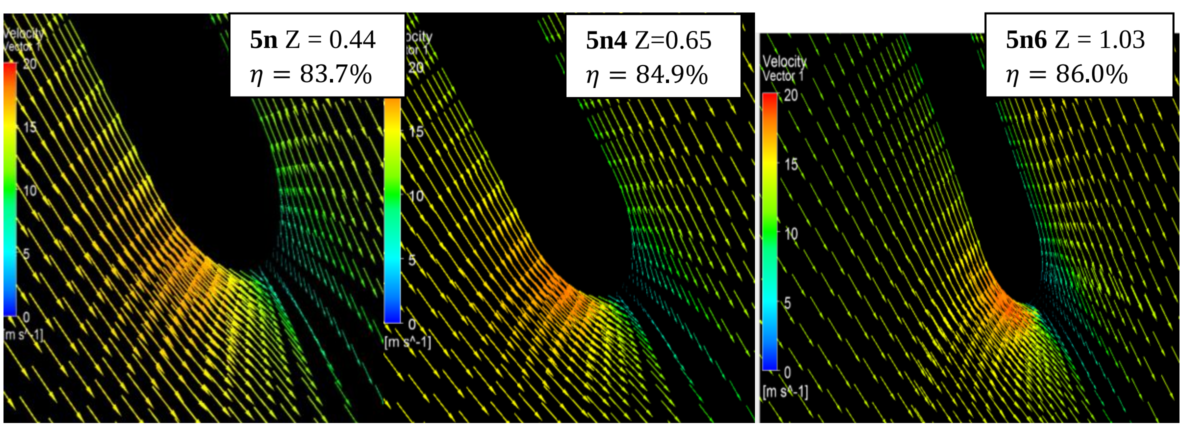

Figure 3.44. Relative velocity vectors at trailing edge for case 5 of Blade Length Study (Span 50%)

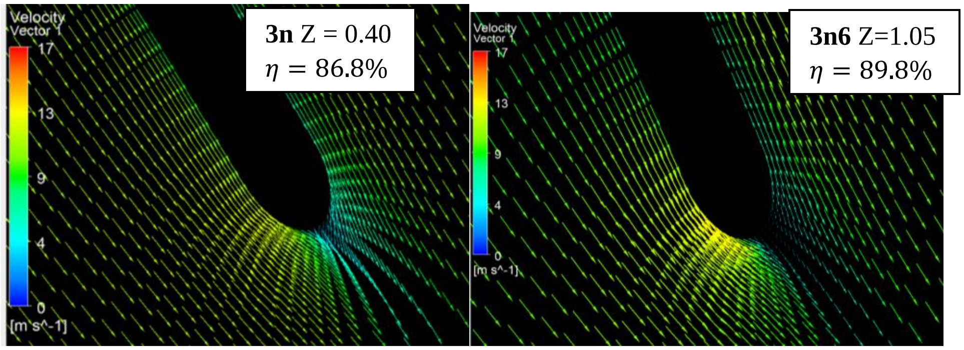

Figure 3.45. Relative velocity vectors at trailing edge for case 3 of Blade Length Study (Span 50%)

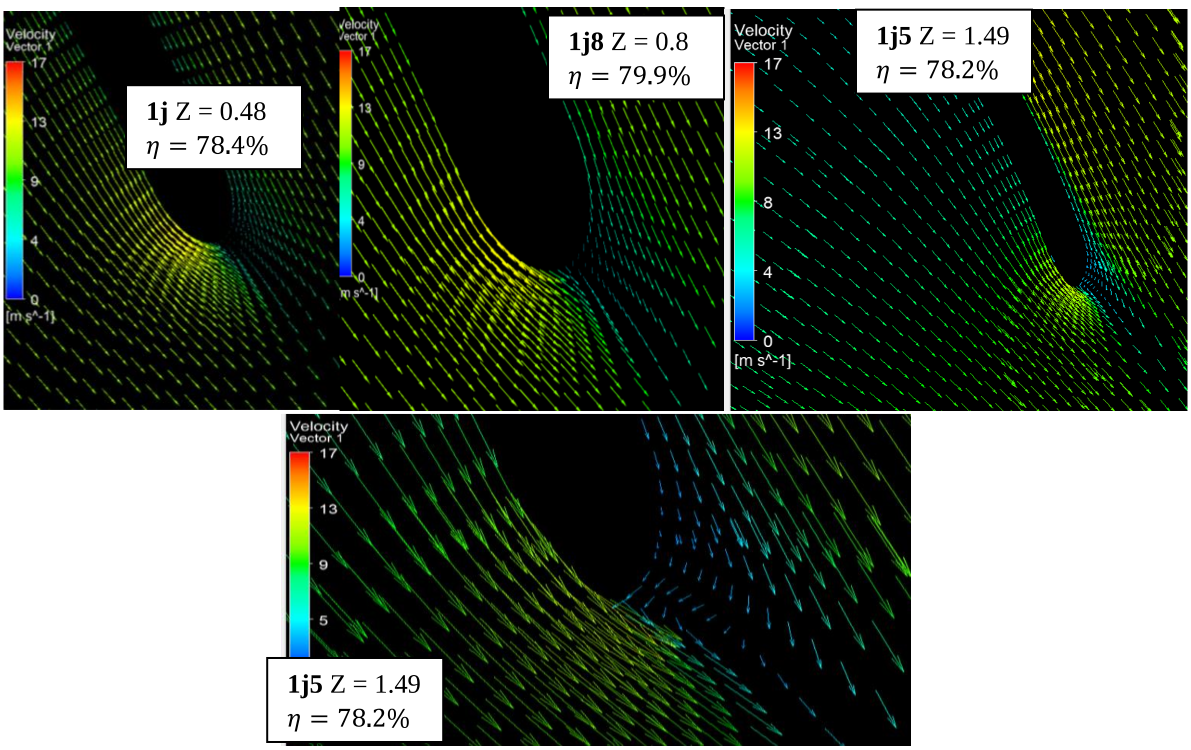

Figure 3.46. Relative velocity vectors at trailing edge for case 1 of Blade Length Study (Span 50%)

3.5.3. Trailing Edge Effects

The above figures illustrate that as Zweifel coefficient was increased, flow acceleration near the trailing edge on the pressure side of the flow increased. On the suction side as flow travels towards the trailing edge, flow decelerates and experienced an adverse pressure gradient, and the boundary layer along this surface became larger. The designs with higher Zweifel coefficient experienced more flow deceleration towards the trailing edge on the suction side, velocity gradients at the leading and trailing edges, and larger size boundary layers. As Zweifel coefficient was increased the wake left by the trailing edge became larger, and shifted closer toward the suction side. These effects can result in additional viscous shear, turbulence, entropy production, and losses at the trailing edge. This effect was observed for each of the designs that were simulated as a part of the Blade Length Study.

Figure 3.47 below shows the magnitude of the relative flow velocity near the blade surface for designs 3n,3n3, and 3n6 of case 3, from 80% along the blade chord to the trailing edge. Each design experienced flow acceleration at the pressure side near the trailing edge. The figure shows the magnitude of this flow acceleration was highest for the designs with the shortest blades. The designs with larger Zweifel coefficients had greater velocity gradients over a smaller axial distance. This suggests the shear stresses and entropy production in this region are higher. This effect was observed for each design simulated as a part of the Blade Length Study.

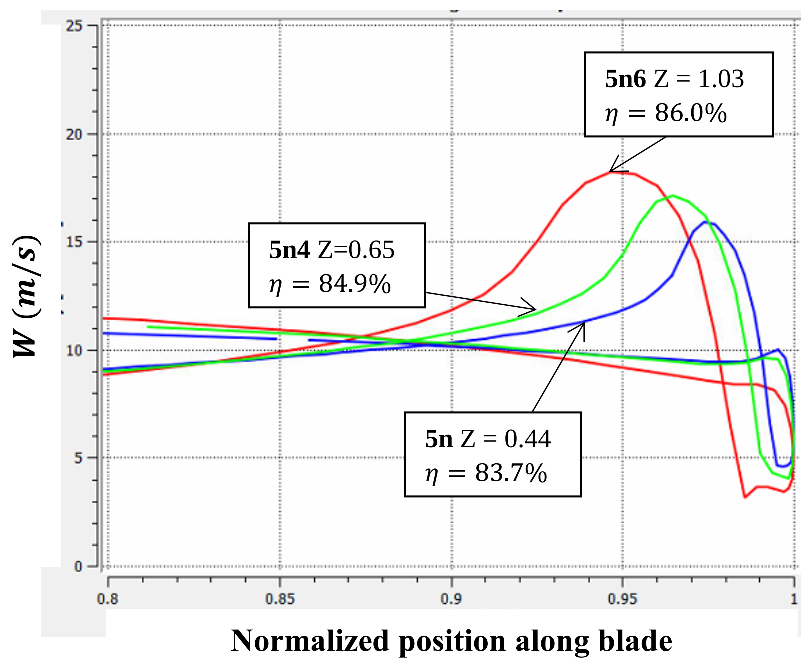

Figure 3.47. Relative velocity near trailing edge of case 3 and 5 of Blade Length Study

Figure 3.48 below shows a contour of the turbulence kinetic energy two designs in case 1 of the Blade Length Study, Figure 3.49 shows two designs in case 3 and Figure 3.50 shows two designs in case 5. These figures illustrate the increased turbulence at the trailing edge for the shorter blade length designs.

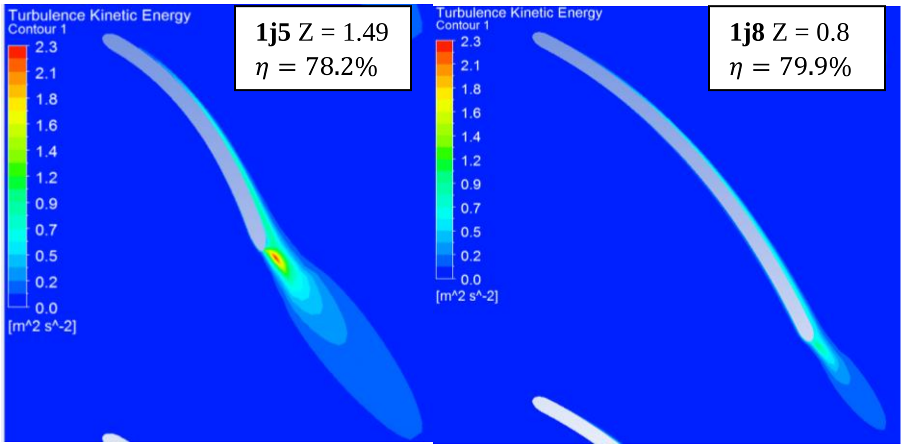

Figure 3.48. Turbulence kinetic energy contour for cases 1j5 and 1j8: Span 50%

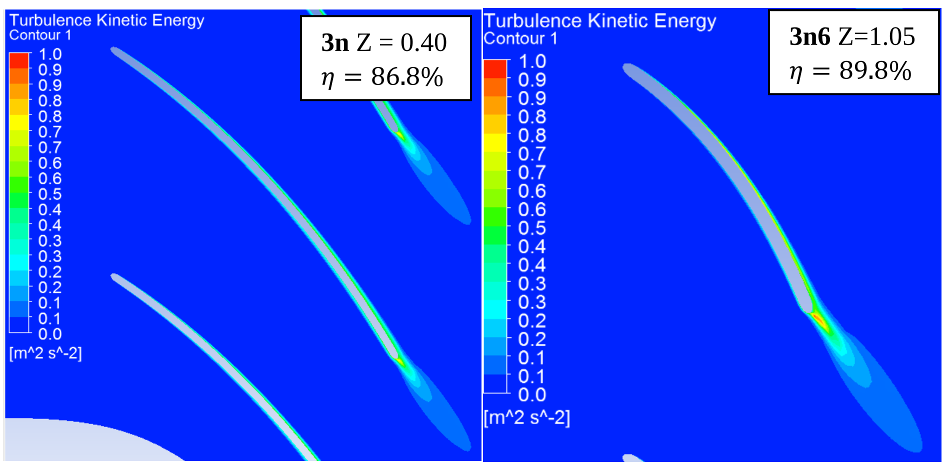

Figure 3.49. Turbulence kinetic energy contour for designs 3n and 3n6: Span 50%

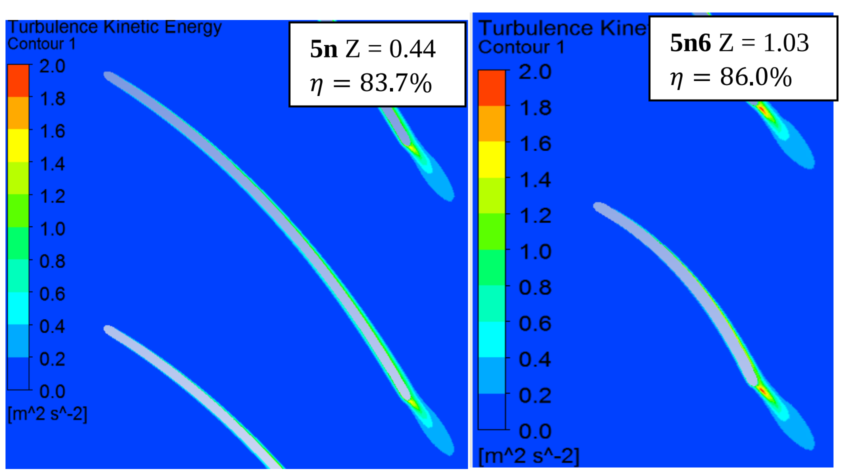

Figure 3.50. Turbulence kinetic energy contour for designs 5n and 5n6: Span 50%

Figure 3.51 below shows exit loss coefficient graphed vs Zweifel coefficient for each design in the Blade Length Study. For Zweifel coefficients under .8, the exit loss coefficient ξ_{2-c} was relatively constant, however as Z was increased above 0.8, the exit loss coefficient increased, which is likely the result of increased losses resulting from the trailing edge wake.

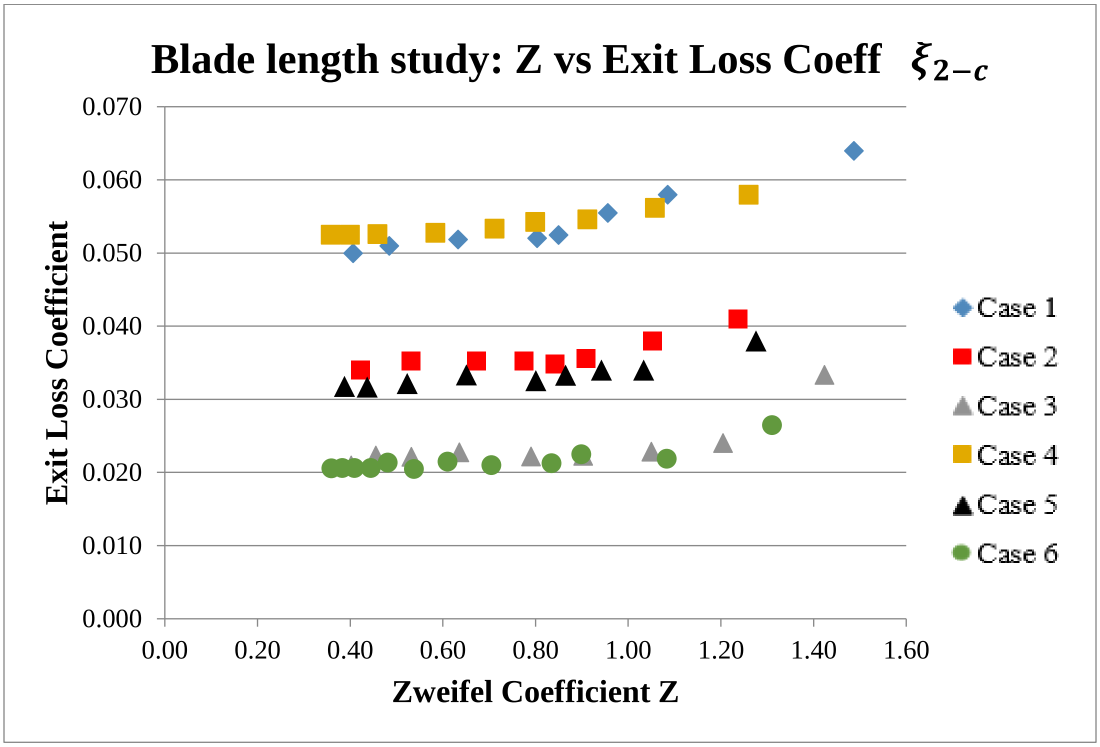

Figure 3.51. Zweifel Coefficeint vs Exit Loss Coefficient for Blade Length Study

Turbines are usually designed to have a thin trailing edge. Blade profiles with high Zweifel coefficient require careful design and iteration to reduce trailing edge losses and reduce the risk of flow separation. Performance of the designs investigated in this work could be improved by tapering the trailing edge, especially those with high Zweifel coefficients, to reduce the trailing edge losses and wake size after the trailing edge.

3.5.4. Blade Loading

With shorter blades, total pressure must decrease over a shorter axial distance. This can lead to more flow deviation and velocity gradients at the leading and trailing edges, which can lead to additional losses. The designs with higher values of *Z* exhibited flows with lower pressure on the suction side of the blade, and higher pressure on the pressure side. With shorter axial length, the pressure difference from pressure to suction side needs to be larger to keep power constant, as the area on which the pressure acts is smaller, and the same force must be maintained to keep power constant. Simulations showed that as Zweifel coefficient was increased by decreasing blade length, an adverse pressure gradient developed on the suction side of the blades after the point of minimum pressure. Another adverse pressure gradient at the trailing edge at the suction side became more pronounced as Zweifel coefficient was increased. Adverse pressure gradients are correlated with boundary layer growth, entropy generation, and increased losses.

Below Figure 3.52 shows the pressure vs. blade position (blade loading) charts for case 3 at three Zweifel coefficients, at 50% span. Figure 3.53 shows static pressure contours for the three designs within case 3 of the Blade Length Study. Figure 3.54 and 3.66 show the blade loading chart and static pressure contours respectively for three designs within case 5. The shorter blade length designs experienced flows with lower pressure on the suction side of the blades, the figures illustrate this effect. For each design simulated in this work, towards the trailing edge an area of low pressure and flow acceleration on the pressure side of the blade was observed, located close next to an area of flow deceleration, an adverse pressure gradient, at the suction side trailing edge. As the blade length was decreased this effect was magnified, and the region was observed over a larger portion of the distance along the blade.

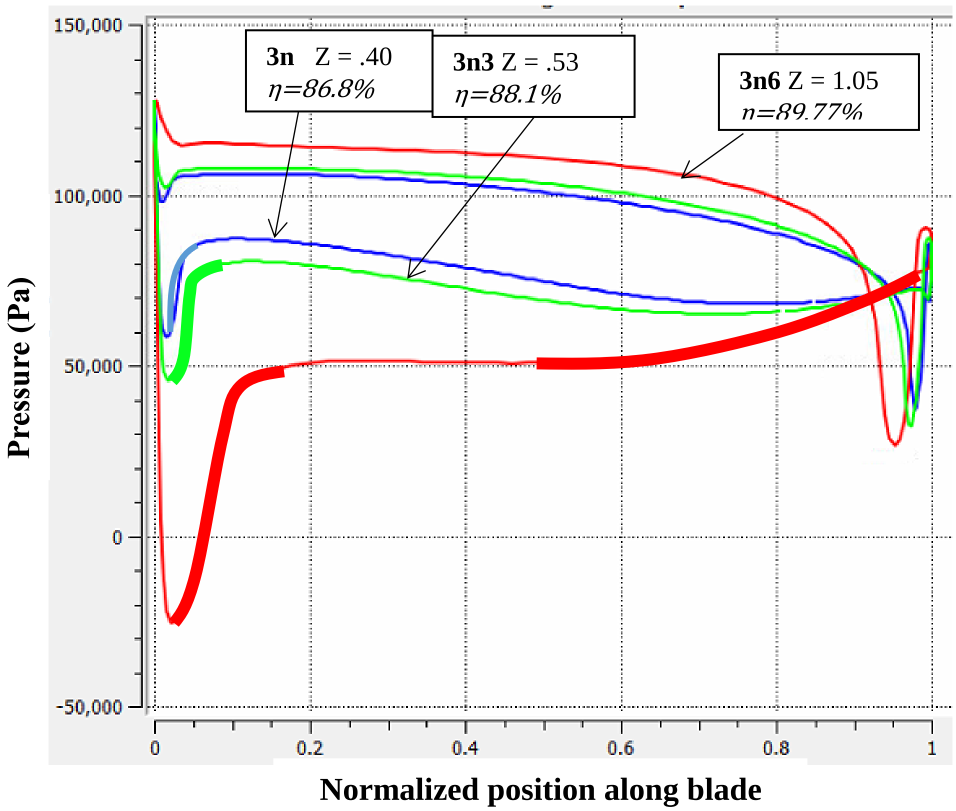

Figure 3.52. Blade loading diagrams for case 3 of Blade Length Study: Span 50%

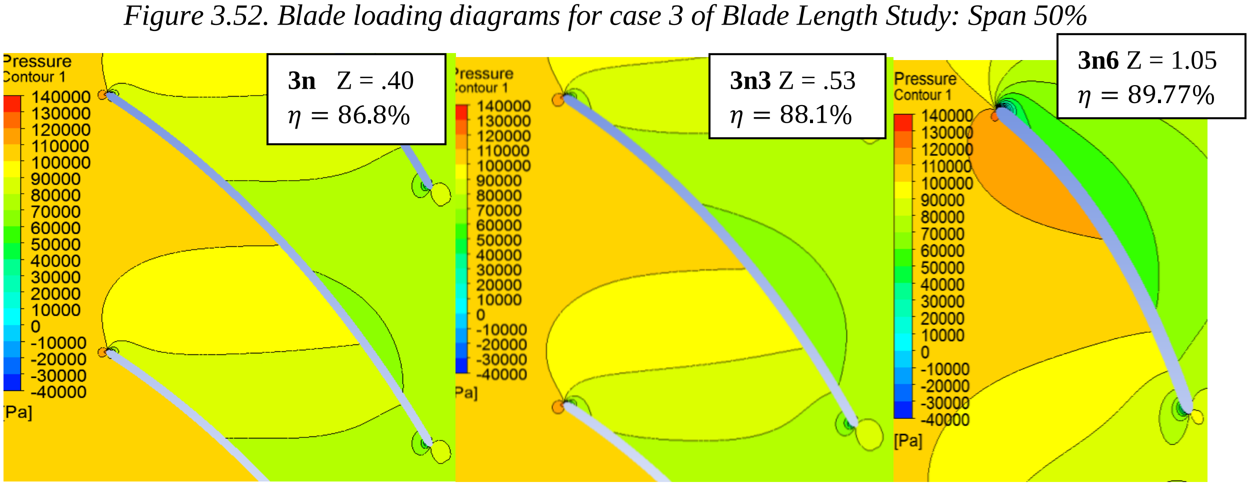

Figure 3.53. Static Pressure Distributions for Case 3 of Blade Length Study (Span 50%)

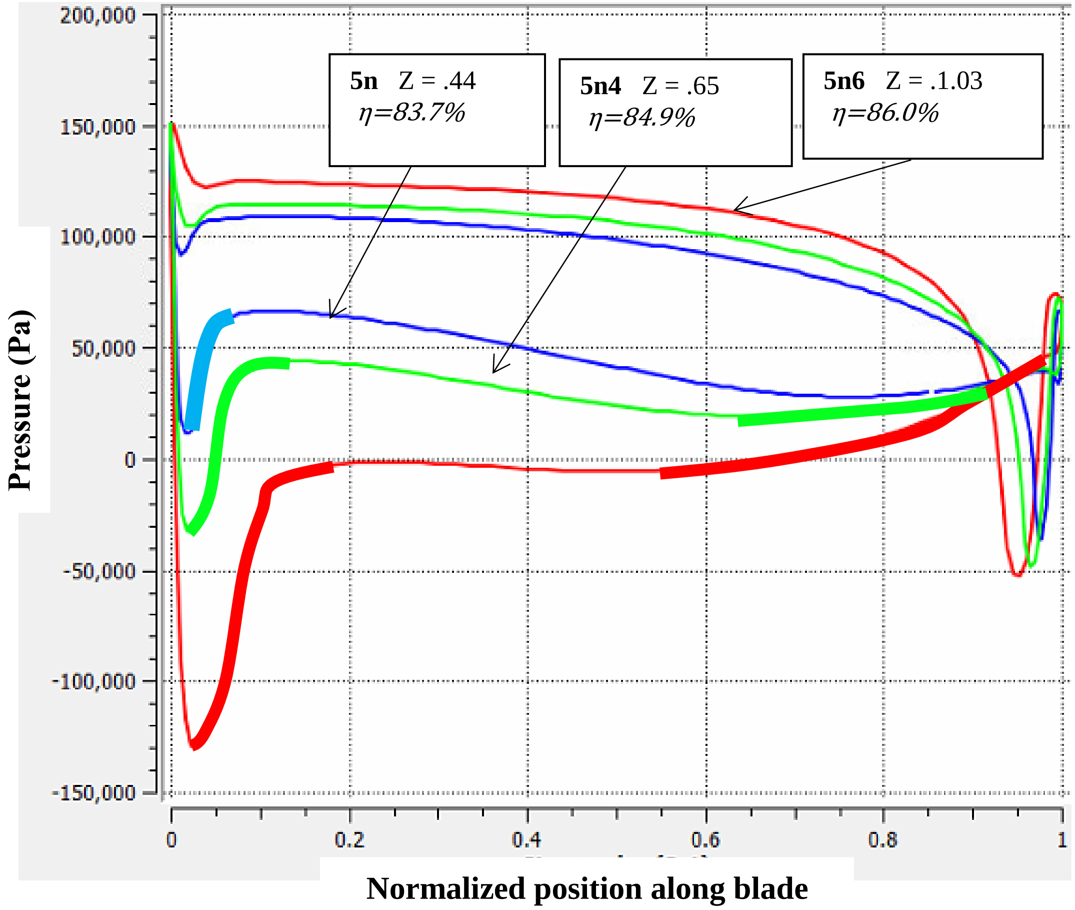

Figure 3.54. Blade loading diagrams for case 5 of Blade Length Study: Span 50%

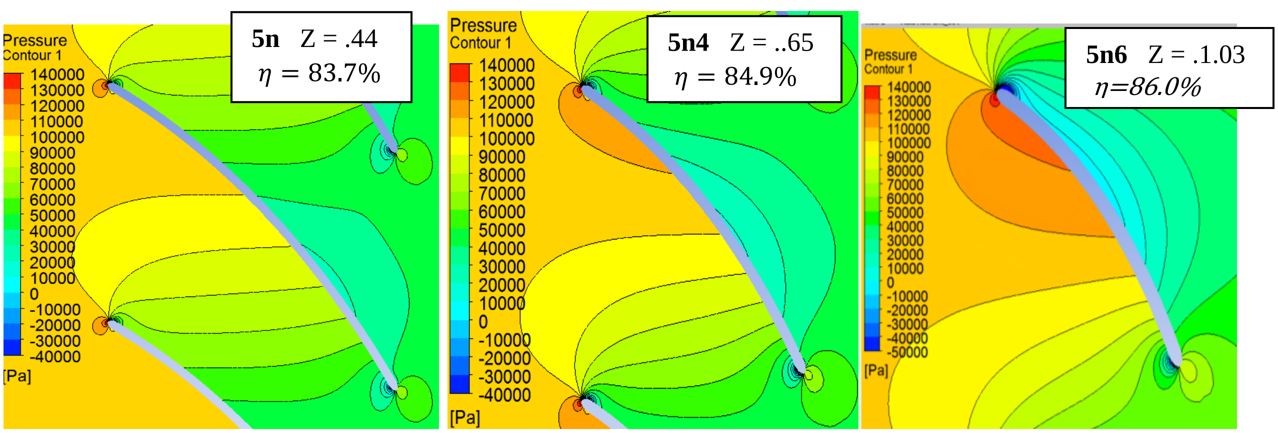

Figure 3.55. Static Pressure Distributions for Case 5 of Blade Length Study (Span 50%)

Figures 3.67 and 3.68 below show velocity triangles superimposed over velocity vector contours and blade loading diagrams produced in CFD-Post for two designs in case 2, designs 2l and 2l8. The figure illustrates how as Zweifel coefficient increases, velocity on the suction side of the blades increases, and velocity on the pressure side of the blades decreases.

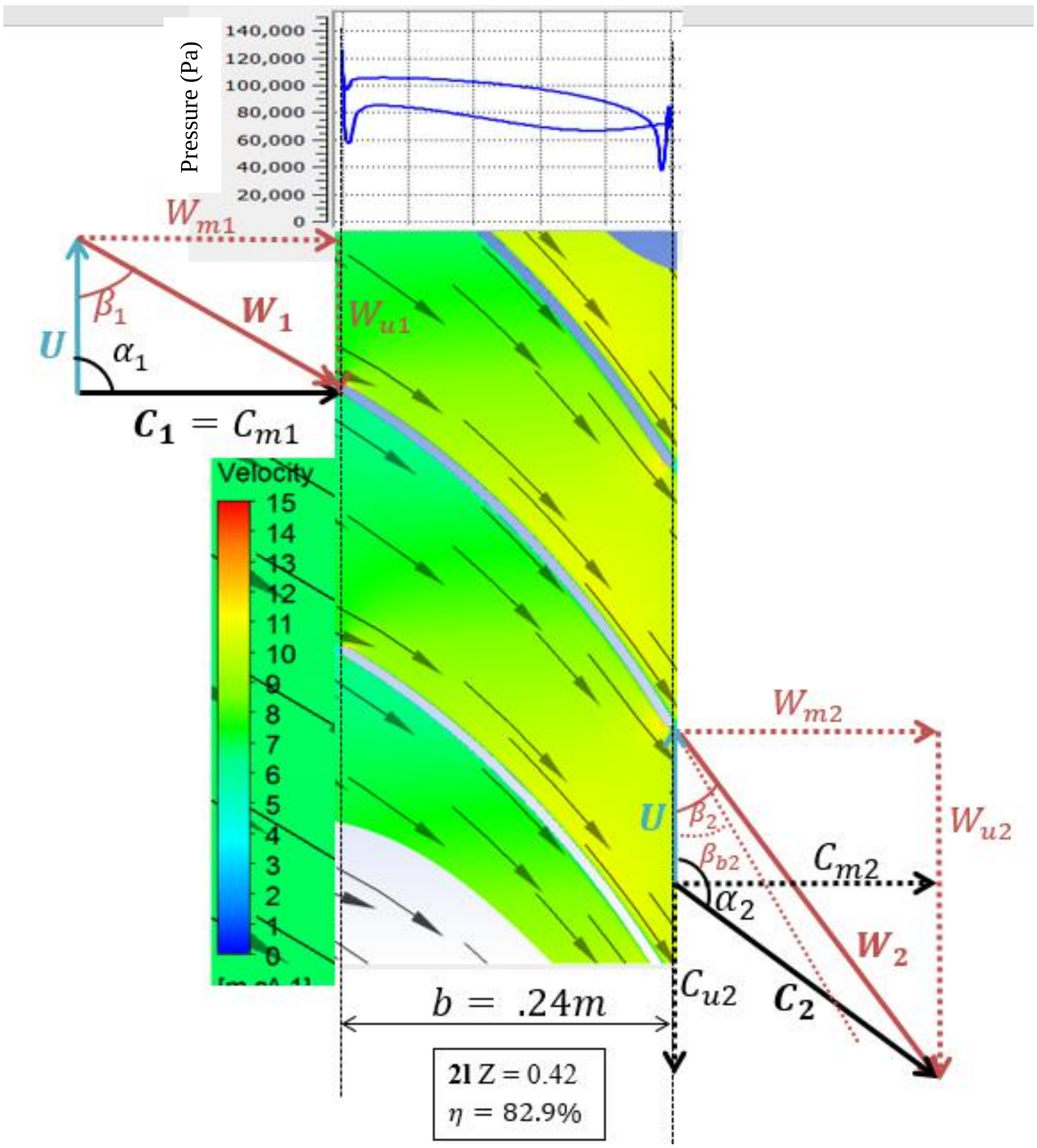

Figure 3.56.Velocity triangles superimposed over velocity vector contours for design 2l of the Blade Length Study at leading and trailing edge (span 50%)

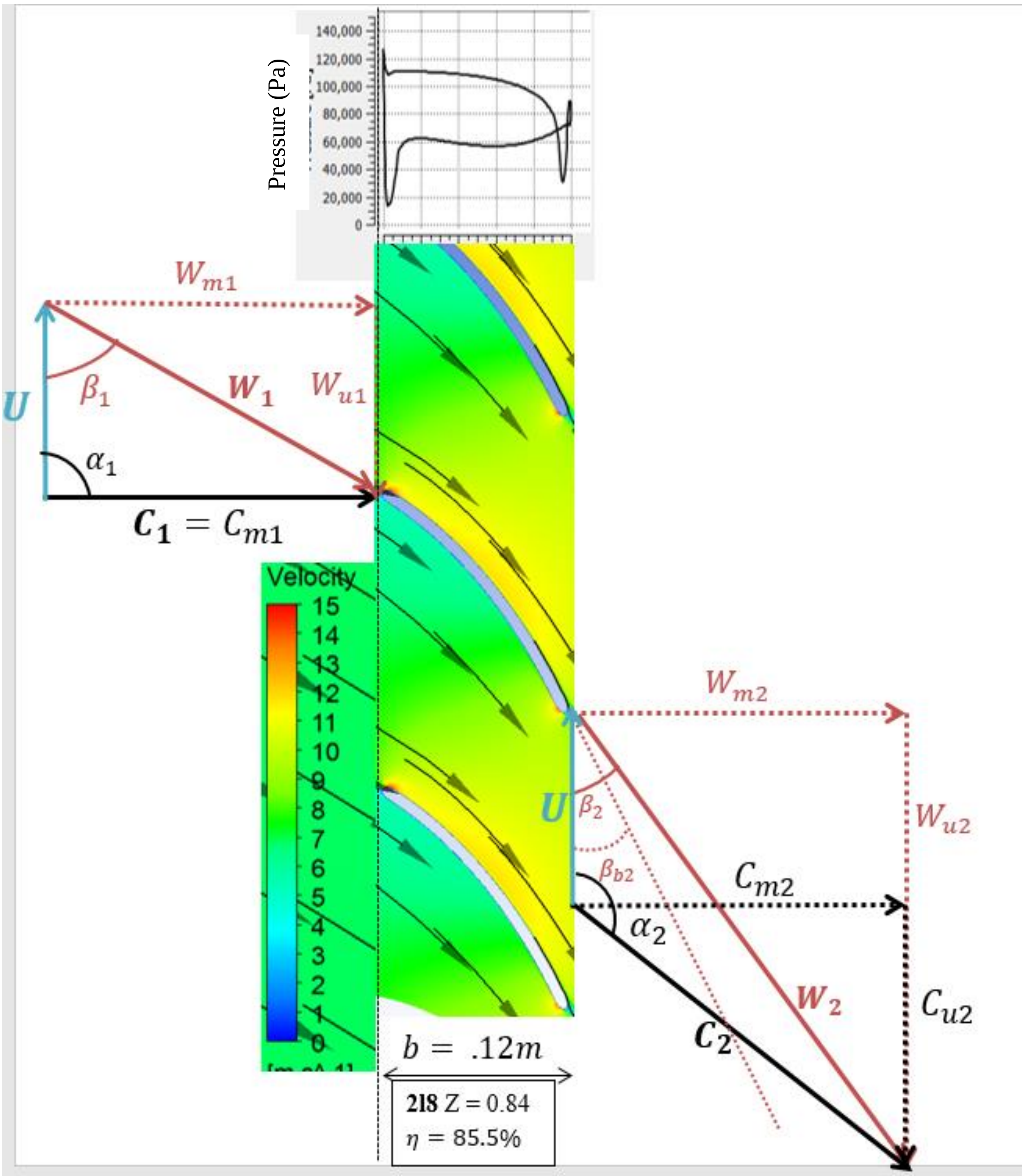

Figure 3.57.Velocity triangles superimposed over velocity vector contours for design 2l8 of the Blade Length Study at leading and trailing edges (span 50%)

3.5.5. Hub and Shroud Effects

Literature suggests that for the designs with higher Zweifel coefficient, losses via friction from the blade surfaces, hub and shroud are reduced, however the losses resulting from diffusion and shear stresses at the trailing edge are higher [24] [29]. The results obtained in the Blade Length Study correlate with these findings.

To investigate the effects of friction resulting from the hub and shroud surfaces, Charts were generated which tracked the relative velocity of the flow along the span of the blades. Figure 3.58 below shows relative flow velocity graphed along the span of the blades at the leading edge of the turbine for case 3, and Figure 3.59 shows the relative flow velocity graphed along the span at the trailing edge. Decreased relative flow velocity was exhibited near the hub and shroud for each design tested, indicating friction effects. The designs with higher Zweifel coefficient experienced a larger decrease in relative velocity at the hub and shroud as the flow traveled from leading to trailing edge. Although the velocity distribution at the leading edge was similar for each of the designs, the designs with lower Zweifel coefficient experienced decreased relative flow velocity at the trailing edge, especially near the hub and shroud. This suggests the lower Z designs experienced additional friction resulting from the hub and shroud surfaces, compared to the higher Z designs.

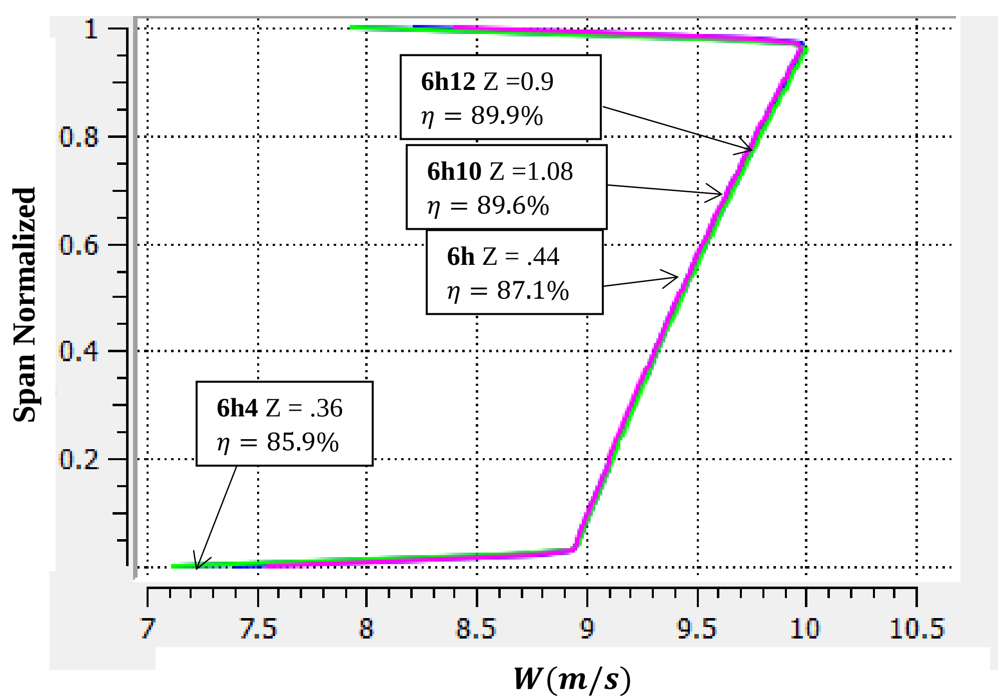

Figure 3.58. Relative velocity of case 6 for Blade Length Study at the leading edge along span

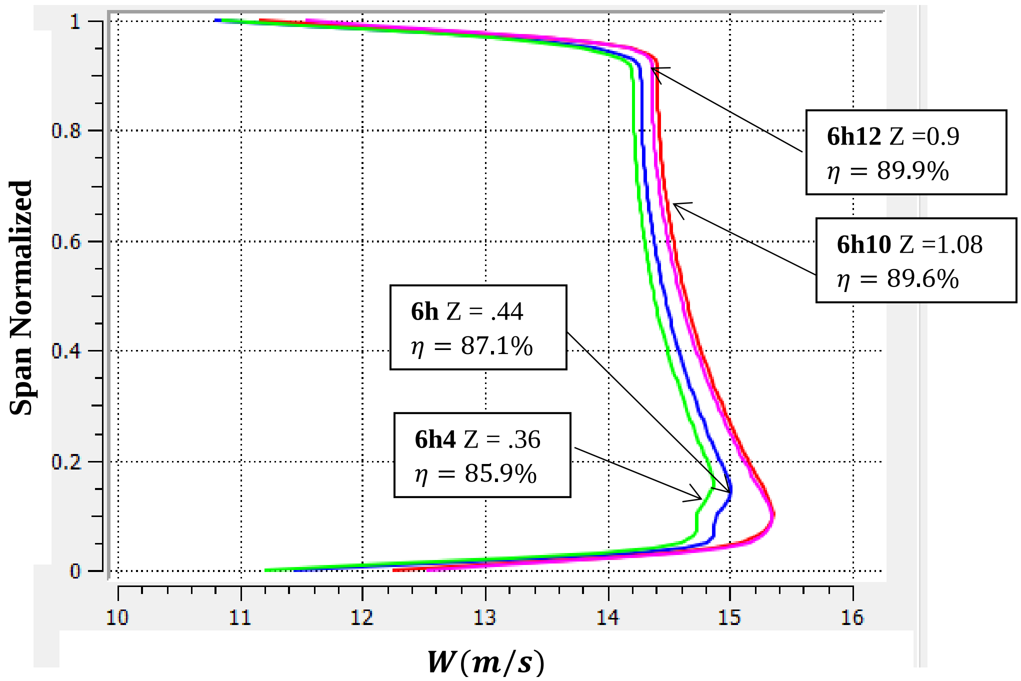

Figure 3.59. Relative velocity of case 6 for Blade Length Study at the trailing edge along span

Profile loss coefficient $\xi_{profile}$ was graphed vs the Zweifel coefficient to track how Z effected losses from the leading to trailing edge. Figure 3.60 below shows that as Zweifel coefficient was increased from the lowest values to .8, $\xi_{profile}$ decreased. However for the Zweifel coefficients above .8, $\xi_{profile}$ stayed relatively constant.

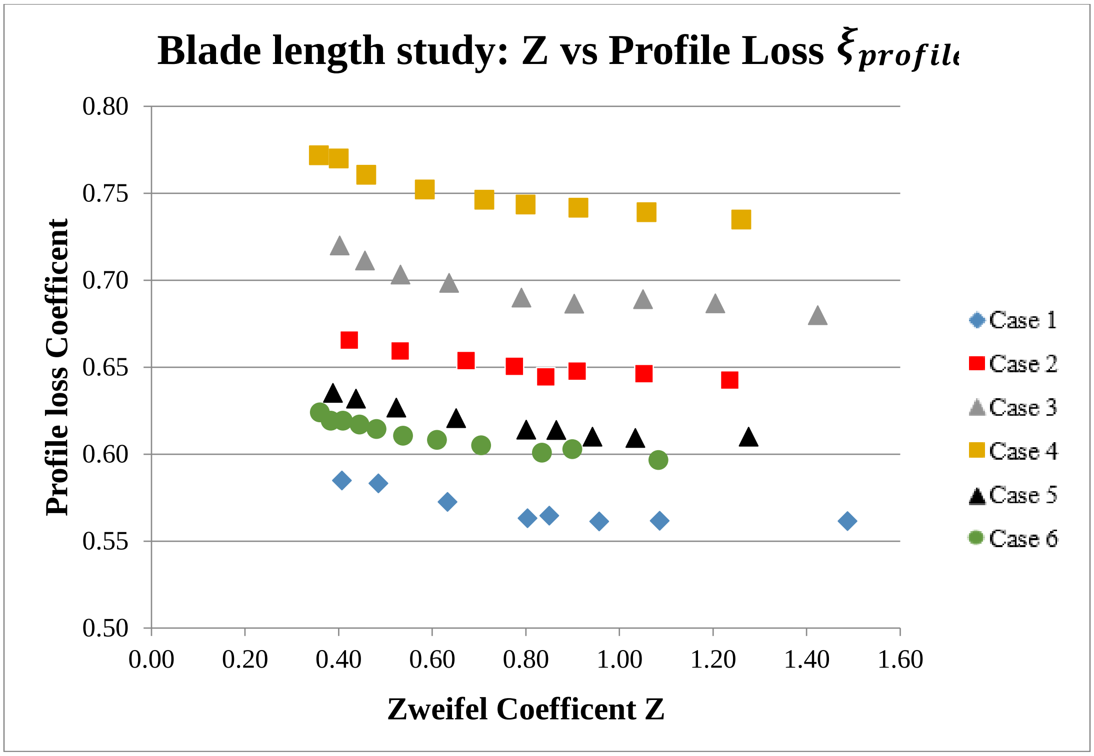

Figure 3.60. Zweifel coefficeint vs Profile loss coefficient for Blade Length Study

3.5.6. Work Extraction

Average relative flow velocity was graphed from annulus inlet to annulus outlet. Figure 3.61 below shows average relative velocity from inlet to outlet for case 1, Figure 3.62 for case 6. The designs with higher efficiency had higher relative velocity at the trailing edge, however each design had equal relative velocities at the leading edge. As W_m stays constant from inlet to outlet, the highest efficiency designs had the highest average relative circumferential velocity at the trailing edge, W_{u2}.

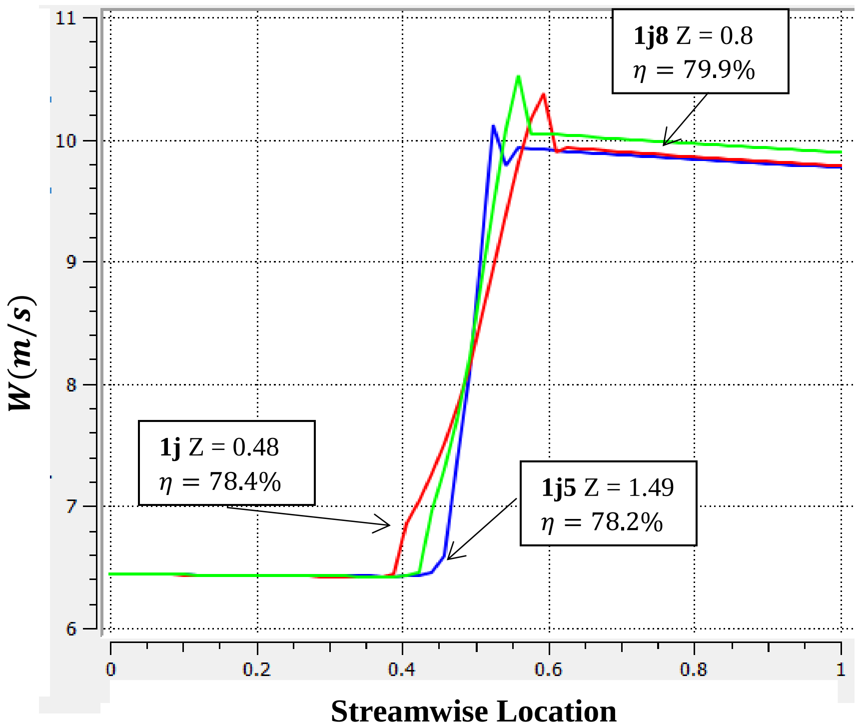

Figure 3.61. Average relative velocity from inlet to outlet for case 1 for Blade Length Study

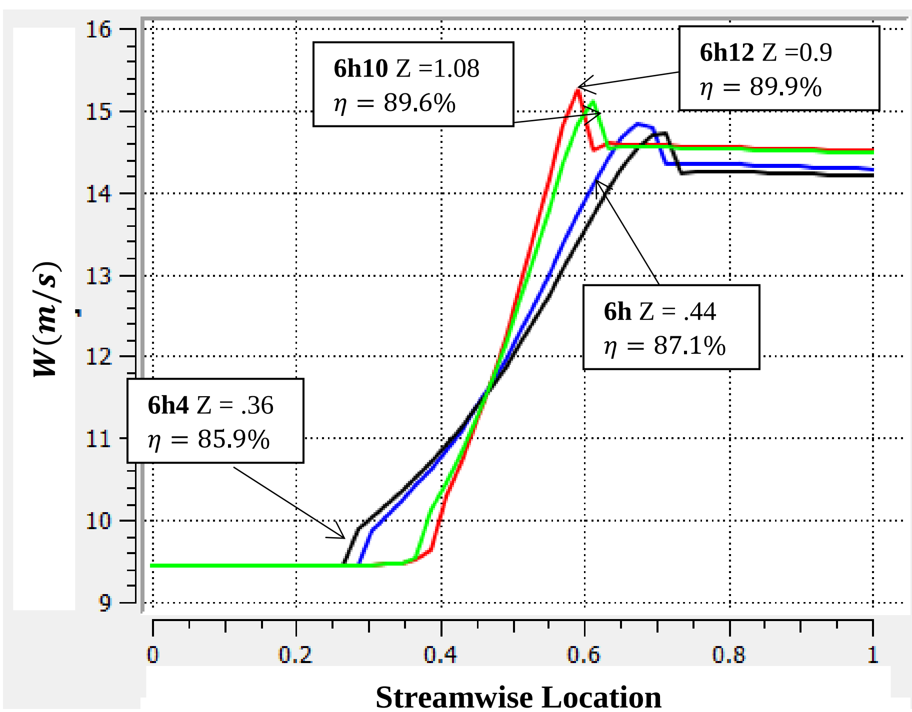

Figure 3.62. Average relative velocity from inlet to outlet for case 6 for Blade Length Study

The simulations of each design produced results which predicted reduced work extraction near the hub and shroud for each design. This is illustrated in the figures below, which display absolute circumferential flow velocity over the span at the trailing edge. Figure 3.63 below shows absolute circumferential velocity graphed along the span of the blades for three designs in case 6 of the Blade Length Study, at the trailing edge, and Figure 3.64 shows this for case 1. The designs with Zweifel coefficients between 0.8 and 1.1 exhibited the highest absolute circumferential velocity C_u near the hub at the trailing edge. These designs had the highest change in angular momentum, and therefore work extraction, near the hub compared to those with Zweifel coefficients outside this range.

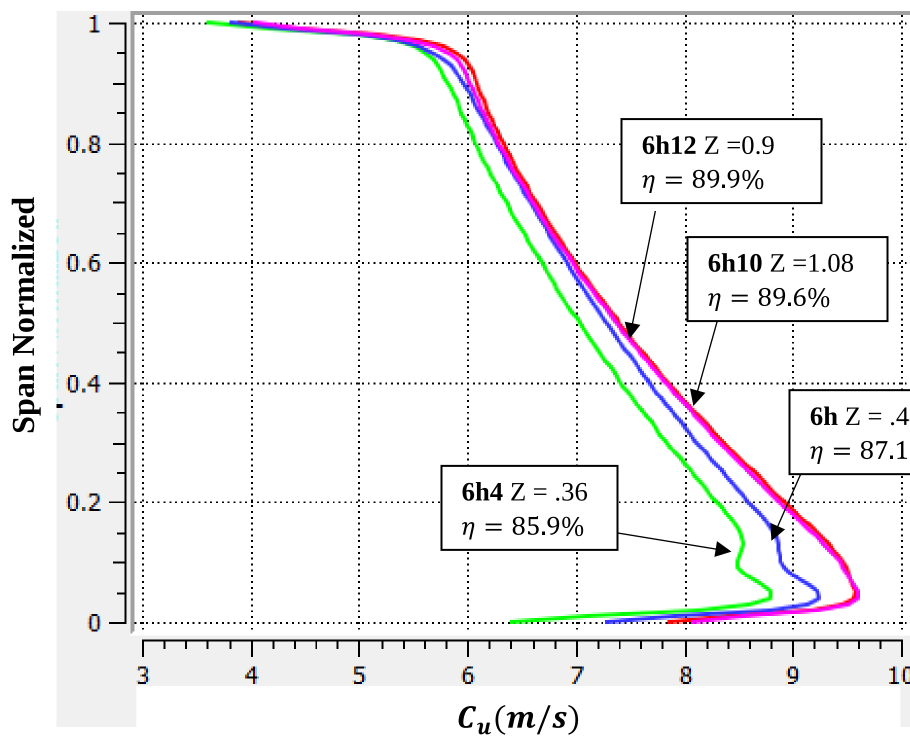

Figure 3.63. Absolute circumferential velocity for case 6 of the Blade Length Study at the trailing edge along span

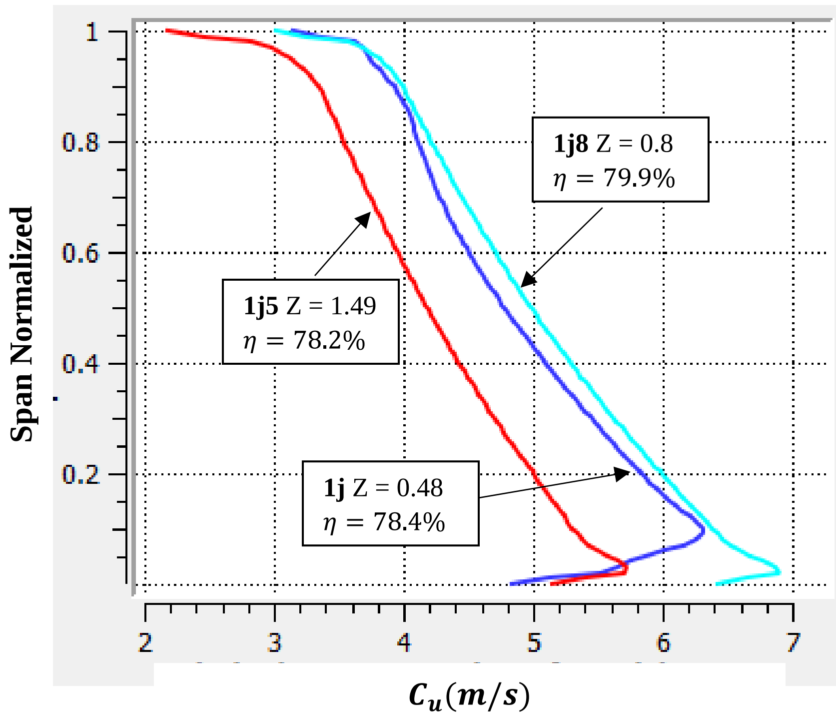

Figure 3.64. Absolute circumferential velocity for case 1 of the Blade Length Study at the trailing edge along span

Graphs were generated which show C_u from inlet to outlet for each design, Figure 3.65 below shows this for case 6, and Figure 3.66 for case 1. The designs which had the highest predicted efficiency had the highest circumferential velocity at the trailing edge (C_{u2}). As absolute circumferential velocity at the leading edge, $C_{u1} = 0$, this means the highest efficiency designs exhibited flows with the largest change in absolute circumferential velocity $C_{u2} - C_{u1}$. These designs had the most work extraction, they exhibited flows with the largest change in angular momentum.

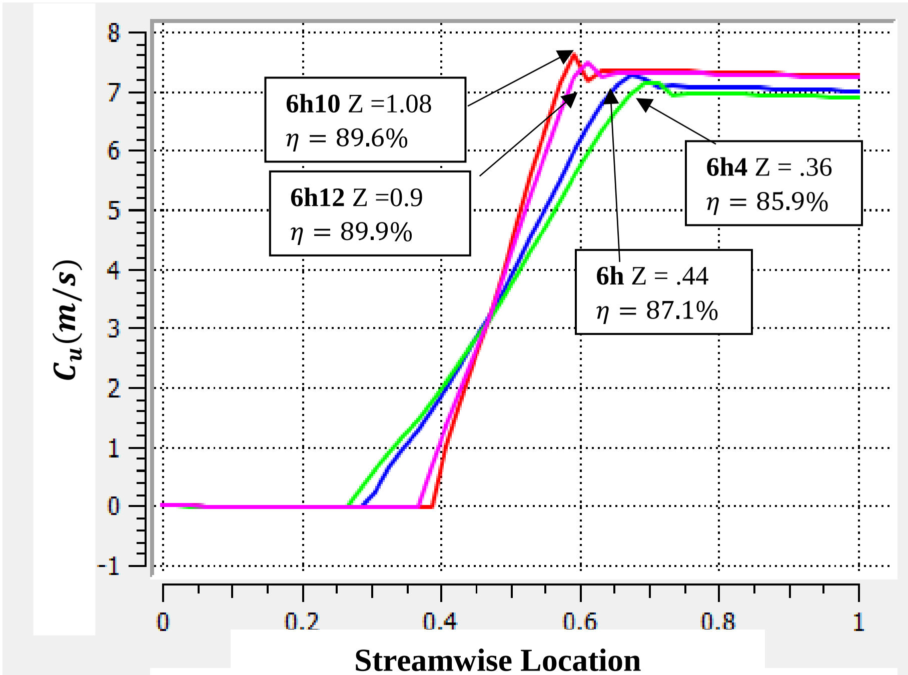

Figure 3.65. Average Absolute circumferential velocity from inlet to outlet of case 6 of Blade Length Study

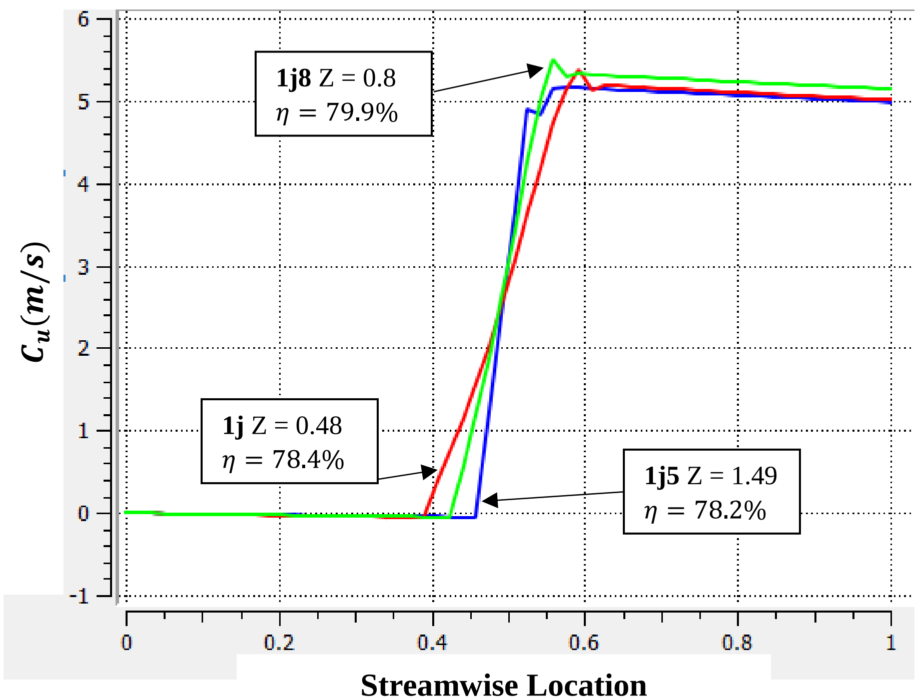

Figure 3.66. Average Absolute circumferential velocity from inlet to outlet of case 1 of Blade Length Study

To help observe the effect of reducing Zweifel coefficient on the simulated work extraction, the product of absolute circumferential velocity C_u and rotational velocity U_θ was graphed over the span of the at the trailing edge for each design. Figure 3.67 below shows $U_\theta C_u$ graphed for three designs in case 1 of the Blade Length Study at the trailing edge of each turbine. The highest efficiency designs had the highest value of $U_\theta C_u$ at the trailing edge. As Zweifel coefficient was increased, work extraction $U_\theta C_u$ at the trailing edge increased. However as Zweifel coefficient was increased above 1.2, $U_\theta C_u$ at the trailing edge decreased. This effect can be seen below in Figure 3.67 below, although the same effect was observed for each case in the Blade Length Study. The designs were set up to have no pre-swirl, such that $C_{u1} = 0$. Designs which had the highest $U_\theta C_u$ at the trailing edge had the highest efficiency, as these designs exhibited flows with the largest change in angular momentum, and thus the largest shaft power.

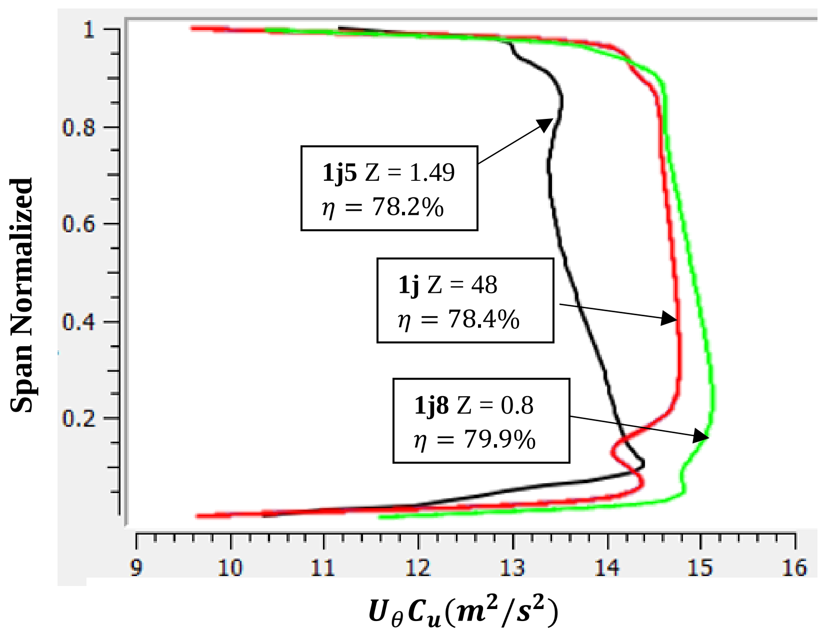

Figure 3.67. $U_\theta C_u$ for case 1 of the Blade Length Study at the trailing edge across span

3.5.7. Cavitation

As blade length was decreased to lower Zweifel coefficient, areas of low static pressure developed on the suction side of the blades, which could lead to cavitation in a real-world application. The below figures show areas of low static pressure for different designs in the

Blade Length Study. Figure 3.68 shows the low static pressure contour for case 1, Figure 3.69 for case 2, Figure 3.70 for case 3, Figure 3.71 for case 4, Figure 3.72 for case 5, and Figure 3.73 for case 6. The results suggest that as Z is increased, the risk of cavitation became greater.

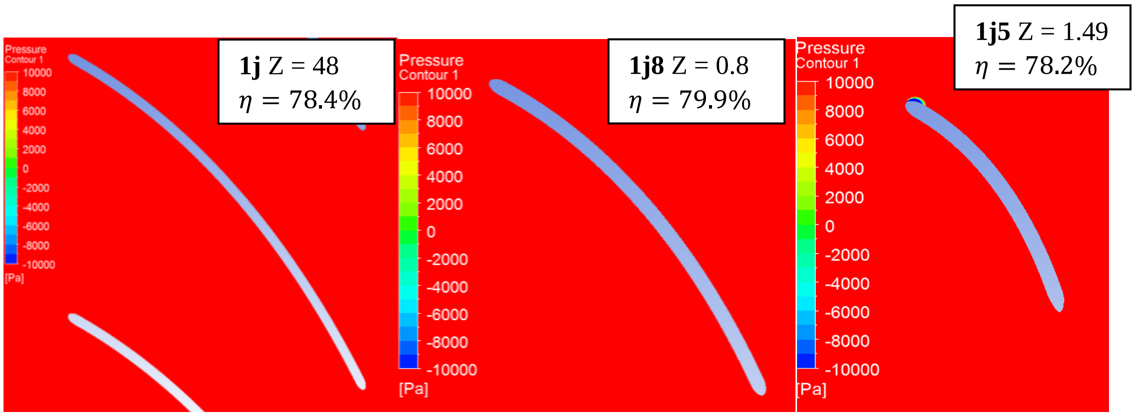

Figure 3.68. Areas of low static pressure for case 1 of Blade Length Study (Span 50%)

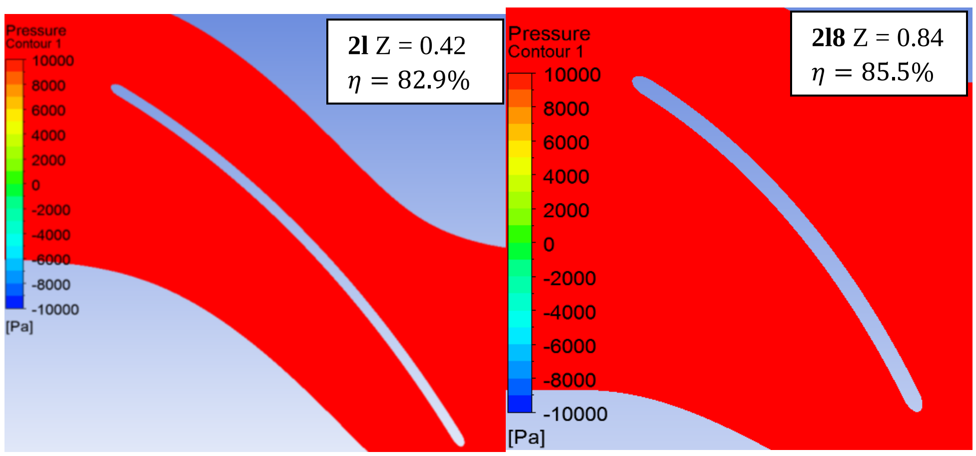

Figure 3.69. Areas of low static pressure for case 2 of Blade Length Study (Span 50%)

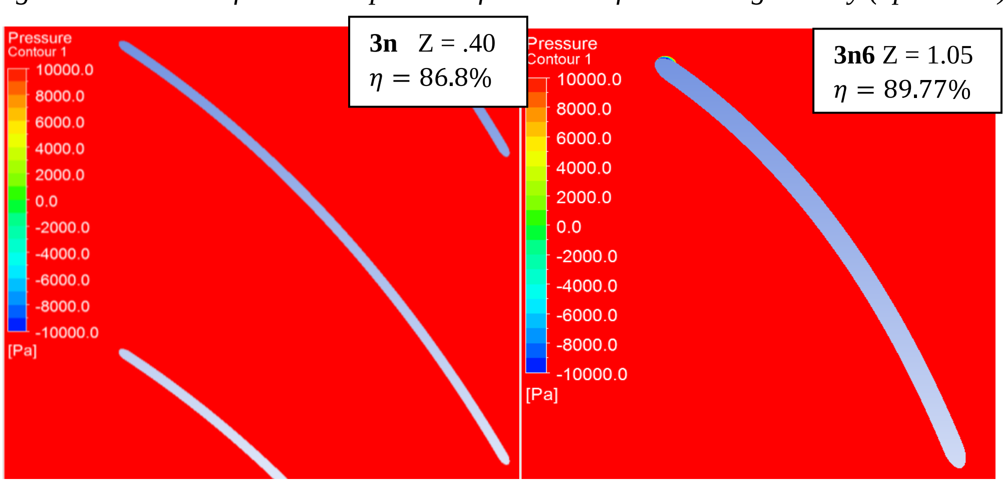

Figure 3.70. Areas of low static pressure for case 3 of Blade Length Study (Span 50%)

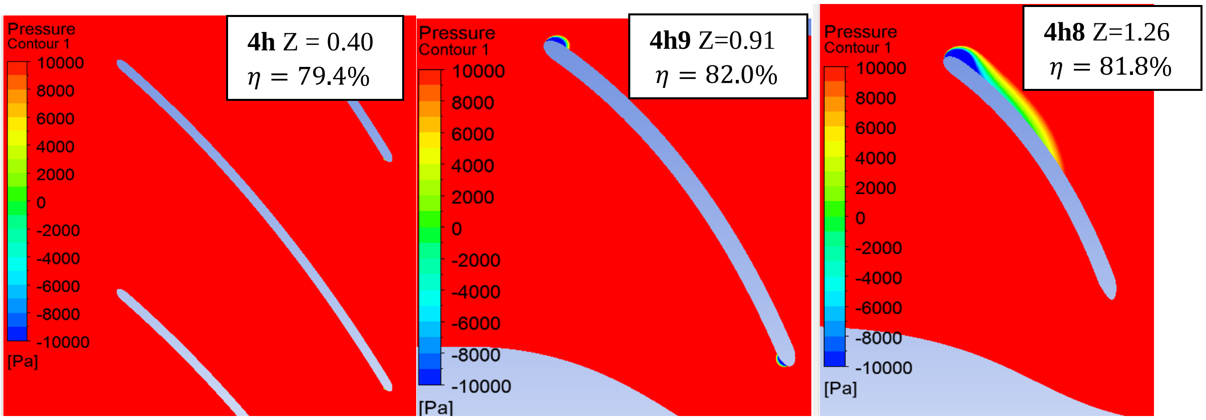

Figure 3.71. Areas of low static pressure for case 4 of Blade Length Study (Span 50%)

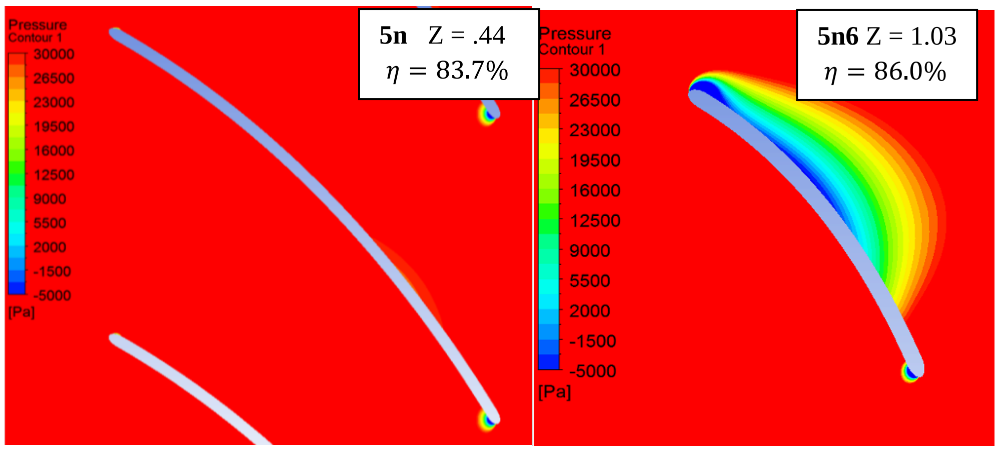

Figure 3.72. Areas of low static pressure for case 5 of Blade Length Study (Span 50%)

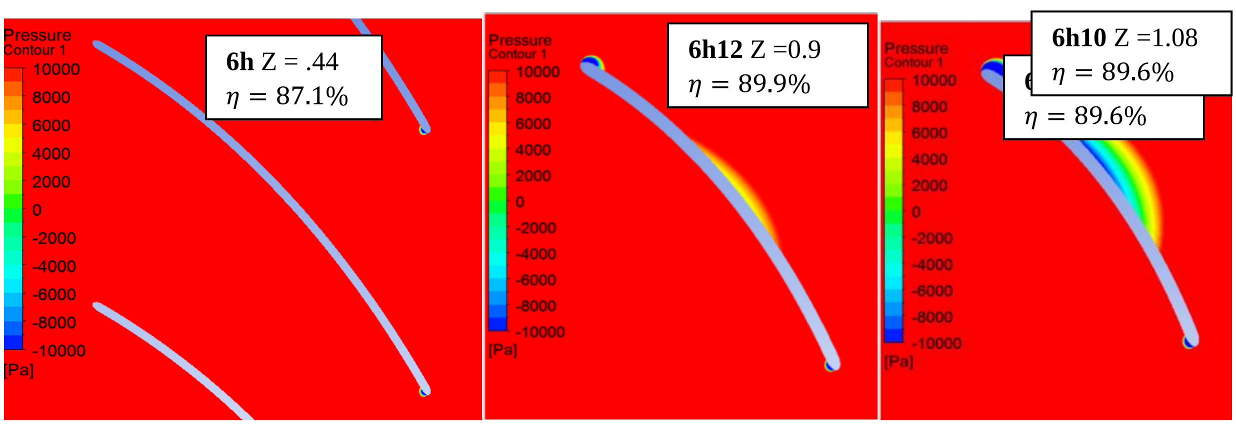

Figure 3.73. Areas of low static pressure for case 6 of Blade Length Study (Span 50%)

CHAPTER 4. CONCLUSIONS

No flow separation was observed for any of the designs simulated, and after optimizing the rotational speed and blade length each set of specifications had a design with efficiency predicted via CFD over 79%. This is despite the fact the highest efficiency designs simulated were located below the Cordier Line. The designs with lower diameter and smaller cross-sectional area showed significantly lower predicted efficiency, Cases 1 and 4 have a tip diameter of .2 meters, designs done for those cases had a peak efficiency of 80%, compared to 90% for cases 3 and 6, which had a tip diameter of .5 meters.

Both hypotheses introduced in section 1.17 were confirmed in this work. First, the designs simulated with specific speed which place it on the Cordier line performed with lower efficiency than designs with specific speed lower than that recommended by the line. Second, peak efficiency in CFD was obtained in CFD for designs which had Zweifel coefficients between .8 and 1.1.

4.1. Speed Study and Cordier Line

For the Speed Study, six sets of turbine specifications were used to produce turbine designs, which were tested in CFD. Designs were generated and simulated at differing rotational speeds. Highest efficiency was observed in the designs which ran at speeds at a range 12-33% that of the Cordier-recommended speed. Highest efficiencies were recorded when the designs were generated at specific speeds between 1.37 and 1.98, lower than the values of specific speed recommended by the Cordier line, between 5.5 and 6.1.

Designs which were generated for higher rotational speeds experienced more severe adverse pressure gradients on the suction side of the blades in simulation, and more severe velocity gradients near the leading and trailing edges. Turbulence kinetic energy at the trailing edge was higher for the designs which operated at higher rotational speeds. The simulations suggest that as rotational speed was increased, the risk of cavitation on the suction side increased.

4.2. Blade Length Study and Zweifel Coefficient

For the Blade Length Study, the designs at which highest efficiency was measured in the Speed Study were simulated with different Zweifel coefficients. Zweifel coefficient was changed by adjusting axial blade length b. Lower efficiency was predicted for the designs with Zweifel coefficients less than 0.75. Simulated efficiency was highest in the range of $0.8 < Z < 1.1$, within this range efficiency was relatively constant.

With higher Zweifel coefficients, pressure on the suction side is reduced and pressure on the pressure side is increased. Designs which had higher Zweifel coefficients experienced more severe adverse pressure gradients on the suction side of the blades. The higher Zweifel coefficient designs experienced more losses at the trailing edge and had a larger wake after the trailing edge. As Zweifel coefficient was increased, the risk of cavitation on the suction side increased. Increased Zweifel coefficients were correlated with larger flow velocity gradients at the leading and trailing edges of the blades. Trailing edge flow deviation increased linearly as Zweifel coefficient was increased.

Literature suggests that for the designs with higher Zweifel coefficient, losses via friction from the blade surfaces, hub and shroud are reduced, however the losses resulting from diffusion and shear stresses at the trailing edge are higher. The results obtained in the Blade Length Study are in line with this prediction. Profile loss coefficient was lowest for designs within $0.8 < Z < 1.1$, however as Zweifel coefficient was increased above 0.8, loss coefficient of the exit region increased, the result of increased trailing edge losses. Turbine designs with Zweifel coefficients below 0.8 were also tested, it was shown that longer blade lengths could be employed, although these designs exhibited more friction losses and lower predicted efficiency in simulations.

4.3. Next Steps of the Project

Additional simulation work can be done to shed more light on the performance of CTPATs. The simulations done in this work demonstrate the efficacy of the designs; however the manufactured turbine will have real geometry different than the idealized 3-D modeled geometry simulated. The Woven Wheel turbomachinery manufacturing technique offers benefits, however additional work is required to mature the manufacturing process to the point where it could be used to produce turbine rotors within acceptable tolerances. At high Reynolds numbers the surface finish of the blades become more important to keep friction losses low [35].

Blade thickness was kept constant across each design within each set of specifications, referred to as a case. To achieve more complete dynamic similarity between each design in the Speed Study $\frac{t}{b}$ could be kept constant across each simulation, but for some of the higher speed simulations axial blade length must be decreased to keep Zweifel coefficient at .8, many of the blade thicknesses would be under 1 millimeter, which would be more costly to manufacture and could experience structural failure.

The designs tested in this analysis did not have inlet or outlet guide vanes. Further simulations would show how this affects the performance of the turbine at off-design points, at differing operating conditions. The simulations assumed a uniform laminar velocity profile at the turbine inlet. This is an idealized scenario, in a real world application flow would be more turbulent at the inlet and a nose cone/guide vanes would be required to guide the flow into the turbine similar to the one simulated in this study. Transient simulations would reveal additional details into the flow features. The speed and blade length studies could be repeated with different specifications, altering volume flow rate, head, and turbine geometry. This could reveal additional insights into how the inputs effect the specific speed at which peak efficiency is measured.

ANSYS CFX includes cavitation modeling as a part of the simulation package, designs of this type should be simulated with cavitation modeling to see where cavitation bubbles develop and collapse. The design could then be improved to reduce the risk of cavitation. Finite Element Analysis (FEA) simulations of the blades would validate the structural performance of the turbine designs. FEA can be used to find the points with the highest stresses, and the design can be changed to reduce stress in those areas.

Performance would be improved by using blade profiles designed for water turbines rather than using constant thickness blade profiles with rounded leading and trailing edges. Trailing edge thickness could be reduced to reduce flow deviation, reduce trailing edge losses and flow deviation.

REFERENCES

REFERENCES

[1] US. Department of Energy Wind and Water Power Technologies Office, "US. Department of Energy Wind and Water Power Technologies Office Funding in the United States: Hydropower Projects," 2012.

[2] S. e. a. Sangal, "Review of Optimal Selection of Turbines for Hydroelectric Projects," *International Journal of Emerging Technology and Advanced Engineering,* vol. 3, no. 3, p. 426, March 2013.

[3] P. Drtina and M. Sallaberger, "Hydraulic Turbines—Basic Principles and State-of-the-art Computational Fluid Dynamics Applications," in *Proceedings of the Institute of Mechanical Engineers*, 1999.

[4] S. L. Dixon and C. A. Hall, Fluid Mechanics and Thermodynamics of Turbomachinery, Elsevier, 2010.

[5] S. Adhau, "Economic Analysis and Application of Small Micro/Hydro Power Plants," in *International Conference on Renewable Energies and Power Quality*, April 2009.

[6] B. Hadjerioua, Y. Wei and S.-C. Kao, "An Assesment of Energy Potential at Non-Powered Dams in the United States," April 2012.

[7] B. Ogayar and P. G. Vidal, "Cost determination of the electro-mechanical equipment of a small hydro-power plant," *Renewable Energy*, vol. 34, pp. 6-13, 2009.

[8] N. Mueller.United States Patent US 7938627 B2, 2011.

[9] N. e. a. Mueller, "Low Cost Wound and Woven Turbomachinery Design," in *Proceedings of the ASME Turbo Expo 2007*, 2007.

[10] Dupont, "Kevlar Aramid Fiber Technical Guide," 2017. [Online]. Available: http://www.dupont.com/content/dam/dupont/products-and-services/fabrics-fibers-and-nonwovens/fibers/documents/Kevlar_Technical_Guide.pdf.

[11] J. H. Horlock, Axial Flow Turbines, Huntington, New York: Robert E. Krieger Publishing Company, 1966.

[12] S. A. Korpela, Principles of Turbomachinery, Hoboken, NJ: John Wiley and Sons, Inc., 2011.

[13] O. Cordier, ""Similarity Considerations in Turbomachines"," VDI Reports, 1955.

[14] T. Wright, Fluid Machinery: Performance, Analysis, and Design, CRC Press, 1999.

[15] O. E. Balje, Turbomachines: A Guide to Design, Selection and Theory, New York: John Wiley and Sons, 1981.

[16] Andritz Hydro, "Compact Hydro," September 2014. [Online]. Available: https://www.andritz.com/resource/blob/33446/089d4393ed0b9ee30e2f9ffba115430d/hy-compact-hydro-en-data.pdf.

[17] P. Adhikari, U. Budhathoki, S. R. Timilsina, S. Manandhar and T. R. Bajracharya, "A Study on Developing Pico Propeller Turbine for Low Head Micro Hydropower Plants in Nepal," *Journal of the Institute of Engineering, Nepal,* vol. 9, no. 1, pp. 36-53, 2013.

[18] S. F. Smith, "A Simple Correlation of Turbine Efficiency," *Journal of the Royal Aeronautics Society,* 1965.

[19] A. F. El-Sayed, Aircraft Propulsion and Gas Turbine Engines, Boca Raton, FL: CRC Press, 2008.

[20] J. D. Coull and H. P. Hodson, "Blade Loading and its Application In The Mean Line Design of Low Pressure Turbines," in *Proceedings of the ASME Turbo Expo 2011*, Vancouver, 2011.

[21] S. C. Kacker and U. Okapuu, "A Mean Line Prediction Method for Axial Flow turbine Efficiency," *Journal of Engineering Power,* vol. 104, pp. 111-119, 1982.

[22] M. T. Schobeiri, Turbomachinery Flow Physics and Dynamic Performance, New York: Springer, 2005.

[23] O. Zweifel and B. &. C. Brown, "The Spacing of Turbomachine Blading, Especially with Large Angular Deflection," 1945.

[24] E. Dick, Fundamentals of Turbomachines, Springer, 2015.

[25] C. Prakash, D. G. Cherry, H. W. Shin, J. Machnaim, L. Dailey, R. Beacock, D. Halstead and A. R. Wadia, "Effect of Loading Level and Distribution on LPT Losses," in *Proceedings of ASME Turbo Expo 2008*, Berlin, Germany, 2008.

[26] S. C. M. R. M. a. T. C. C. J. P. C. P. J. K. a. S. L. P. J. T. Schmitz, "Highly Loaded Low-Pressure Turbine: Design, Numberical, and Experimental Analysis," in *Proceedings of the ASME 2010 Turbo Expo*, Glasgow, Scotland, 2010.

[27] H. Pfeil, Optimale Primarverluste in Axialgittern und Axialstufen von Stromungsmaschinen, VD-Forschungsheft, p. 535.

[28] J. T. Schmitz, S. C. Morris, R. Ma, T. C. Corke, J. P. Clark, P. J. Koch and S. L. Puterbaugh, "Highly Loaded Low-Pressure Turbine: Design, Numerical, and Experimental Analysis," in *Proceedings of the ASME Turbo Expo 2010*, 2010.

[29] T. J. Praisner , E. A. Grover and D. C. Knezevici, "Toward the Expansion of Low-Pressure Turbine Airfoil Design Space," in *Proceeedings of the ASME Turbo Expo 2008*, Germany, 2008.

[30] M. Ćosić, M. Dojčinovi and Z. Aćimović-Pavlovic, "Fabrication and Behaviour of Al-Si/SiC Composite in Cavitation Conditions," *International Journal of Cast Metals Research,* vol. 27, 2014.

[31] T. Yamatogi, H. Murayama, K. Uzawa, K. Kageyama and N. Watanabe, "Study on Cavitation Erosion of Composite Materials for Marine Propeller," in *ICCM International Conferences on Composite Materials*, 2009.

[32] D. D. J, "Loss Mechanisms in Turbomachines," in *International Gas Turbine and Aeroengine Congress and Exposition*, Cincinatti, Ohio, 1993.

[33] W. Fox, W. Pritchard and A. McDonald, Introduction to Fluid Mechanics, Seventh Edition ed., John Wiley and Sons, 2010.

[34] Hydraulic Institute, Pipe Friction Manual, New York, 1954.

[35] C. Canuto, M. Y. Hussani, A. Quarteroni and T. A. Zang, Spectral Methods: Evolution to Complex Geometries and Applications to Fluid Dynamics, Springer, 2007.

[36] Voith Hydro, "Environmentally Friendly Turbine Design," May 2011. [Online]. Available: http://www.voith.com/corp-de/VH_Product_Brochure_Environmentally-friendly-turbine-design_14_vvk_t3360e_en.pdf.

[37] J. M. Becker, "Identifying the Effects on Fish of Changes in Water Pressure during Turbine Passage," *Hydro Review,* vol. 22, no. 5, pp. 1-4, September 2003.

[38] G. Cada, "The Development of Advanced Hydroelectric Turbines to Improve Fish Passage Survival," *Fisheries,* p. 14, September 201.

[39] S. Lieblein, F. C. Schwenk and R. L. Broderick, "Diffusion Factor for Estimating Losses and Limiting Blade Loadings in Axial Flow Compessor Blade Elements," National Advisory Committee for Aeronautics, Washington, 1953.

[40] R. W. Johnson, The Handbook of Fluid Dynamics, Boca Raton, FL: CRC Press, 2000.

[41] W. W. Peng, Fundamentals of Turbomachinery, Hoboken, NJ: John Wiley and Sons, 2007.

[42] D. R. Durgaiah, Fluid Mechanics and Machinery, New Dehli: New Age International Ltd., 2002.